Titre: Title:	Circular grating DFB and DBR lasers : theory and experiment
Auteur: Author:	Chunmeng Wu
Date:	1992
Type:	Mémoire ou thèse / Dissertation or Thesis
Référence: Citation:	Wu, C. (1992). Circular grating DFB and DBR lasers : theory and experiment [Thèse de doctorat, Polytechnique Montréal]. PolyPublie. https://publications.polymtl.ca/57975/

UNIVERSITÉ DE MONTRÉAL

CIRCULAR GRATING DFB AND DBR LASERS: THEORY AND EXPERIMENT

par

CHUNMENG WU

DÉPARTEMENT DE GÉNIE PHYSIQUE

ÉCOLE POLYTECHNIQUE

THÉSE PRÉSENTÉE EN VUE DE L'OBTENTION

DU GRADE DE PHILOSOPHIAE DOCTOR (Ph.D.)

(GÉNIE PHYSIQUE)

juin 1992

ISBN 0-315-77690-0

UNIVERSITÉ DE MONTRÉAL

ECOLE POLYTECHNIQUE

Cette thèse intitulée :

CIRCULAR GRATING DFB AND DBR LASERS: THEORY AND EXPERIMENT

présentée par : Chunmeng Wu

en vue de l'obtention du grade de Philosophiae Doctor (Ph.D.)

a été dûment acceptée par le jury d'examen constitué de :

M. Bures, Jacques, D.Sc., président

M. Bertrand, Lionel, D. d'État, membre

M. Chrostowski, Jacek, Ph.D., membre

M. Najafi, S.Iraj, Ph.D., membre et directeur de recherche

M. Maciejko, Romain, Ph.D., membre et directeur de recherche

To

Jane Qu

SOMMAIRE

Dans cette thèse, deux nouvelles structures de laser à semi-conducteurs sont proposées et étudiées: le laser à rétroaction distribuée par réseau circulaire (circular-grating distributed-feedback (CG-DFB) laser) et le laser à réflexion distribuée de Bragg par réseau circulaire (circular-grating distributed-Bragg-reflector (CG-DBR) laser).

Une nouvelle théorie du couplage d'ondes est formulée spécialement dans le cas des ondes cylindriques. Cette théorie est une formulation vectorielle basée sur les équations de Maxwell pour les champs électro-magnétiques. La théorie est appliquée à une analyse des caractéristiques des modes des lasers CG-DFB et CG-DBR. Pour la premiere fois, une analyse du courant de seuil est présentée pour des lasers CG-DFB et CG-DBR à l'hétérostructure GaInAsP/InP.

Le premier laser CG-DFB à émission de surface est fabriqué en GaInAsP/InP. L'action laser est démontrée par pompage optique. Le longueur d'onde d'émission est 1.283μm. Une puissance maximum de 25mW a été mesurée.

Le premier laser CG-DBR utilisant l'injection de courant est aussi réalisé. Le courant de seuil est de 140mA et la puissance émise de la surface est supérieure à 10mW.

ABSTRACT

In this thesis, two novel laser structures are proposed: the circular-grating distributed-feedback (CG-DFB) laser and the circular-grating distributed-Bragg-reflector (CG-DBR) laser. They are studied both theoretically and experimentally.

A new coupled-wave theory for cylindrical waves is formulated as the basis for the theoretical analysis of CG-DFB and CG-DBR lasers. The coupled-wave theory established here is a self-consistent, vector-wave formulation based on Maxwell's equations for the electromagnetic fields. A large radius approximation to the new coupled-wave equations is also derived. Discrepancies between the new, vector-wave formulation presented in this thesis and the scalar-wave derivations by other researchers are clarified.

The threshold gain and the mode properties of CG-DFB and CG-DBR lasers are studied by this new coupled-wave theory. An analytical eigenvalue equation is obtained for the threshold condition. For the first time, a threshold current analysis is made for these novel laser structures. It is found that for both types of lasers, by a proper choice of the inner radius (i.e, the phase-shift), one can select the laser oscillation to be either in the even cylindrical-wave modes or in the odd cylindrical-wave modes. This possibility of mode selection is important in the design of CG-DFB and CG-DBR lasers. It is also found that CG-DFB lasers have a higher threshold gain and a higher threshold current than CG-DBR lasers.

The concept of CG-DFB and CG-DBR lasers is verified experimentally. The first optically-pumped surface-emitting CG-DFB laser is fabricated using the GaAsInP/InP heterostructure. Lasing action is demonstrated at 1.283 μm. The maximum surface-emitted optical power is measured as high as 25 mW.

The first electrically-pumped surface-emitting CG-DBR laser is also successfully demonstrated on the GaInAsP/InP material. The lowest threshold current is 140mA and the maximum measured surface-emitted optical power exceeds 10mW.

RÉSUMÉ

Le concept des lasers à rétroaction distribuée (Distributed FeedBack (DFB) laser) fut introduit par Kogelnik et Shank au début des années 1970 [1-2]. Depuis leurs travaux originaux, les lasers DFB ont attiré beaucoup d'attention [3-55].

Les lasers à semi-conducteurs qui utilisent la rétroaction distribuée peuvent être classifiés en deux catégories: les lasers DFB et les lasers DBR (Distributed-Bragg-Reflector). Dans les lasers DFB, la rétroaction nécessaire pour maintenir l'oscillation du laser n'est pas localisée aux facettes de la cavité, mais est plutôt distribuée sur toute la longueur de celle-ci. Cet effet est obtenu grâce à un réseau gravé dans une couche épitaxiale qui fait partie de l'hétérostructure. La variation périodique de l'épaisseur de la couche gravée crée une perturbation périodique de l'indice de réfraction. La rétrodiffusion de Bragg produite par le réseau couple les champs se propageant vers l'avant et vers l'arrière. La condition de Bragg détermine la selectivité en fréquence du laser DFB. Pour les lasers DBR, les réseaux sont fabriqués aux deux bouts de la cavité et il n'y a pas de rétroaction dans la région active située au centre. Les deux régions ondulées fonctionnent effectivement comme des miroirs dont la réflectivité est une fonction de la longueur d'onde.

En comparaison avec les lasers à semi-conducteurs conventionnels de type Fabry-Pérot (FP), les lasers DFB et DBR ont une longueur d'onde démission plus stable et une largeur de raie réduite. Ces deux aspects sont importants pour les systèmes de communication par fibre optique. Afin de bien utiliser les fenêtres d'atténuation minimale de la fibre de silice, à environ 1.3μm et 1.55μm, et de réaliser des systèmes à fibre optique à

large bande et à haut débit, on a développé les lasers DSM (dynamic single-mode) utilisant le mécanisme de rétroaction distribuée [56].

En plus d'une sélectivité en fréquence accrue, on peut aussi obtenir une émission de surface grâce à un réseau du deuxième ordre. Ceci fournit en même temps la rétroaction au laser par la réflexion de Bragg du deuxième ordre et le couplage au champ radiatif par interaction du premier ordre [57]. Des lasers DFB et DBR à émission de surface par injection ont déjà été réalisés [58-60]. L'émission de surface est une propriété souhaitable pour l'intégration monolithique. À cause de la géométrie rectiligne des réseaux du second ordre utilisés dans les travaux antérieurs, l'émission de surface prend la forme d'un faisceau rectangulaire dont les angles de divergence sont différents selon les directions parallèle et perpendiculaire aux lignes du réseau.

Ce problème peut être corrigé en utilisant un réseau circulaire du deuxième ordre pour obtenir une émission normale à la surface. La structure d'un laser DFB et celle d'un laser DBR à réseau circulaire (circular-grating DFB (CG-DFB) laser ou circular-grating DBR (CG-DBR) laser) sont les versions à deux dimensions des structures de rétroaction distribuée considérées par Kogelnik et Shank [1-2]. Les lasers CG-DFB furent proposés par Shimpe [61] en 1988. Deux ans après cette proposition, en 1990, Toda [62] a fait une analyse du caractère monomode d'un laser CG-DFB non-périodique. Dans la même année, Erdogan et Hall [63] présentaient leur analyse du gain de seuil d'un laser CG-DFB dans le cadre d'une théorie scalaire du couplage modal. En 1991, Gong et al [64] ont fait une analyse d'onde scalaire des lasers CG-DBR. On a aussi étudié des résonateurs passives aux réseaux circulaires [65-66].

Dans les lasers à réseau circulaire, le mécanisme de rétroaction est essentiellement le même que dans le cas des lasers DFB rectilignes. La différence majeure est que maintenant on traite des ondes cylindriques qui se propagent radialement vers le centre et vers

l'extérieur, au lieu d'ondes planes qui vont vers l'avant et vers l'arrière. A cause de leur symétrie circulaire, les lasers CG-DFB et CG-DBR offrent des avantages pour les applications pratiques. Par exemple, il est possible d'obtenir un faisceau circulaire dont la divergence est très petite parce que la surface d'émission est circulaire et plus large que dans le cas des lasers à émission latérale. Il est aussi possible de réaliser un faisceau focalisé avec un réseau circulaire façonné comme une lentille de Fresnel. Un autre avantage est la formation d'émetteurs-réseau. De plus, les tests sont plus faciles à réaliser parce qu'il n'y a pas de facettes clivées.

Le but de cette thèse est d'étudier théoriquement et expérimentalement les caractéristiques des lasers CG-DFB et CG-DBR. Nous avons établi une formulation vectorielle de la théorie du couplage entre les ondes. La théorie est spécialement développée pour analyser des dispositifs utilisant des réseaux circulaires. Nous avons aussi analysé les caractéristiques des modes et calculé le courant de seuil des lasers CG-DFB et CG-DBR. Récemment, nous avons réussi à fabriquer et caractériser le premier laser CG-DFB pompé optiquement et le premier laser CG-DBR utilisant l'injection de courant. Parce que le matériau GaInAsP produit des sources les plus courantes pour les systèmes à fibre optique, tous les exemples théoriques et expérimentaux sont basés sur cet alliage. Cependant, la théorie développée dans cette thèse est applicable à d'autres matériaux comme l'AlGaAs et l'InGaAs.

La thèse est composée de cinq chapitres. Les deux premiers décrivent la théorie du couplage entre ondes cylindriques. Le troisième analyse les modes et le courant de seuil des lasers CG-DFB et CG-DBR. Les deux derniers chapitres présentent des résultats expérimentaux. Le contenu de chaque chapitre est décrit brièvement ci-dessous.

Les ondes se propageant dans des dispositifs à réseau circulaire sont les ondes cylindriques qui sont représentées par les fonctions de Hankel [61-66]. La théorie

conventionnelle du couplage entre modes pour les structures à une dimension n'étant pas applicable, il est désirable d'établir des équations de couplage entre les ondes spécialement pour les ondes cylindriques. Ceci est présenté au chapitre 1. La formulation est basée sur les équations de Maxwell. C'est une formulation générale, consistante et vectorielle de la théorie du couplage entre les ondes pour les ondes cylindriques dans un guide plan à réseau circulaire. Nous commençons par définir les ondes cylindriques de polarisation TE et TM. Après avoir prouvé la relation d'orthonormalité entre les ondes cylindriques, les équations de couplage entre les ondes sont dérivées selon la ligne de pensée de Kogelnik [67]. Dans la théorie conventionelle du couplage entre modes, les modes TE ne sont pas couplés avec les modes TM, mais dans la nôtre il existe un couplage entre les ondes cylindriques de polarisation TE et celles de polarisation TM. La théorie développée ici est plus générale que celle de Zheng et Lacroix [65-66] dans laquelle seulement les ondes cylindriques de premier ordre furent considérées. Notre théorie est également différente de la formulation scalaire de Erdogan et Hall [63]. La théorie dérivée dans le chapitre 1 forme la base théorique des lasers CG-DFB et CG-DBR étudiés dans les chapitres suivants.

Dans le chapitre 2, les équations de couplage entre les ondes cylindriques sont simplifiées. Nous démontrons que le couplage entre les ondes cylindriques TE et TM est négligeable quand le rayon r est suffisamment grand ($r >> 1/\beta$), ce qui est vérifié en pratique. Cette approximation rend séparables en deux groupes les équations de couplage entre les ondes: un groupe pour les ondes cylindriques TE et l'autre pour les ondes cylindriques TM. Dans ce chapitre, nous allons aussi discuter des différences entre notre théorie et celle d'Erdogan et Hall [63].

Grâce à la théorie développée dans les chapitres 1 et 2, une analyse détaillée du seuil d'oscillation est faite au chapitre 3 pour des lasers à semi-conducteurs CG-DFB et CG-DBR. Les équations de couplage entre les ondes sont résolues et une équation aux valeurs

propres est obtenue analytiquement pour le gain de seuil des lasers CG-DFB et CG-DBR; des résultats numériques sont présentés. Par ajustement de la phase Ω, c'est-à-dire le rayon de la région centrale, on peut forcer l'oscillation laser sur des ondes cylindriques d'ordre soit pair ou impair. Ce résultat est important pour les réalisation pratiques des lasers CG-DFB et CG-DBR. Nous avons aussi fait une estimation du courant de seuil. On a trouvé que la densité de courant de seuil et le courant de seuil pour les lasers CG-DFB sont plus élevés que pour les lasers CG-DBR.

Le chapitre 4 se concentre sur les caractéristiques du premier laser CG-DFB à émission de surface, basé sur une hétérostructure GaInAsP/InP. Le réseau circulaire est fabriqué par lithographie de faisceau d'électrons (E-beam) et la technique de gravure par ion réactif (RIE: reactive-ion-etching). La structure de notre laser CG-DFB est d'abord décrite, suivie par une explication de la procédure de fabrication. Les résultats expérimentaux du premier laser CG-DFB à émission de surface par pompage optique sont présentés.

Au chapitre 5, on discute du premier laser CG-DBR utilisant l'injection de courant, fabriqué en GaInAsP/InP. Nous avons modifié l'équation aux valeurs propres afin de tenir compte de la perte d'énergie à l'interface entre la région de gain et la région du réseau. Les caractéristiques optiques du premier laser CG-DBR à émission de surface sont présentées.

Le succès de la démonstration des lasers CG-DFB et CG-DBR est une contribution importante de cette thèse. Le concept proposé par Shimpe [61] est maintenant devenu une réalité. Cependant, il y a encore beaucoup de travail à faire pour améliorer l'efficacité des lasers CG-DFB et CG-DBR. Par exemple, à cause de l'imperfection du couplage entre la région centrale de gain et celle de réseau, le courant de seuil expérimental de nos lasers CG-DBR est plus élevé que celui prédit notre théorie et l'opération à courant continu (CW: continuous wave operation) n'a pas été obtenue. Aussi, nos lasers oscillent dans les ondes cylindriques impaires et non pas les ondes paires. L'optimisation des lasers à réseau

circulaire est nécessaire pour réduire le courant de seuil, la densité de courant de seuil, et pour augmenter la puissance émise de la surface. Il faudra étudier l'efficacité et la distribution spatiale du rayonnement, ainsi que les caractéristiques dynamiques et spectrales. Jusqu'à présent, le réseau circulaire a été écrit par lithographie E-beam et FIB (Focussed-Ion -Beam). Les deux techniques sont très onéreuses, et en plus, elles demandent beaucoup de temps. Il est désirable d'avoir un autre moyen, comme une méthode holographique, pour fabriquer des réseaux circulaires.

Même si l'utilisation courante des lasers CG-DFB et CG-DBR est encore lointaine, nous croyons que par une étude théorique et des travaux expérimentaux, il est possible de les optimiser. On peut réduire le courant de seuil et augmenter la puissance émise de la surface. Ce sont des sources prometteuses pour les systèmes de communication par fibre optique, l'interconnexion optique et les applications en espace libre.

ACKNOWLEDGEMENT

I would like to thank Professor Romain Maciejko and Professor S. Iraj Najafi, for their patience in guiding me throughout my Ph.D researches. Their experience in both the experimental and the theoretical sides have been very valuable to me.

I am grateful to Professors Jacques Bures and Lionel Bertrand of Ecole Polytechnique, Dr. Jacek Chrostowski of National Research Council (NRC), Professor Weiping Huang of the University of Waterloo, and Dr. Toshihiko Makino of Bell-Northern-Research (BNR), for participating in my thesis committee and for giving advices and suggestions to improve the manuscript.

I gratefully acknowledge the management of BNR for its support on the project. Especially, I would like to thank the Advanced Technology Laboratory of BNR for providing the technical help that is very important for the success of this work.

I would like to thank Dr. George Chik for being very supportive since the beginning of the project.

I would like to express my deep thanks to Dr. Jan Glinski. It was due to his willingness to accept me as a co-op student to work in the Department of Exploratory Devices of Advanced Technology Laboratory (BNR), that gave me the chance to study circular grating lasers.

Thanks are due to Dr. Toshihiko Makino. His knowledge on semiconductor lasers has been of great help to me. We had many long discussions and brain-storming sessions on the theoretical aspects and the designs of circular grating lasers.

I am grateful to Dr. Mikelis Svilans for his skill in mask design and optical measurement. I am also grateful for his interests in the project. There have been many useful discussions during our coffee tasting sessions.

I would like to thank Dr. Mahmoud Fallahi and Dr. Ian Templeton of NRC for their help in patterning circular gratings. Their collaboration are indispensable for the success of the first optically-pumped circular grating DFB laser and the first electrically-pumped circular grating DBR laser.

I am grateful to Gordon. Knight, Cornelis Blaauw and Norbert Puetz. Their expertise in crystal growth, especially the selective regrowth done by Gordon, formed a solid basis for the success of this project.

I would like to thank Cheryl Maritan and Mavis Hillier. Though they often have a heavy workload, they always manage to find time to process the wafers.

I would like to acknowledge the help of Karen Fox, Chuchay Tan and Joanne Zorzi in doing the scanning-electron-scope (SEM) analysis of the devices.

Thanks are due to Zehra Husain for her skillful hands in cleaving the devices, to Laura Raine for her help in wire-bonding and to Edith Carroll as well.

I would also like to thank Dr. Jacques Albert of Communications Research Center (CRC), Dr. Sylvain Charbonneau of NRC, Carla Miner and Brad Watt of BNR, for their help in the optical pumping measurement. I would also like to say thanks to Michel Gallant for his useful comments when I had difficulties in doing the optical pumping experiment.

Thanks are due to Claude Rolland, Larry Tarof, Gouping Li, Bernard Villeneuve, Douglas Beckett and Grzegoz Pakulski of the Department of Exploratory Devices, for their encouragement and team-support. Bernard deserves a special thanks for his help in preparing the résumé in French.

And I also like to thank Jingwen Jiang, Gouping Li and Mikelis Svilans, for their carefull reading of and their valuable comments on the manuscript.

Finally, I would like to thank Jane Qu for her love and her support.

TABLE OF CONTENTS

LIST OF TABLES

PAGE

LIST OF FIGURES

LIST OF APPENDICES

INTRODUCTION

The concept of the distributed feedback (DFB) laser was first introduced and demonstrated by Kogelnik and Shank in the early 1970's [1-2]. Since their pioneering work, DFB semiconductor lasers have attracted considerable attention both experimentally and theoretically [3-55].

From the viewpoint of device operation, semiconductor lasers employing distributed feedback can be classified into two broad categories: the DFB lasers and the distributed Bragg reflector (DBR) lasers. They are shown schematically in Fig.1.

In DFB lasers, the feedback necessary for the lasing action is not localized at the cavity facets but is distributed throughout the cavity length. This is achieved by etching a grating along the cavity length into one of the epitaxial layers that forms part of the heterostructure. The periodic variation in the thickness of the etched layer creates a periodic perturbation of the effective index of refraction. The backward Bragg scattering generated by the grating provides the feedback by coupling the forward- and backward propagating waves. Mode selectivity of the DFB mechanism results from the Bragg condition.

In DBR lasers, the grating is etched near the cavity ends and distributed feedback does not take place in the central active region. The unpumped corrugated end regions act as effective mirrors whose reflectivity is wavelength-dependent.

(a) DFB laser (b) DBR laser

Fig.1 Schematic view of conventional DFB and DBR lasers

In comparison with the conventional Fabry-Perot-type (FP) semiconductor lasers, DFB and DBR lasers provide an improved wavelength stability and a reduced linewidth. Both are important for today's optical fiber systems. In order to take advantage of the low-loss window occurring around the wavelengths of 1.3μm and 1.55 μm in silica fibers, and to realize wide-band high speed optical fiber transmission systems, the distributed feedback mechanism has been employed to develop dynamic-single-mode (DSM) lasers [56].

In addition to the advantage of frequency selectivity, surface emission which is desirable for monolithic integration purposes can also be obtained by using a second-order grating [57]. In this case, feedback is produced by the second-order Bragg reflection process and radiation is achieved through the first-order interaction. Electrically pumped surface-emitting DFB and DBR lasers have been reported [58-60]. For conventional surface-emitting DFB and DBR lasers, the surface-emitted beam has unequal divergence angles along directions parallel and perpendicular to the grating lines, due to the longitudinal shape of the emission surface. This results in high coupling losses when the surface-emitted power must be coupled to an optical fiber.

The above problem however can be overcome by using a second-order circular grating to couple light out normal to the surface. Fig.2 illustrates the structures of CG-DFB and CG-DBR lasers. In CG-DFB lasers, the feedback mechanism is essentially the same as in conventional DFB lasers. The main difference is that we are dealing with cylindrical waves going into and out from the center, rather than plane waves travelling forward and backward.

CG-DFB lasers were first proposed by Shimpe [61] in 1988. Toda was the first one to analyze the single-mode behavior of a disk-shaped DFB laser with a non-periodic circular grating [62]. In the same year, Erdogan and Hall [63] gave a scalar-wave coupled-mode analysis on the threshold gain of circular grating DFB lasers. In 1991, Gong et al [64], presented their scalar-wave analysis of CG-DBR lasers. There were also analyses of passive circular grating resonators [65-66].

Owing to their circular symmetry, CG-DFB and CG-DBR lasers are of fundamental interest. These novel laser structures offer several potential advantages for practical applications. For example, they give a low-divergence circular beam because of their circular emission surface and a much larger aperture compare to conventional edge-emitting stripe lasers. They offer the possibility of a focussed beam. This can be realized by designing the circular grating like a Fresnel lens. Another advantage is the possibility of

making integrated arrays. Furthermore, because no cleaved facets are needed, on-wafer testing is easy to perform.

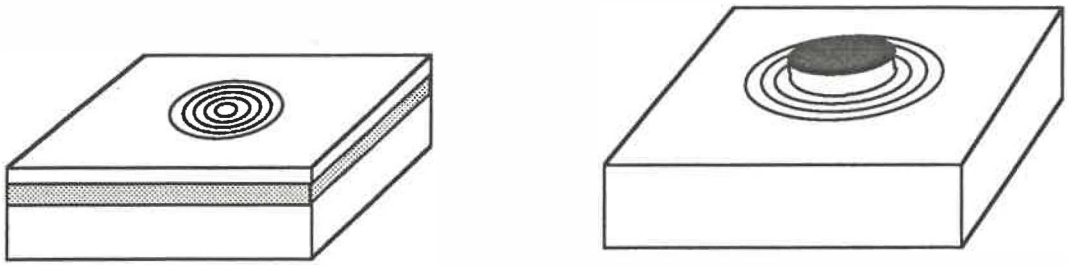

(a) CG-DFB laser (b) CG-DBR laser

Fig. 2 Schematic view of CG-DFB laser and CG-DBR lasers

The purpose of this thesis is to study, both theoretically and experimentally, CG-DFB and CG-DBR lasers. As GaInAsP lasers are the most widely used light sources for optical fiber communication systems, our theoretical examples and experiments are concentrated on this material. It should be stressed, however, that the theoretical aspects of CG-DFB and CG-DBR lasers discussed in this thesis apply to other materials, such as AlGaAs, InGaAs as well.

This thesis contains five chapters. The first three chapters present the theoretical background and the last two report the experimental results. A brief outline of each chapter is now given:

Because the propagating waves in circular grating devices are outward and inward cylindrical waves represented by Hankel functions [61-66], the coupled-mode theories for one dimensional periodic structures are no longer applicable here. It is therefore desirable to establish a special set of coupled-wave equations for cylindrical waves in circular periodic structures. Chapter 1 gives a general, self-consistent, vector-wave formulation of the coupled-wave theory for cylindrical waves in circular grating planar waveguides. Starting from Maxwell's equations, the definition of TE- and TM-cylindrical waves is introduced and the orthonormality relation between cylindrical waves is proved. The coupled-wave equations are then derived along Kogelnik's line of thought [67]. Unlike the conventional

coupled-mode theory in which the TE modes do not couple with the TM modes, our coupled-wave equations consist of a system of four first-order differential equations which include the inter-polarization coupling between TE- and TM-cylindrical waves. A discussion of the coupling between different cylindrical waves follows. The coupled-wave theory developed in this chapter is more general than the one given by Zheng and Lacroix [65-66] where only zeroth order cylindrical waves were considered, and is different from the scalar formulation of Erdogan and Hall [63] which is for TE-cylindrical waves. This new coupled-wave theory forms the theoretical basis for the analysis of CG-DFB and CG-DBR lasers in later chapters.

In Chapter 2, a simplified form of the coupled-wave equations is derived for cylindrical waves in circular grating planar waveguides. It is shown that under the large radius approximation ($\beta r >> 1$), the coupling between TE and TM cylindrical waves can be neglected. This renders the coupled-wave equations separable into two sets, one for TE cylindrical waves and the other for TM cylindrical waves. The large radius approximation is valid for most practical cases. The difference between the theory in this thesis and the scalar theory of Erdogan and Hall [63] is clarified.

In Chapter 3, a detailed threshold analysis for TE-cylindrical waves in CG-DFB and CG-DBR lasers is given. The analysis is based on the coupled-wave theory developed in Chapters 1 and 2. The coupled equation is solved analytically to obtain an eigenvalue equation for the threshold gain of the lasing modes. Numerical results on the threshold gain and the mode properties are presented. It is shown that, by a proper choice of the total phase-shift Ω (in other words, the inner radius R_1), the laser can be tuned to oscillate in either the even or the odd cylindrical waves. This is an important result for practical designs. By using a linear model, an estimate of the threshold current density and the threshold current of circular grating lasers is also given. CG-DFB lasers are found to have a higher threshold current density and a higher threshold current than CG-DBR lasers.

Chapter 4 concentrates on the lasing characteristics of the first surface-emitting CG-DFB laser fabricated on a GaInAsP/InP double heterostructure by electron-beam (E-beam) lithography and reative-ion-etching (RIE). The structure of the CG-DFB laser is first described. An explanation of the fabrication procedures follows. The experimental results of the first optically-pumped surface-emitting CG-DFB laser are given in the last section. The experiments are carried out at room temperature.

Chapter 5 discusses the design and fabrication of the first electrically-pumped CG-DBR lasers on a GaInAsP/InP heterostructure . First, the threshold eigenvalue equation is

modified to take into account the coupling loss at the interface between the gain region and the grating. Design curves in terms of the coupling coefficient and the power coupling efficiency between the gain region and the grating region are given. Fabrication procedures for CG-DBR lasers are then described. The optical characteristics of the first electrically pumped surface-emitting CG-DBR lasers are presented.

CHAPTER 1

SELF-CONSISTENT COUPLED-WAVE THEORY FOR CYLINDRICAL WAVES

1.1. Introduction

Circular grating devices have received much attention in the past years [61-66, 68-70]. Tien [68] initially suggested curved-line gratings as reflectors and resonators. Shimpe [61] proposed cylindrical diffraction grating couplers and distributed feedback resonators. Toda [62] made an analysis of the single-mode behavior of a disk-shaped DFB laser. Erdogan and Hall were the first to analyze the threshold gain of circular symmetric distributed feedback semiconductor lasers [63]. Gong et al [64], presented their scalar-wave analysis of CG-DBR lasers. Zheng, et al showed the applicability of circular gratings as resonators [65] and analyzed the mode-coupling in passive circular grating devices [66] . Hori, et al.[69], and Shiono, et.al.[70], respectively designed and fabricated focusing grating mirror by electron beam lithography. Circular gratings could be used in leaky-wave antenna [71], which, when combined with active materials, would be a new type of surface-emitting lasers. Circular gratings could also serve as a multi-port directional coupler [66, 72], which would be especially useful in multi-channel operation. In addition to circular gratings, elliptic Bragg reflectors have also been proposed by Sudbø [73] for applications in integrated optics.

Though both use gratings to obtain distributed feedback, there is a main difference between circular grating devices and the conventional grating devices. In the former, the propagating waves are the cylindrical waves going into or out from the center. The field distribution spreads over the entire guide-plane, thus is two-dimensional in nature. Mathematically, cylindrical waves are described by Hankel functions. In the latter, the propagation of modes is along the axial direction and is described by the exponential

functions ($\exp(\pm j\beta z)$ for z-direction propagation). Because of this fundamental difference, the coupled-mode theory for conventional waveguides [67, 74-79] is not applicable to circular grating optical devices such as circular-grating distributed-feedback (CG-DFB) lasers and circular-grating distributed-Bragg-reflector (CG-DBR) lasers.

There have been several attempts to derive coupled-wave equations for cylindrical waves [63-66]. The coupled-wave theory of Erdogan and Hall [63] was a scalar-wave formulation in which only TE- cylindrical waves in a single-mode slab waveguide were considered. The same can be said about the formulation of Gong, et al [64]. Zheng's coupled-wave theory for circular grating resonators [65-66] is valid only for zeroth-order cylindrical waves.

In order to have a better understanding of the characteristics of circular grating devices and to give a simple but powerful tool for their analysis, a complete vector-wave coupled-wave theory that is applicable to higher order cylindrical waves and takes into account of both TE and TM cylindrical waves is needed. The purpose of this chapter is to give a full-detailled, vector-wave formulation of the coupled-wave theory for cylindrical waves. This new theory can be applied to analyze both passive and active grating devices formed on planar dielectric waveguides.

This chapter is organized as follows: in section 1.2, starting from Maxwell's equations, TE and TM cylindrical waves in an ideal planar waveguide are first defined. Then, the orthonormality relations between cylindrical waves are proved. The coupled-wave theory for cylindrical waves is established in section 1.3. A general discussion on coupling between different cylindrical waves is presented in section 1.4. A summary of the theory is given in section 1.5. Details of the derivations are given in Appendices I-III. Comparison between the vector-wave formulation of this Chapter and the scalar coupled-wave theory of Erdogan and Hall [63] is left to Chapter 2 where the coupled-wave equations are simplified.

1.2 Cylindrical Waves in A Planar Dielectric Waveguide

1.2.1 Definition of Cylindrical Waves

Consider a planar dielectric waveguide. The structure and the coordinates are indicated in Fig.3. The relative permittivity of the waveguide is denoted by ε, with $\varepsilon = \varepsilon_c$ for the cover layer , $\varepsilon = \varepsilon_f$ for the guiding layer and $\varepsilon = \varepsilon_s$ for the substrate layer. In our analysis,

cylindrical coordinates are used, with the r-and θ-directions in and the z-direction normal to the plane of the waveguide.

In each uniform layer, the z-components of the electric field and the magnetic field satisfy the wave equation [74]

$$\left(\nabla^2+\omega^2\varepsilon_0\mu_0\varepsilon\right)\begin{Bmatrix} E_z \\ H_z \end{Bmatrix} = 0 \tag{1.1}$$

where ω is the frequency of the light wave in the waveguide, μ_0 is the permeability and ε_0 the permittivity of free space, respectively. ε denotes the relative permittivity. We have implicitly assumed a time dependence in the form of exp(jωt).

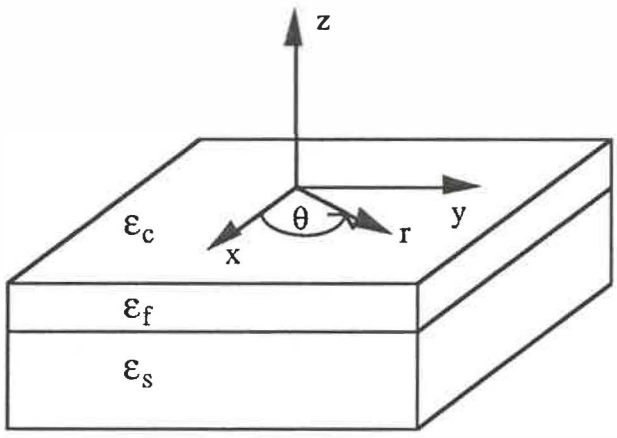

Fig.3 Ideal planar dielectric waveguide without perturbation: $\Delta\varepsilon(r,\theta,z)=0$.

The Laplacian operator ∇^2 in cylindrical coordinates is given by

$$\nabla^2 = \frac{1}{r}\frac{\partial}{\partial r}\left(r\frac{\partial}{\partial r}\right)+\frac{1}{r^2}\frac{\partial^2}{\partial\theta^2}+\frac{\partial^2}{\partial z^2} \tag{1.2}$$

In order to solve Eq.(1.1), we use the method of separation of variables. That is, assuming solutions of the form [80]

$$\psi(r,\theta,z) = \{E_z \text{ or } H_z\} = R(r)\, Z(z)\, \Phi(\theta) \tag{1.3}$$

where R(r), $\Phi(\theta)$ and Z(z) describe the field distribution in the r-, the θ- and the z-directions, respectively.

Substituting Eq.(1.3) into Eq.(1.1) and performing separation of variables, we obtain

$$\frac{d^2Z}{dz^2} + [\omega^2 \mu_0 \varepsilon_0 \varepsilon - \beta^2] Z = 0 \tag{1.4a}$$

$$\frac{d^2\Phi}{d\theta^2} + n^2 \Phi = 0 \tag{1.4b}$$

$$r\frac{d}{dr}(r\frac{dR}{dr}) + [(\beta r)^2 - n^2] R = 0 \tag{1.4c}$$

where n and β are constants of separation.

Comparing Eq.(1.4a) with the one dimensional scalar wave equations for TE and/or TM modes [67], we see that Eq.(1.4a) defines the slab modes of a planar dielectric waveguide and β is the propagation constant of the corresponding slab mode. The solutions for Eq.(1.4a) as well as the dispersion equations for calculating β can be found in standard textbooks, such as [67, 74-76].

Since the permittivity of each layer is uniform, periodic condition must be satisfied such that $\Phi(\theta+2\pi)=\Phi(\theta)$. Thus, the constant n in Eq.(1.4b) has to be an integer, and the solution of Eq.(1.4b) can be written as

$$\Phi(\theta) = e^{jn\theta} \tag{1.5}$$

with n=0, ±1, ±2, ±3,...etc. We call n the order of the cylindrical wave.

Eq.(1.4c) is Bessel's equation of integer order n [81-82], which describes the radial propagation of cylindrical waves. As we are considering the propagation of outward or inward waves, the solutions of Eq.(1.4c) are chosen to be Hankel functions [80], i.e

$$R(\beta r) = H_n^{(2)}(\beta r) = J_n(\beta r) - j\, N_n(\beta r) \tag{1.6a}$$

for outward-propagating wave, and

$$R(\beta r) = H_n^{(1)}(\beta r) = J_n(\beta r) + j\, N_n(\beta r) \tag{1.6b}$$

for inward-propagating wave. These two solutions are independent of each other.

In Eqs.(1.6), $H_n^{(1)}(\beta r)$ and $H_n^{(2)}(\beta r)$ denotes the Hankel functions of the first and second kind, respectively. $J_n(\beta r)$ is the n-th order Bessel function of the first kind, and $N_n(\beta r)$ is the n-th order Neuman function.The outward or inward propagation characteristics represented by Hankel functions are best understood by looking at their large argument approximations [81-82]:

$$H_n^{(1)}(\beta r) \rightarrow \sqrt{\frac{2}{\pi\beta r}}\, e^{j(\beta r - n\frac{\pi}{2} - \frac{\pi}{4})} \tag{1.7a}$$

$$H_n^{(2)}(\beta r) \rightarrow \sqrt{\frac{2}{\pi\beta r}}\, e^{-j(\beta r - n\frac{\pi}{2} - \frac{\pi}{4})} \tag{1.7b}$$

for $\beta r >> 1$. Thus, $H_n^{(1)}(\beta r)$ describes inward-propagating waves, and $H_n^{(2)}(\beta r)$ outward-propagating waves. Eqs.(1.7a)-(1.7b) resemble very much the propagation of slab modes which is represented by the exponential function $\exp(-j\beta z)$ for z-propagating modes except that the cylindrical waves are decaying waves.

Substituting R, Φ and Z into Eq.(1.3), the solution of the scalar wave equation (1.1) can therefore be written in the following form

$$\psi_{\mu n}^{(p)\sigma}(r,\theta,z) = A_{\mu n}^{(p)\sigma} R_n^{(p)}(\beta_\mu^{(p)} r)\, Z_\mu^\sigma(z)\, e^{j n\theta} \tag{1.8}$$

where a normalization constant $A_{\mu n}^{(p)\sigma}$ is introduced. The subscript " μ " denotes the slab mode number and the subscript " n " the order of the cylindrical wave; the superscript " p " represents outward-propagating waves when p = + and inward propagating waves when p = - ; the superscript " σ " denotes the polarization of the wave, σ = TE or TM.

Similarly to the case of circular optical fibers, the radial and the azimuthal components of the electromagnetic field are obtained from E_z and H_z [74]:

$$E_r = \frac{1}{\beta^2}\left[\frac{\partial^2 E_z}{\partial z \partial r} - \frac{j\omega\mu_0 \partial H_z}{r \quad \partial\theta}\right]$$

$$E_\theta = \frac{1}{\beta^2}\left[\frac{1}{r}\frac{\partial^2 E_z}{\partial\theta\partial z} + j\omega\mu_0\frac{\partial H_z}{\partial r}\right]$$

$$H_r = \frac{1}{\beta^2}\left[\frac{j\omega\varepsilon_0\varepsilon}{r}\frac{\partial E_z}{\partial\theta} + \frac{\partial^2 H_z}{\partial r\partial z}\right]$$

$$H_\theta = \frac{1}{\beta^2}\left[-j\omega\varepsilon_0\varepsilon\frac{\partial E_z}{\partial r} + \frac{1}{r}\frac{\partial^2 H_z}{\partial\theta\partial z}\right] \qquad (1.9)$$

From our knowledge on planar waveguides[67, 74-76], we know that only two kinds of waves can be supported in a planar waveguide, the one with $E_z = 0$ and $H_z \neq 0$, and the other with $E_z \neq 0$ and $H_z = 0$. We call the former the TE-waves, and the latter TM-waves. Using this definition in Eq.(1.9), the TE-waves satisfy:

$$E_r = -\frac{j\omega\mu_0}{\beta^2}\frac{1}{r}\frac{\partial H_z}{\partial\theta}$$

$$E_\theta = \frac{j\omega\mu_0}{\beta^2}\frac{\partial H_z}{\partial r}$$

$$H_r = \frac{1}{\beta^2}\frac{\partial^2 H_z}{\partial r \partial z}$$

$$H_\theta = \frac{1}{\beta^2}\frac{1}{r}\frac{\partial^2 H_z}{\partial \theta \partial z} \qquad (1.10)$$

and likewise, for TM-waves, we have

$$E_r = \frac{1}{\beta^2}\frac{\partial^2 E_z}{\partial z \partial r}$$

$$E_\theta = \frac{1}{\beta^2}\frac{1}{r}\frac{\partial^2 E_z}{\partial \theta \partial z}$$

$$H_r = \frac{j\omega\varepsilon_0\varepsilon}{\beta^2}\frac{1}{r}\frac{\partial E_z}{\partial \theta}$$

$$H_\theta = -\frac{j\omega\varepsilon_0\varepsilon}{\beta^2}\frac{\partial E_z}{\partial r} \qquad (1.11)$$

Substituting Eq.(1.8) into Eq.(1.10) and Eq.(1.11), we obtain the field distribution of TE cylindrical waves

$$E_{\mu n\, z}^{(p)TE} = 0$$

$$H_{\mu n\, z}^{(p)TE} = A_{\mu n}^{(p)TE} R_n^{(p)}(\beta_\mu^{TE} r)\, Z_\mu^{TE}(z)\, e^{jn\theta}$$

$$E_{\mu n\, r}^{(p)TE} = A_{\mu n}^{(p)TE} \frac{n\omega\mu_0}{(\beta_\mu^{TE})^2}\frac{1}{r} R_n^{(p)}(\beta_\mu^{TE} r)\, Z_\mu^{TE}(z)\, e^{jn\theta}$$

$$E_{\mu n\,\theta}^{(p)TE} = A_{\mu n}^{(p)TE} \frac{j\omega\mu_0}{(\beta_\mu^{TE})^2} \frac{dR_n^{(p)TE}(\beta_\mu^{TE} r)}{dr} Z_\mu^{TE}(z)\, e^{jn\theta}$$

$$H_{\mu n\, r}^{(p)TE} = A_{\mu n}^{(p)TE} \frac{1}{(\beta_\mu^{TE})^2} \frac{dR_n^{(p)}(\beta_\mu^{TE} r)}{dr} \frac{dZ_\mu^{TE}}{dz} e^{jn\theta}$$

$$H_{\mu n\,\theta}^{(p)TE} = A_{\mu n}^{(p)TE} \frac{jn}{(\beta_\mu^{TE})^2} \frac{1}{r} R_n^{(p)}(\beta_\mu^{TE} r) \frac{dZ_\mu^{TE}}{dz} e^{jn\theta} \qquad (1.12)$$

Similarly, the field distributions of the TM cylindrical waves are

$$H_{\mu n\, z}^{(p)TM} = 0,$$

$$E_{\mu n\, z}^{(p)TM} = A_{\mu n}^{(p)TM} R_n^{(p)}(\beta_\mu^{TM} r) Z_\mu^{TM}(z)\, e^{jn\theta}$$

$$E_{\mu n\, r}^{(p)TM} = A_{\mu n}^{(p)TM} \left[\frac{1}{(\beta_\mu^{TM})^2}\right] \frac{dR_n^{(p)}(\beta_\mu^{TM} r)}{dr} \frac{dZ_\mu^{TM}(z)}{dz} e^{jn\theta}$$

$$E_{\mu n\,\theta}^{(p)TM} = A_{\mu n}^{(p)TM} \left[\frac{jn}{(\beta_\mu^{TM})^2}\right] \frac{R_n^{(p)}(\beta_\mu^{TM} r)}{r} \frac{dZ_\mu^{TM}(z)}{dz} e^{jn\theta}$$

$$H_{\mu n\, r}^{(p)TM} = -A_{\mu n}^{(p)TM} \left[\frac{n\,\omega_0 \varepsilon_0 \varepsilon}{(\beta_\mu^{TM})^2}\right] \frac{R_n^{(p)}(\beta_\mu^{TM} r)}{r} Z_\mu^{TM}(z)\, e^{jn\theta}$$

$$H_{\mu n\theta}^{(p)TM} = -A_{\mu n}^{(p)TM} \left[\frac{j\,\omega_0 \varepsilon_0 \varepsilon}{(\beta_\mu^{TM})^2}\right] \frac{dR_n^{(p)}(\beta_\mu^{TM} r)}{dr} Z_\mu^{TM}(z)\, e^{jn\theta} \qquad (1.13)$$

The superscripts " TE " and " TM " in Eqs.(1.12)-(1.13) are deliberately added to distinguish the TE and the TM waves.

1.2.2 General Characteristics of Cylindrical Waves

Note that Z(z) is independent of $\Phi(\theta)$ and R(r). This implies that for each slab mode, i.e., for each solution of Z, there are infinitely many cylindrical waves. This also means that the field distribution in the z-direction is the same for all the cylindrical waves associated with the same slab mode

From Eq.(1.12), one can show that

$$\left|\frac{E_{\mu n r}^{(p)TE}}{E_{\mu n \theta}^{(p)TE}}\right| = \left|\frac{H_{\mu n \theta}^{(p)TE}}{H_{\mu n r}^{(p)TE}}\right| = \left(\frac{n}{\beta_{\mu}^{TE} r}\right)\left|\frac{R_n^{(p)}(\beta_{\mu}^{TE} r)}{R_n^{(p)'}(\beta_{\mu}^{TE} r)}\right| \qquad (1.14)$$

where the prime " ' " means differentiation with respect to the argument (βr). Eq.(1.14) indicates that the components $E_{\mu n r}^{(p)TE}$ in the direction of propagation are nonzero except for n=0. We recall that, by definition, the component of a TE slab mode in the direction of propagation is always zero [67]. Therefore, we can say that only the zeroth order TE cylindrical wave resembles the TE slab mode. Nonetherless, the ratio in Eq.(1.14) approaches zero when r —> ∞ due to the asymptotic behavior of R and R' (see Eq. (1.10)). Hence, higher order TE cylindrical waves behave more and more like TE- slab modes as they propagate away from the center. This is to be expected, because at large radius, the cylindrical waves essentially only see the planar waveguide. Similar comments can be made about TM cylindrical waves. In this case, we have

$$\left|\frac{H_{\mu n r}^{(p)TM}}{H_{\mu n \theta}^{(p)TM}}\right| = \left|\frac{E_{\mu n \theta}^{(p)TM}}{E_{\mu n r}^{(p)TM}}\right| = \left(\frac{n}{\beta_{\mu}^{TM} r}\right)\left|\frac{R_n^{(p)}(\beta_{\mu}^{TM} r)}{R_n^{(p)'}(\beta_{\mu}^{TM} r)}\right| \qquad (1.15)$$

$H_{\mu n r}^{(p)TM} = 0$ for n=0 and $H_{\mu n r}^{(p)TM}$ goes to zero for higher order waves as the wave gets far away from the center.

1.2.3 Orthonormality Relations Between Cylindrical Waves

It can be proved that cylindrical waves in an ideal planar waveguides are orthonormal to each other (see Appendix II for details). The orthonormality relations between cylindrical waves can be summarized as :

$$\int_0^{2\pi}\int_{-\infty}^{\infty} r d\theta dz\, \hat{r}.[\mathbf{E}_{vm\,t}^{(q)\tau} \times \mathbf{H}_{\mu n\,t}^{(p)\sigma\,*} + \mathbf{E}_{\mu n\,t}^{(p)\sigma\,*} \times \mathbf{H}_{vm\,t}^{(q)\tau}] = p\,\delta_{v\mu}\delta_{nm}\delta_{pq}\delta_{\sigma\tau} \tag{1.16}$$

where δ is the Kronecker delta, p, q = $\pm$; μ,ν = slab mode number; n, m = order of cylindrical waves; σ,τ = TE or TM.

These relations indicate that cylindrical waves in a uniform planar waveguide are independent of each other. Thus, all the cylindrical waves form a complete basis which can be used to express an arbitary field. This is extremely important in the formulation of the coupled-wave theory in next section.

1.3 Coupled-Wave Theory For Cylindrical Waves

As discussed above, each cylindrical wave in a uniform planar waveguide propagates independent of other cylindrical waves. When a circular grating is introduced in the cladding layer of the guiding structure, the waveguide is no longer the same as the uniform waveguide. The propagation of cylindrical waves is disturbed. Cylindrical waves becomes related to each other. The coupled-wave theory describes how a circular grating affects the propagation of cylindrical waves. This section presents the vector-wave formulation of the coupled-wave equations to be used in the analysis of CG-DFB and CG-DBR lasers in later chapters.

1.3.1 Excitation of Cylindrical Waves

Consider a distribution of sources exciting various cylindrical waves in a waveguide, and represent these sources by the complex amplitude $\mathbf{P}(r,\theta,z)$ of the corresponding induced polarization vector. In the presence of these sources, the complex Maxwell's equations have the form

$$\nabla\times\mathbf{E} = -j\omega\mu_0\mathbf{H} \tag{1.17a}$$

$$\nabla\times\mathbf{H} = j\omega\varepsilon_0\varepsilon\,\mathbf{E} + j\omega\mathbf{P} \tag{1.17b}$$

For two different induced polarizations $\mathbf{P}_1$ and $\mathbf{P}_2$, there are two different fields. To facilitate our derivation, the field corresponding to $\mathbf{P}_1$ is called field 1 and denoted by ($\mathbf{E}_1$, $\mathbf{H}_1$); the field caused by $\mathbf{P}_2$ is field 2 and represented by ($\mathbf{E}_2$, $\mathbf{H}_2$). From Maxwell's equations (1.17), it is easy to verify that

$$\nabla\cdot(\mathbf{E}_1\times\mathbf{H}_2^*+\mathbf{E}_2^*\times\mathbf{H}_1) = -j\omega\mathbf{P}_1\cdot\mathbf{E}_2^* + j\omega\mathbf{P}_2^*\cdot\mathbf{E}_1 \tag{1.18}$$

Setting $\mathbf{P}_2=0$ in Eq.(1.18), we obtain

$$\nabla\cdot(\mathbf{E}_1\times\mathbf{H}_2^*+\mathbf{E}_2^*\times\mathbf{H}_1) = -j\omega\mathbf{P}_1\cdot\mathbf{E}_2^* \tag{1.19}$$

Integrate Eq.(1.19) on both sides over a cylindrical surface that extends to infinity in the z-direction

$$\int_0^{2\pi}\int_{-\infty}^{\infty} r\,d\theta\,dz\;\nabla\cdot(\mathbf{E}_1\times\mathbf{H}_2^*+\mathbf{E}_2^*\times\mathbf{H}_1) = -j\omega\int_0^{2\pi}\int_{-\infty}^{\infty} r\,d\theta\,dz\;\mathbf{P}_1\cdot\mathbf{E}_2^* \tag{1.20}$$

Note that (see the derivation of Eq.(A2.5) in Appendix II)

$$\int_0^{2\pi}\int_{-\infty}^{\infty} r\,d\theta\,dz\;\nabla\cdot(\mathbf{E}_1\times\mathbf{H}_2^*+\mathbf{E}_2^*\times\mathbf{H}_1)$$

$$= \oint \mathbf{dl}.(\mathbf{E}_1\times\mathbf{H}_2^*+\mathbf{E}_2^*\times\mathbf{H}_1)_t + \int_0^{2\pi}\int_{-\infty}^{\infty} d\theta dz \frac{\partial}{\partial r}[\,r\,(\mathbf{E}_1\times\mathbf{H}_2^*+\mathbf{E}_2^*\times\mathbf{H}_1)_r]$$

$$= \int_0^{2\pi}\int_{-\infty}^{\infty} d\theta dz \frac{\partial}{\partial r}[\,r\,(\mathbf{E}_1\times\mathbf{H}_2^*+\mathbf{E}_2^*\times\mathbf{H}_1)_r] \qquad (1.21)$$

where the subscript " t " means the transverse components, i.e the θ and the z components and the subscript "r" indicates the r-component. The contour integral vanishes if at least one of the two waves is a guided wave with fields exponentially decaying toward infinity along the z-direction. The contour integral also goes to zero when both waves are radiation waves, due to the oscillatory nature of the radiation fields [75].

Since

$$(\mathbf{E}_1\times\mathbf{H}_2^*+\mathbf{E}_2^*\times\mathbf{H}_1)_r = (\mathbf{E}_{1t}\times\mathbf{H}_{2t}^*+\mathbf{E}_{2t}^*\times\mathbf{H}_{1t})\,.\,\hat{r} \qquad (1.22)$$

we obtain, from Eqs.(1.20-1.22)

$$\int_0^{2\pi}\int_{-\infty}^{\infty} d\theta dz \frac{\partial}{\partial r}[\,r\,(\mathbf{E}_{1t}\times\mathbf{H}_{2t}^*+\mathbf{E}_{2t}^*\times\mathbf{H}_{1t})\,.\,\hat{r}] = -j\omega\int_0^{2\pi}\int_{-\infty}^{\infty} r d\theta dz\,(\mathbf{P}_1\,.\,\mathbf{E}_2^*) \qquad (1.23)$$

1.3.2 Field Distribution in Terms of Cylindrical Waves

Let field 1 be an arbitrary field. Its transverse (θ, z) components can be expanded in terms of the cylindrical waves in an ideal planar waveguide as

$$\mathbf{E}_{1t}(r,\theta,z) = \sum_{q,\tau,\nu,m} a_{\nu m}^{(q)\tau}(r)\,\mathbf{E}_{\nu m\,t}^{(q)\tau}(r,\theta,z)$$

$$\mathbf{H}_{1t}(r,\theta,z) = \sum_{q,\tau,\nu,m} a_{\nu m}^{(q)\tau}(r)\,\mathbf{H}_{\nu m\,t}^{(q)\tau}(r,\theta,z) \qquad (1.24)$$

where q = ± represents outward waves or inward waves, respectively; τ=TE, TM, denotes the polarization of the wave; ν is the slab mode number (ν=0,1,2,...) and m denotes the order of the cylindrical wave (m=0, ±1, ±2,...). The expansion in Eq.(1.24) includes also the integration over radiation cylindrical waves (with ν being continuous). The radiation cylindrical waves are related to radiation modes of the slab waveguide. To simplify our notation, the continuum is not written out explicitly.

Let field 2 be one of the cylindrical waves, i.e

$$\mathbf{E}_{2t}(r,\theta,z) = \mathbf{E}^{(p)\sigma}_{\mu n\, t}(r,\theta,z)$$

$$\mathbf{H}_{2t}(r,\theta,z) = \mathbf{H}^{(p)\sigma}_{\mu n\, t}(r,\theta,z) \tag{1.25}$$

Substituting Eq.(1.24) and Eq.(1.25) into Eq.(1.23), and making use of the orthonormality relations Eq.(1.16), we obtain

$$\int_0^{2\pi}\int_{-\infty}^{\infty} d\theta dz \frac{\partial}{\partial r}[\, r\,(\mathbf{E}_{1t}\times\mathbf{H}^{*}_{2t}+\mathbf{E}^{*}_{2t}\times\mathbf{H}_{1t})\,.\,\hat{r}]$$

$$=\int_0^{2\pi}\int_{-\infty}^{\infty} d\theta dz \frac{\partial}{\partial r}[\, r \sum_{q,\tau,\nu,m} a^{(q)\tau}_{\nu m}(r)\,(\mathbf{E}^{(q)\tau}_{\nu m\, t}\times\mathbf{H}^{(p)\sigma *}_{\mu n\, t}+\mathbf{E}^{(p)\sigma *}_{\mu n\, t}\times\mathbf{H}^{(q)\tau}_{\nu m\, t})\,.\,\hat{r}]$$

$$= \sum_{q,\tau,\nu,m} \frac{\partial}{\partial r}\{\, a^{(q)\tau}_{\nu m}(r)\int_0^{2\pi}\int_{-\infty}^{\infty} r d\theta dz\ [\ (\mathbf{E}^{(q)\tau}_{\nu m\, t}\times\mathbf{H}^{(p)\sigma *}_{\mu n\, t}+\mathbf{E}^{(p)\sigma *}_{\mu n\, t}\times\mathbf{H}^{(q)\tau}_{\nu m\, t})\,.\,\hat{r}]\}$$

$$= \sum_{q,\tau,\nu,m} \frac{\partial}{\partial r}\{\, a^{(q)\tau}_{\nu m}(r)\, p\, \delta_{qp}\delta_{mn}\delta_{\sigma\tau}\delta_{\nu\mu}\}$$

$$= p\frac{da^{(p)\sigma}_{\mu n}}{dr} \tag{1.26}$$

Hence,

$$p\frac{da_{\mu n}^{(p)\sigma}}{dr} = -j\omega\int_0^{2\pi}\int_{-\infty}^{\infty} r\, d\theta dz\, [\mathbf{P}_1 \cdot \mathbf{E}_{\mu n}^{(p)\sigma *}(r,\theta,z)] \tag{1.27}$$

If $\mathbf{P}_1 = 0$, i.e, when no sources (in other words, no perturbations) are present, there is no change in the amplitude of the cylindrical waves. It should be emphasized that the above relations are exact; no assumptions about the magnitude of the perturbations have been made.

1.3.3 Waveguide Deformations

We have seen in Eq.(1.27) that the variation of the amplitude of a cylindrical wave is related to the polarization vector $\mathbf{P}_1$ which can be brought about by a variety of physical effects. Consider the polarization induced by the difference $\Delta\varepsilon(r,\theta,z)$ of the actual dielectric constant (waveguide with circular gratings) from the ideal distribution (uniform waveguide without gratings), then

$$\mathbf{P}_1 = \varepsilon_0 \Delta\varepsilon\, \mathbf{E}_1 \tag{1.28}$$

which is proportional to the field $\mathbf{E}_1$ in the actual waveguide.

It is easily shown (see Appendix I) that the radial component $\mathbf{E}_{1r}$ of the field can be expressed with the help of transverse components (i.e. the θ- and the z-components) as

$$\mathbf{E}_{1r} = \frac{1}{j\omega\varepsilon_0(\varepsilon+\Delta\varepsilon)}\left[\nabla_t \times \mathbf{H}_{1t} - \frac{H_{1\theta}}{r}\hat{z}\right]$$

$$= \frac{1}{j\omega\varepsilon_0(\varepsilon+\Delta\varepsilon)}\left[\nabla_t \times \sum_{q,\tau,\nu,m} a_{\nu m}^{(q)\tau}(r)\, \mathbf{H}_{\nu m\, t}^{(q)\tau}(r,\theta,z) - \sum_{q,\tau,\nu,m} a_{\nu m}^{(q)\tau}(r)\, \frac{H_{\nu m\, \theta}^{(q)\tau}}{r}\hat{z}\right]$$

$$= \frac{1}{j\omega\varepsilon_0(\varepsilon+\Delta\varepsilon)} \sum_{q,\tau,\nu,m} a_{\nu m}^{(q)\tau}(r) \left[\nabla_t \times \mathbf{H}_{\nu m\, t}^{(q)\tau}(r,\theta,z) - \frac{H_{\nu m\, \theta}^{(q)\tau}}{r} \hat{z} \right]$$

$$= \frac{1}{j\omega\varepsilon_0(\varepsilon+\Delta\varepsilon)} \sum_{q,\tau,\nu,m} a_{\nu m}^{(q)\tau}(r) \left[j\,\omega\,\varepsilon_0\,\varepsilon\,\mathbf{E}_{\nu m\, r}^{(q)\tau} \right]$$

$$= \frac{\varepsilon}{(\varepsilon+\Delta\varepsilon)} \sum_{q,\tau,\nu,m} a_{\nu m}^{(q)\tau}(r)\, \mathbf{E}_{\nu m\, r}^{(q)\tau} \qquad (1.29)$$

which, together with Eq.(1.24), yields

$$\mathbf{P}_1 = \varepsilon_0\,\Delta\varepsilon\,(\mathbf{E}_{1t} + \mathbf{E}_{1r})$$

$$= \varepsilon_0\,\Delta\varepsilon \left[\sum_{q,\tau,\nu,m} a_{\nu m}^{(q)\tau}(r)\, \mathbf{E}_{\nu m\, t}^{(q)\tau} + \frac{\varepsilon}{(\varepsilon+\Delta\varepsilon)} \sum_{q,\tau,\nu,m} a_{\nu m}^{(q)\tau}(r)\, \mathbf{E}_{\nu m\, r}^{(q)\tau} \right]$$

$$= \varepsilon_0\,\Delta\varepsilon \sum_{q,\tau,\nu,m} a_{\nu m}^{(q)\tau}(r) \left[\mathbf{E}_{\nu m\, t}^{(q)\tau} + \frac{\varepsilon}{(\varepsilon+\Delta\varepsilon)} \mathbf{E}_{\nu m\, r}^{(q)\tau} \right] \qquad (1.30)$$

1.3.4 Coupled-Wave Equations

These equations can be easily derived from Eq.(1.27) and Eq.(1.30). Putting $\mathbf{P}_1$ of Eq.(1.30) into Eq.(1.27), we get

$$p \frac{da_{\mu n}^{(p)\sigma}}{dr} = -j\omega \int_0^{2\pi} \int_{-\infty}^{\infty} r\, d\theta dz \left\{ \varepsilon_0\,\Delta\varepsilon \sum_{q,\tau,\nu,m} a_{\nu m}^{(q)\tau}(r) \left[\mathbf{E}_{\nu m\, t}^{(q)\tau} + \frac{\varepsilon}{(\varepsilon+\Delta\varepsilon)} \mathbf{E}_{\nu m\, r}^{(q)\tau} \right] \right\} \cdot \mathbf{E}_{\mu n}^{(p)\sigma *}$$

$$= -j \sum_{q,\tau,\nu,m} a_{\nu m}^{(q)\tau}(r)\, \omega\, \varepsilon_0 \int_0^{2\pi} \int_{-\infty}^{\infty} r\, d\theta dz\ \Delta\varepsilon \left[\mathbf{E}_{\nu m\, t}^{(q)\tau} \cdot \mathbf{E}_{\mu n\, t}^{(p)\sigma *} + \frac{\varepsilon}{(\varepsilon+\Delta\varepsilon)} \mathbf{E}_{\nu m\, r}^{(q)\tau} \cdot \mathbf{E}_{\mu n\, r}^{(p)\sigma *} \right]$$

$$= -j \sum_{q,\tau,\nu,m} K_{\mu n,\nu m}^{(p)\sigma,(q)\tau} a_{\nu m}^{(q)\tau}(r) \qquad (1.31)$$

where the coupling coefficients are defined by

$$K_{\mu n,\nu m}^{(p)\sigma,(q)\tau} = \omega\, \varepsilon_0 \int_0^{2\pi} \int_{-\infty}^{\infty} r\, d\theta dz\ \Delta\varepsilon \left[\mathbf{E}_{\nu m\, t}^{(q)\tau} \cdot \mathbf{E}_{\mu n\, t}^{(p)\sigma *} + \frac{\varepsilon}{(\varepsilon+\Delta\varepsilon)} \mathbf{E}_{\nu m\, r}^{(q)\tau} \cdot \mathbf{E}_{\mu n\, r}^{(p)\sigma *} \right] \qquad (1.32)$$

From Eq.(1.32), we deduce that

$$K_{\mu n,\nu m}^{(p)\sigma,(q)\tau} = (K_{\nu m,\mu n}^{(q)\tau,(p)\sigma})^* \qquad (1.33)$$

i.e.

$$K_{\mu n,\nu m}^{(+)\sigma,(+)\tau} = (K_{\nu m,\mu n}^{(+)\tau,(+)\sigma})^*$$

$$K_{\mu n,\nu m}^{(+)\sigma,(-)\tau} = (K_{\nu m,\mu n}^{(-)\tau,(+)\sigma})^*$$

$$K_{\mu n,\nu m}^{(-)\sigma,(+)\tau} = (K_{\nu m,\mu n}^{(+)\tau,(-)\sigma})^*$$

$$K_{\mu n,\nu m}^{(-)\sigma,(-)\tau} = (K_{\nu m,\mu n}^{(-)\tau,(-)\sigma})^* \qquad (1.34)$$

for lossless medium.

Writing down explicitly the equations for the outward-propagating waves (p=+) and the inward-propagating waves (p= -), we have

$$\frac{da_{\mu n}^{(+)\sigma}}{dr} = -j \sum_{\tau,\nu,m} [\, K_{\mu n,\nu m}^{(+)\sigma,(+)\tau}\, a_{\nu m}^{(+)\tau} + K_{\mu n,\nu m}^{(+)\sigma,(-)\tau}\, a_{\nu m}^{(-)\tau} \,] \tag{1.35a}$$

$$\frac{da_{\mu n}^{(-)\sigma}}{dr} = j \sum_{\tau,\nu,m} [\, K_{\mu n,\nu m}^{(-)\sigma,(+)\tau}\, a_{\nu m}^{(+)\tau} + K_{\mu n,\nu m}^{(-)\sigma,(-)\tau}\, a_{\nu m}^{(-)\tau} \,] \tag{1.35b}$$

The coupled-wave theory that we have just formulated is in fact self-consistent, that is to say, that the total power carried by all the waves is conserved. The proof of self-consistency is presented in Appendix III.

Eqs.(1.35) and Eq.(1.32) actually are very similar to the coupled-mode equations for conventional waveguides [67, 76] except that here the summation includes the TE and TM polarizations, while in conventional theories the TE and TM modes are normally not coupled. One should notice though that the coupling coefficients for cylindrical waves are different from those for plane waves, as to be seen in the next section.

1.4. Coupling Coefficients for Circular Gratings

A lot of physical insight can be obtained by just examining the coupling coefficients since they are the key parameters in the coupling process between different waves. From section 1.3, we know that the couplings between cylindrical waves are governed by Eqs.(1.35) and the coupling coefficients are defined by Eq.(1.32). For simplicity, we assume that the grating is circularly symmetric as shown in Fig.4 and the permittivity variation is expressed by $\Delta\varepsilon(r,\theta,z) = \Delta\varepsilon(r,z)$.

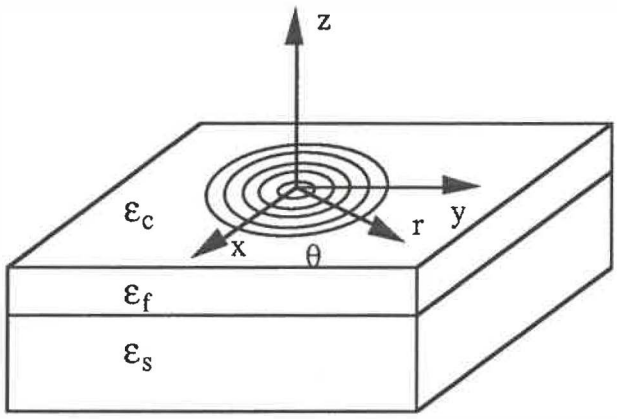

Fig.4 Circularly symmetric grating fabricated on planar dielectric waveguide with perturbation : $\Delta\varepsilon(r,\theta,z) = \Delta\varepsilon(r,z) \neq 0$.

1.4.1 TE-TE Coupling Coefficients

For this case, $\sigma=\tau=TE$, substituting the field distributions (see Eq.(1.12)) of TE cylindrical waves into Eq.(1.32), we have

$$K_{\mu n,\nu m}^{(p)TE,(q)TE} = \omega\varepsilon_0 \int_0^{2\pi}\int_{-\infty}^{\infty} r\, d\theta dz\ \Delta\varepsilon \{ A_{\nu m}^{(q)TE} \frac{j\omega\mu_0}{(\beta_\nu^{TE})^2} \frac{dR_m^{(q)TE}(\beta_\nu^{TE} r)}{dr} Z_\nu^{TE}(z)\, e^{jm\theta}$$

$$\cdot A_{\mu n}^{(p)TE*} \frac{(-j\omega\mu_0)}{(\beta_\mu^{TE})^2} \frac{dR_n^{(p)TE*}(\beta_\mu^{TE} r)}{dr} Z_\mu^{TE*}(z)\, e^{-jn\theta}$$

$$+ \frac{\varepsilon}{(\varepsilon+\Delta\varepsilon)} A_{\nu m}^{(q)TE} \frac{m\omega\mu_0}{(\beta_\nu^{TE})^2} \frac{1}{r} R_m^{(q)}(\beta_\nu^{TE} r)\, Z_\nu^{TE}(z) e^{jm\theta}$$

$$\cdot A_{\mu n}^{(p)TE*} \frac{n\omega\mu_0}{(\beta_\mu^{TE})^2} \frac{1}{r} R_n^{(p)*}(\beta_\mu^{TE} r)\, Z_\mu^{TE*}(z)\, e^{-jn\theta}\}$$

$$= A_{\nu m}^{(q)TE} A_{\mu n}^{(p)TE*} \frac{(\omega^2 \varepsilon_0 \mu_0)(\omega \mu_0)}{(\beta_\nu^{TE} \beta_\mu^{TE} 2)} \int_0^{2\pi} \int_{-\infty}^{\infty} e^{j(m-n)\theta} \Delta\varepsilon \, Z_\nu^{TE}(z) Z_\mu^{TE*}(z) \, r \, d\theta dz \, .$$

$$\{ \frac{dR_m^{(q)TE}(\beta_\nu^{TE} r)}{dr} \frac{dR_n^{(p)TE*}(\beta_\mu^{TE} r)}{dr} + \frac{\varepsilon}{\varepsilon+\Delta\varepsilon} (\frac{n}{r})(\frac{m}{r}) R_m^{(q)TE}(\beta_\nu^{TE} r) R_n^{(p)TE*}(\beta_\mu^{TE} r) \}$$

$$= \delta_{nm} 2\pi r \, A_{\nu m}^{(q)TE} A_{\mu n}^{(p)TE*} \frac{(\omega^2 \varepsilon_0 \mu_0)(\omega \mu_0)}{(\beta_\nu^{TE} \beta_\mu^{TE} 2)} \int_{-\infty}^{\infty} dz \, \Delta\varepsilon(r,z) \, Z_\nu^{TE} Z_\mu^{TE*} \, .$$

$$\{ \frac{dR_m^{(q)TE}(\beta_\nu^{TE} r)}{dr} \frac{dR_n^{(p)TE*}(\beta_\mu^{TE} r)}{dr} + \frac{\varepsilon}{\varepsilon+\Delta\varepsilon} (\frac{n}{r})(\frac{m}{r}) R_m^{(q)TE}(\beta_\nu^{TE} r) R_n^{(p)TE*}(\beta_\mu^{TE} r) \}$$

$$= \delta_{nm} K_{\mu n,\nu n}^{(p,q)TETE} \tag{1.36}$$

where we have defined

$$K_{\mu n,\nu n}^{(p,q)TETE} = 2\pi r \, A_{\nu n}^{(q)TE} A_{\mu n}^{(p)TE*} \frac{(\omega^2 \varepsilon_0 \mu_0^2)}{(\beta_\nu^{TE} \beta_\mu^{TE} 2)(\omega \varepsilon_0)} \int_{-\infty}^{\infty} dz \, \Delta\varepsilon(r,z) \, Z_\nu^{TE} Z_\mu^{TE*}$$

$$\cdot \{ \frac{dR_n^{(q)TE}(\beta_\nu^{TE} r)}{dr} \frac{dR_n^{(p)TE*}(\beta_\mu^{TE} r)}{dr} + \frac{\varepsilon}{\varepsilon+\Delta\varepsilon} (\frac{n}{r})^2 R_n^{(q)TE}(\beta_\nu^{TE} r) R_n^{(p)TE*}(\beta_\mu^{TE} r) \} \tag{1.37}$$

1.4.2 TM-TM Coupling Coefficients

For coupling between TM waves, we have $\sigma=\tau=TM$. Substituting the field distribution of TM waves from Eq.(1.13) into Eq.(1.32), the coupling coefficients are found to be

$$K_{\mu n,\nu m}^{(p)TM,(q)TM} = \delta_{nm} K_{\mu n,\nu n}^{(p,q)TMTM} \tag{1.38}$$

where, as in the case of TE waves, we have defined

$$K_{\mu n,\nu n}^{(p,q)TMTM} = 2\pi r\, A_{\nu n}^{(q)TM} A_{\mu n}^{(p)TM*} \omega\varepsilon_0 \int_{-\infty}^{\infty} dz\, \Delta\varepsilon(r,z)$$

$$\cdot\Big[\frac{n^2}{(\beta_\nu^{TM}\beta_\mu^{TM})^2}\frac{1}{r^2}\frac{dZ_\nu^{TM}}{dz}\frac{dZ_\mu^{TM*}}{dz} R_n^{(q)}(\beta_\nu^{TM} r) R_n^{(p)*}(\beta_\mu^{TM} r) + R_n^{(q)}(\beta_\nu^{TM} r)\, R_n^{(p)*}(\beta_\mu^{TM} r)\, Z_\nu^{TM} Z_\mu^{TM*}$$

$$+\frac{\varepsilon}{\varepsilon+\Delta\varepsilon}\frac{1}{(\beta_\nu^{TM}\beta_\mu^{TM})^2}\frac{dR_n^{(q)}(\beta_\nu^{TM} r)}{dr}\frac{dR_n^{(p)*}(\beta_\mu^{TM} r)}{dr}\frac{dZ_\nu^{TM}}{dz}\frac{dZ_\mu^{TM*}}{dz}\Big] \tag{1.39}$$

1.4.3 TE-TM Coupling Coefficients

Note that in this case we have $\sigma=TE$ and $\tau=TM$. Substituting the field distributions of TE cylindrical waves and TM cylindrical waves from Eq.(1.12) and Eq.(1.13), respectively, into Eq.(1.32), the coupling coefficients are obtained as

$$K_{\mu n,\nu m}^{(p)TE,(q)TM} = \delta_{nm} K_{\mu n,\nu n}^{(p,q)TETM} \tag{1.40}$$

where

$$K_{\mu n,\nu n}^{(p,q)TE,TM} = 2\pi n\, A_{\nu n}^{(q)TM} A_{\mu n}^{(p)TE*} \frac{(\omega^2 \varepsilon_0 \mu_0)}{(\beta_\nu^{TM}\, \beta_\mu^{TE\,2})} \int_{-\infty}^{\infty} dz\, \Delta\varepsilon(r,z)\, \frac{dZ_\nu^{TM}}{dz} Z_\mu^{TE*}$$

$$\cdot \left[R_n^{(q)}(\beta_\nu^{TM} r) \frac{dR_n^{(p)*}(\beta_\mu^{TE} r)}{dr} + \frac{\varepsilon}{\varepsilon+\Delta\varepsilon} \frac{dR_n^{(q)}(\beta_\nu^{TM} r)}{dr} R_n^{(p)*}(\beta_\mu^{TE} r) \right] \tag{1.41}$$

From Eq.(1.33), we get

$$K_{\mu n,\, \nu m}^{(p)TM,(q)TE} = (K_{\nu m,\, \mu n}^{(q)TE,(p)TM})^*$$

$$K_{\mu n,\nu n}^{(p,q)TM,TE} = (K_{\nu n,\mu n}^{(q,p)TE,TM})^* \tag{1.42}$$

1.4.4. Discussion

Substituting the coupling coefficients from Eqs.(1.36), (1.38) , (1.40) and (1.42) into the coupled-wave equations in (1.35), we obtain

$$\frac{da_{\mu n}^{(+)TE}}{dr} = -j \sum_\nu \left[K_{\mu n,\nu n}^{(+,+)TE,TE} a_{\nu n}^{(+)TE} + K_{\mu n,\nu n}^{(+,-)TE,TE} a_{\nu n}^{(-)TE} + K_{\mu n,\nu n}^{(+,+)TE,TM} a_{\nu n}^{(+)TM} + K_{\mu n,\nu n}^{(+,-)TE,TM} a_{\nu n}^{(-)TM} \right]$$

$$\frac{da_{\mu n}^{(-)TE}}{dr} = j \sum_\nu \left[K_{\mu n,\nu n}^{(-,+)TE,TE} a_{\nu n}^{(+)TE} + K_{\mu n,\nu n}^{(-,-)TE,TE} a_{\nu n}^{(-)TE} + K_{\mu n,\nu n}^{(-,+)TE,TM} a_{\nu n}^{(+)TM} + K_{\mu n,\nu n}^{(-,-)TE,TM} a_{\nu n}^{(-)TM} \right]$$

$$\frac{da_{\mu n}^{(+)TM}}{dr} = -j \sum_\nu \left[K_{\mu n,\nu n}^{(+,+)TM,TE} a_{\nu n}^{(+)TE} + K_{\mu n,\nu n}^{(+,-)TM,TE} a_{\nu n}^{(-)TE} + K_{\mu n,\nu n}^{(+,+)TM,TM} a_{\nu n}^{(+)TM} + K_{\mu n,\nu n}^{(+,-)TM,TM} a_{\nu n}^{(-)TM} \right]$$

$$\frac{da_{\mu n}^{(-)TM}}{dr} = j \sum_{\nu} [\, K_{\mu n,\nu n}^{(-,+)TM\,TE}\, a_{\nu n}^{(+)TE} + K_{\mu n,\nu n}^{(-,-)TM\,TE}\, a_{\nu n}^{(-)TE} + K_{\mu n,\nu n}^{(-,+)TM\,TM}\, a_{\nu n}^{(+)TM} + K_{\mu n,\nu n}^{(-,-)TM\,TM}\, a_{\nu n}^{(-)TM} \,] \tag{1.43}$$

These equations show that circular gratings couple only cylindrical waves of the same order. Generally speaking, TE and TM cylindrical waves are coupled together.

A very interesting case is when n=m=0. We find from Eqs.(1.41) and (1.42) that the coupling between TE and TM wave vanishes. For this case, the coupled-wave equations can be separated into two independent sets, one for zeroth-order TE-waves

$$\frac{da_{\mu 0}^{(+)TE}}{dr} = -j \sum_{\nu} [\, K_{\mu 0,\nu 0}^{(+,+)TE\,TE}\, a_{\nu 0}^{(+)TE} + K_{\mu 0,\nu 0}^{(+,-)TE\,TE}\, a_{\nu 0}^{(-)TE} \,]$$

$$\frac{da_{\mu 0}^{(-)TE}}{dr} = j \sum_{\nu} [\, K_{\mu 0,\nu 0}^{(-,+)TE\,TE}\, a_{\nu 0}^{(+)TE} + K_{\mu 0,\nu 0}^{(-,-)TE\,TE}\, a_{\nu 0}^{(-)TE} \,] \tag{1.44}$$

and the other for zeroth-order TM-waves

$$\frac{da_{\mu 0}^{(+)TM}}{dr} = -j \sum_{\nu} [\, K_{\mu 0,\nu 0}^{(+,+)TM\,TM}\, a_{\nu 0}^{(+)TM} + K_{\mu 0,\nu 0}^{(+,-)TM\,TM}\, a_{\nu 0}^{(-)TM} \,]$$

$$\frac{da_{\mu 0}^{(-)TM}}{dr} = j \sum_{\nu} [\, K_{\mu 0,\nu 0}^{(-,+)TM\,TM}\, a_{\nu 0}^{(+)TM} + K_{\mu 0,\nu 0}^{(-,-)TM\,TM}\, a_{\nu 0}^{(-)TM} \,] \tag{1.45}$$

Eqs.(1.44)-(1.45) show that for zeroth-order cylindrical waves, we have pure TE-TE or TM-TM coupling.

For single-mode waveguides, we have $\mu=\nu=0$. Eqs.(1.43)-(1.45) become

$$\frac{da_{0n}^{(+)TE}}{dr} = -j \,[\, K_{0n,0n}^{(+,+)TE\,TE}\, a_{0n}^{(+)TE} + K_{0n,0n}^{(+,-)TE\,TE}\, a_{0n}^{(-)TE} + K_{0n,0n}^{(+,+)TE\,TM}\, a_{0n}^{(+)TM} + K_{0n,0n}^{(+,-)TE\,TM}\, a_{0n}^{(-)TM} \,]$$

$$\frac{da_{0n}^{(-)TE}}{dr} = j\,[\,K_{0n,0n}^{(-,+)TETE} a_{0n}^{(+)TE} + K_{0n,0n}^{(-,-)TETE} a_{0n}^{(-)TE} + K_{0n,0n}^{(-,+)TETM} a_{0n}^{(+)TM} + K_{0n,0n}^{(-,-)TETM} a_{0n}^{(-)TM}]$$

$$\frac{da_{0n}^{(+)TM}}{dr} = -j\,[\,K_{0n,0n}^{(+,+)TMTE} a_{0n}^{(+)TE} + K_{0n,0n}^{(+,-)TMTE} a_{0n}^{(-)TE} + K_{0n,0n}^{(+,+)TMTM} a_{0n}^{(+)TM} + K_{0n,0n}^{(+,-)TMTM} a_{0n}^{(-)TM}]$$

$$\frac{da_{0n}^{(-)TM}}{dr} = j\,[\,K_{0n,0n}^{(-,+)TMTE} a_{0n}^{(+)TE} + K_{0n,0n}^{(-,-)TMTE} a_{0n}^{(-)TE} + K_{0n,0n}^{(-,+)TMTM} a_{0n}^{(+)TM} + K_{0n,0n}^{(-,-)TMTM} a_{0n}^{(-)TM}] \qquad (1.46)$$

for higher order waves with n > 0. And

$$\frac{da_{00}^{(+)TE}}{dr} = -j\,[\,K_{00,00}^{(+,+)TETE} a_{00}^{(+)TE} + K_{00,00}^{(+,-)TETE} a_{00}^{(-)TE}]$$

$$\frac{da_{00}^{(-)TE}}{dr} = j\,[\,K_{00,00}^{(-,+)TETE} a_{00}^{(+)TE} + K_{00,00}^{(-,-)TETE} a_{00}^{(-)TE}]$$

$$\frac{da_{00}^{(+)TM}}{dr} = -j\,[\,K_{00,00}^{(+,+)TMTM} a_{00}^{(+)TM} + K_{00,00}^{(+,-)TMTM} a_{00}^{(-)TM}]$$

$$\frac{da_{00}^{(-)TM}}{dr} = j\,[\,K_{00,00}^{(-,+)TMTM} a_{00}^{(+)TM} + K_{00,00}^{(-,-)TMTM} a_{00}^{(-)TM}] \qquad (1.47)$$

for zeroth-order waves.

We notice that the coupling between zeroth-order cylindrical waves (pure TE-TE or TM-TM coupling) looks very similar to that of two-mode coupling in one-dimensional waveguide [67]. But for n > 0, due to the cross-coupling between TE and TM waves, the situation is much more complicated.

1.5. Summary

A vector coupled-wave theory has been formulated for cylindrical waves in a planar dielectric waveguide. The theory is general and self-consistent. It is shown that only cylindrical waves of the same order (which can belong to different slab modes in the waveguide) are coupled. For zeroth-order waves pure TE-TE or TM-TM coupling occurs. For higher order waves, TE-and TM-cylindrical waves are cross-coupled. The coupled-wave equations for zeroth-order cylindrical waves are similar to those of two-mode coupling in one dimensional waveguides with linear gratings. The coupled-wave equations established in this chapter are valid for both passive and active circular grating devices in integrated optics. In the following chapters, this coupled-wave theory will be applied to study circular grating DFB and DBR lasers.

CHAPTER 2

SIMPLIFIED COUPLED-WAVE EQUATIONS FOR CYLINDRICAL WAVES

2.1 Introduction

A general self-consistent coupled-wave theory has been derived in Chapter 1. The coupled-wave theory is valid for all cylindrical waves (both TE and TM) in multi-mode or single-mode planar waveguides. Because of the inter-polarization coupling between TE and TM cylindrical waves, the coupled-wave equations form a system of four first-order differential equations. This renders the analysis complicated and tedious.

In this chapter, a simplified form of the coupled-wave equations for cylindrical waves is presented. It is shown that under the large radius approximation ($\beta r >> 1$), which covers most practical cases, the inter-polarization coupling between TE and TM cylindrical waves approaches zero. This approximation allows one to break up the system of coupled-wave equations into two independent families, one for TE-cylindrical waves and the other for TM-cylindrical waves. The coupled-wave equations then become similar to those of one dimensional periodic structures. This greatly facilitates the analysis of circular grating devices.

In section 2.2, the coupled-wave equations established in Chapter 1 are briefly reviewed. It is shown that the coupling coefficients can be expressed as the product of a cylindrical factor which is defined by the Hankel functions describing the propagation of the cylindrical waves and a slab-mode coupling coefficient which depends only on the permittivity perturbation created by the grating and the field distributions of the slab modes related to the cylindrical waves. The large radius approximation of the coupled-wave equations is obtained by applying the asymptotic formulae (for $\beta r >> 1$) of Hankel functions to the cylindrical-wave factors. In section 2.3, the special case of circular gratings

on a single-mode planar waveguide is considered. The validity of the large radius approximation is discussed in section 2.4. A comparison between the coupled-wave theory derived in this thesis and those by other authors [63, 65, 66] is also presented in section 2.4.

2.2. Large Radius Approximation of Coupled-Wave Equations

2.2.1 Purpose

To see why simplified coupled-wave equations are needed, we rewrite the coupled-wave equations derived in Chapter 1 as follows,

$$p\frac{da_{\mu n}^{(p)\sigma}}{dr} = -j \sum_{q,\tau,\nu,m} K_{\mu n,\nu m}^{(p)\sigma,(q)\tau} a_{\nu m}^{(q)\tau}(r) \tag{2.1}$$

in which the a's are the amplitudes of the cylindrical waves and the K's are the coupling coefficients defined by

$$K_{\mu n,\nu m}^{(p)\sigma,(q)\tau} = \omega \varepsilon_0 \int_0^{2\pi} \int_{-\infty}^{\infty} r \, d\theta dz \; \Delta\varepsilon \left[\mathbf{E}_{\nu m\, t}^{(q)\tau} \cdot \mathbf{E}_{\mu n\, t}^{(p)\sigma *} + \frac{\varepsilon}{(\varepsilon+\Delta\varepsilon)} \mathbf{E}_{\nu m\, r}^{(q)\tau} \cdot \mathbf{E}_{\mu n\, r}^{(p)\sigma *} \right] \tag{2.2}$$

When the grating has circular symmetry, the coupling coefficients can be written as (see Section 1.4):

$$K_{\mu n,\nu m}^{(p)\sigma,(q)\tau} = \delta_{nm} K_{\mu n,\nu n}^{(p,q)\sigma\tau} \tag{2.3}$$

where δ is the Kronecker delta, and the K's on the right-hand side are the coupling coefficients between cylindrical waves of the same order defined by Eqs.(1.37), (1.39) and (1.41) in Chapter 1.

Substituting Eq.(2.3) into Eq.(2.1) and writing down the results explicitly , we have

$$\frac{da_{\mu n}^{(+)TE}}{dr} = -j \sum_{\nu} [\, K_{\mu n,\nu n}^{(+,+)TE\,TE}\, a_{\nu n}^{(+)TE} + K_{\mu n,\nu n}^{(+,-)TE\,TE}\, a_{\nu n}^{(-)TE} + K_{\mu n,\nu n}^{(+,+)TE\,TM}\, a_{\nu n}^{(+)TM} + K_{\mu n,\nu n}^{(+,-)TE\,TM}\, a_{\nu n}^{(-)TM} \,] \tag{2.4a}$$

$$\frac{da_{\mu n}^{(-)TE}}{dr} = j \sum_{\nu} [\, K_{\mu n,\nu n}^{(-,+)TE\,TE}\, a_{\nu n}^{(+)TE} + K_{\mu n,\nu n}^{(-,-)TE\,TE}\, a_{\nu n}^{(-)TE} + K_{\mu n,\nu n}^{(-,+)TE\,TM}\, a_{\nu n}^{(+)TM} + K_{\mu n,\nu n}^{(-,-)TE\,TM}\, a_{\nu n}^{(-)TM} \,] \tag{2.4b}$$

$$\frac{da_{\mu n}^{(+)TM}}{dr} = -j \sum_{\nu} [\, K_{\mu n,\nu n}^{(+,+)TM\,TE}\, a_{\nu n}^{(+)TE} + K_{\mu n,\nu n}^{(+,-)TM\,TE}\, a_{\nu n}^{(-)TE} + K_{\mu n,\nu n}^{(+,+)TM\,TM}\, a_{\nu n}^{(+)TM} + K_{\mu n,\nu n}^{(+,-)TM\,TM}\, a_{\nu n}^{(-)TM} \,] \tag{2.4c}$$

$$\frac{da_{\mu n}^{(-)TM}}{dr} = j \sum_{\nu} [\, K_{\mu n,\nu n}^{(-,+)TM\,TE}\, a_{\nu n}^{(+)TE} + K_{\mu n,\nu n}^{(-,-)TM\,TE}\, a_{\nu n}^{(-)TE} + K_{\mu n,\nu n}^{(-,+)TM\,TM}\, a_{\nu n}^{(+)TM} + K_{\mu n,\nu n}^{(-,-)TM\,TM}\, a_{\nu n}^{(-)TM} \,] \tag{2.4d}$$

The inter-polarization coupling between TE and TM cylindrical waves makes the coupled-wave equations take the form of a 4th-order linear differential system. To solve Eqs.(2.4) analytically will be very difficult or even impossible if no approximation is made. The complexity in the expressions of the coupling coefficients (see section 1.4) renders the problem more unwieldy. Thus, in order to facilitate the analysis of circular grating devices, simplification of the coupled-wave equations is necessary. It is especially helpful if the TE and TM cylindrical waves can be decoupled.

2.2.2 Coupling Coefficients and Cylindrical Wave Factors

As the coupling coefficients are the key to the coupled-wave equations, it is natural to start with them. By using the properties of the Hankel functions, one can show (see Appendix IV) that for small perturbations with $\Delta\varepsilon/(\varepsilon+\Delta\varepsilon) \ll 1$, the coupling coefficients in Eqs.(2.4) can be expressed by

$$K_{\mu n,\nu n}^{(p,q)\sigma\tau} = F_{\mu n,\nu n}^{(p,q)\sigma\tau}(r)\, K_{\mu,\nu}^{\sigma\tau}(r) \qquad (\text{for } \sigma = \tau = \text{TE or } \sigma \neq \tau) \tag{2.5a}$$

$$= \tilde{F}^{(p,q)\sigma\tau}_{\mu n,\nu n}(r)\,\tilde{K}^{\sigma\tau}_{\mu,\nu}(r) + F^{(p,q)\sigma\tau}_{\mu n,\nu n}(r)\,K^{\sigma\tau}_{\mu,\nu}(r) \qquad (\sigma=\tau=\mathrm{TM}) \qquad (2.5b)$$

The F's in Eq.(2.5) are called the cylindrical-wave factors which are equivalent to the plane-wave phase factor $\exp[\pm j(\beta_\mu \pm \beta_\nu)z]$ in conventional coupled-mode theory [67] (see also section 2.2.3). The cylindrical-wave factors are defined by

$$F^{(p,q)\sigma\tau}_{\mu n,\nu n}(r) = \frac{\pi r}{4}\sqrt{\beta^{\sigma}_{\mu}\beta^{\tau}_{\nu}}\;\left[\, R^{(p)*}_{n-1}(\beta^{\sigma}_{\mu}r)\,R^{(q)}_{n-1}(\beta^{\tau}_{\nu}r) \pm R^{(p)*}_{n+1}(\beta^{\sigma}_{\mu}r)\,R^{(q)}_{n+1}(\beta^{\tau}_{\nu}r)\,\right]$$
$$(+ \text{ sign for } \sigma=\tau \text{ ; - sign for } \sigma\neq\tau) \qquad (2.6a)$$

$$\tilde{F}^{(p,q)\sigma\tau}_{\mu n,\nu n}(r) = \frac{\pi r}{2}\sqrt{\beta^{\sigma}_{\mu}\beta^{\tau}_{\nu}}\;R^{(p)*}_{n}(\beta^{\sigma}_{\mu}r)\,R^{(q)}_{n}(\beta^{\tau}_{\nu}r) \qquad (\sigma=\tau=\mathrm{TM}) \qquad (2.6b)$$

where the β's are the propagation constants of planar waveguide modes and the R's describe the radial dependence of the cylindrical waves with

$$R^{(+)}_{n}(\beta r) = H^{(2)}_{n}(\beta r) = J_n(\beta r) - jN_n(\beta r) \qquad (2.7a)$$

$$R^{(-)}_{n}(\beta r) = H^{(1)}_{n}(\beta r) = J_n(\beta r) + jN_n(\beta r) \qquad (2.7b)$$

The $H^{(1)}_n(\beta r)$ and $H^{(2)}_n(\beta r)$ in Eqs.(2.7) are the Hankel functions of the first and second kind, the $J_n(\beta r)$ and $N_n(\beta r)$ denote the Bessel functions of the first and second kind, respectively.

The K's and $\tilde{K}$'s in Eqs.(2.5) depends only on the overlap integrals of the slab guide modes with the grating. They are defined by

$$K^{\mathrm{TE}\,\mathrm{TE}}_{\mu\nu}(r) = \frac{k_0^2}{2\sqrt{\beta^{\mathrm{TE}}_{\mu}\beta^{\mathrm{TE}}_{\nu}}}\;\frac{\displaystyle\int_{-\infty}^{\infty}\Delta\varepsilon(r,z)\,Z^{\mathrm{TE}*}_{\mu}\,Z^{\mathrm{TE}}_{\nu}\,dz}{\sqrt{\displaystyle\int_{-\infty}^{\infty}\left|Z^{\mathrm{TE}}_{\mu}\right|^2 dz\int_{-\infty}^{\infty}\left|Z^{\mathrm{TE}}_{\nu}\right|^2 dz}} \qquad (2.8a)$$

$$\tilde{K}_{\mu\nu}^{TM\,TM}(r) = \frac{\sqrt{\beta_\mu^{TM}\,\beta_\nu^{TM}}}{2} \frac{\int_{-\infty}^{\infty} \Delta\varepsilon(r,z)\, Z_\mu^{TM*}\, Z_\nu^{TM}\, dz}{\sqrt{\int_{-\infty}^{\infty} \varepsilon \left|Z_\mu^{TM}\right|^2 dz \int_{-\infty}^{\infty} \varepsilon \left|Z_\nu^{TM}\right|^2 dz}} \tag{2.8b}$$

$$K_{\mu\nu}^{TM\,TM}(r) = \frac{1}{2\sqrt{\beta_\mu^{TM}\,\beta_\nu^{TM}}} \frac{\int_{-\infty}^{\infty} \Delta\varepsilon(r,z) \left(\frac{dZ_\mu^{TM*}}{dz}\right)\left(\frac{dZ_\nu^{TM}}{dz}\right) dz}{\sqrt{\int_{-\infty}^{\infty} \varepsilon \left|Z_\mu^{TM}\right|^2 dz \int_{-\infty}^{\infty} \varepsilon \left|Z_\nu^{TM}\right|^2 dz}} \tag{2.8c}$$

$$K_{\mu\nu}^{TE\,TM}(r) = \frac{k_0}{2\sqrt{\beta_\mu^{TE}\,\beta_\nu^{TM}}} \frac{\int_{-\infty}^{\infty} \Delta\varepsilon(r,z)\, Z_\mu^{TE*} \left(\frac{dZ_\nu^{TM}}{dz}\right) dz}{\sqrt{\int_{-\infty}^{\infty} \left|Z_\mu^{TE}\right|^2 dz \int_{-\infty}^{\infty} \varepsilon \left|Z_\nu^{TM}\right|^2 dz}} \tag{2.8d}$$

$$K_{\mu\nu}^{TM\,TE}(r) = \frac{k_0}{2\sqrt{\beta_\mu^{TM}\,\beta_\nu^{TE}}} \frac{\int_{-\infty}^{\infty} \Delta\varepsilon(r,z) \left(\frac{dZ_\mu^{TM*}}{dz}\right) Z_\nu^{TE}\, dz}{\sqrt{\int_{-\infty}^{\infty} \varepsilon \left|Z_\mu^{TM}\right|^2 dz \int_{-\infty}^{\infty} \left|Z_\nu^{TE}\right|^2 dz}} \tag{2.8e}$$

where $k_0 = \omega\sqrt{\mu_0 \varepsilon_0}$ is the wave number of light in vacuum and the Z's describe the corresponding modal field distributions in the z-direction.

By comparing with the conventional coupled-mode theory [67], we realize that $K_{\mu\nu}^{TE\,TE}(r)$ is actually the coupling coefficient between TE slab modes, while $\tilde{K}_{\mu\nu}^{TM\,TM}(r)$ and $K_{\mu\nu}^{TM\,TM}(r)$ are the transverse and the longitudinal coupling coefficients of TM modes in a perturbed planar waveguide [83], respectively.

As expressed by Eq.(2.5a), the coupling coefficients for TE-cylindrical waves are the product of two terms, the cylindrical-wave factor $F_{\mu n,\nu n}^{(p,q)TE\,TE}(r)$ and the coupling coefficient between TE slab modes $K_{\mu\nu}^{TE\,TE}(r)$. Similar remarks apply to the TM cylindrical waves, except that the coupling coefficients between TM cylindrical waves have one more term

than their TE counter-parts because the electric fields of the TM cylindrical waves have a z-component while the TE cylindrical waves do not (see Eqs.(1.12)-(1.13)).

It is interesting to look at the inter-polarization coupling coefficients between TE and TM cylindrical waves. As shown by Eq.(2.5a), the inter-polarization coupling coefficients (with σ=TE, τ=TM or vice versa) are also the product of a cylindrical-wave factor and an overlap integral.

Note that $H_{-1}^{(2)}(\beta r) = -H_1^{(2)}(\beta r)$ and $H_{-1}^{(1)}(\beta r) = -H_1^{(1)}(\beta r)$ Then, for n=0, from Eq.(2.6a)-Eq.(2.7), we have

$$F_{\mu 0,\nu 0}^{(p,q)TE\,TM}(r) = F_{\mu 0,\nu 0}^{(p,q)TM\,TE}(r) = 0 \tag{2.9}$$

Putting Eq.(2.9) into Eq.(2.5a), we obtain

$$K_{\mu 0,\nu 0}^{(p,q)TE\,TM} = K_{\mu 0,\nu 0}^{(p,q)TM\,TE}(r) = 0 \tag{2.10}$$

Hence, for zeroth order (n=0) cylindrical waves, the inter-polarization coupling vanishes. This is because the zeroth order waves have circular symmetry and propagate along the radial direction. This is similar to the case of conventional grating structures, where TE modes do not couple with the TM modes if the direction of propagation is normal to the grating [67].

For higher order waves ($n \geq 1$), because they no longer travel radially, the coupling between TE-cylindrical waves and TM-cylindrical waves is generally nonzero. In fact, when the incident wave is not normal to the grating plane, the TE-polarization couples with the TM polarization and vice versa even for the case of linear gratings [84].

2.2.3 Large Radius Approximation for Cylindrical-Wave Factors

As we have seen in Eqs.(2.5)-(2.6), the complexity of the coupling coefficients comes from the cylindrical-wave factors. The coupled-wave equations could be simplified if a simpler expression for the cylindrical-wave factors can be found.

From the large argument approximation of the Hankel functions [81-82], we have

$$R_n^{(+)}(\beta r) = H_n^{(2)}(\beta r) = \sqrt{\frac{2}{\pi\beta r}}\, e^{-j(\beta r - \frac{\pi}{4} - \frac{\pi}{2} n)} \qquad (2.11a)$$

$$R_n^{(-)}(\beta r) = H_n^{(1)}(\beta r) = \sqrt{\frac{2}{\pi\beta r}}\, e^{j(\beta r - \frac{\pi}{4} - \frac{\pi}{2} n)} \qquad (2.11b)$$

$$(\beta r >> 1)$$

From Eq.(2.6a) and Eq.(2.11), the large radius approximation of the cylindrical-wave factors of the same polarization is obtained as

$$F_{\mu n,\nu n}^{(\pm,\pm)\sigma\sigma} = e^{\pm j(\beta_\mu^\sigma - \beta_\nu^\sigma) r} \qquad (\sigma=\text{TE or TM}) \qquad (2.12a)$$

$$F_{\mu n,\nu n}^{(+,-)\sigma\sigma} = j(-1)^n e^{j(\beta_\mu^\sigma + \beta_\nu^\sigma) r} \qquad (\sigma=\text{TE or TM}) \qquad (2.12b)$$

$$F_{\mu n,\nu n}^{(-,+)\sigma\sigma} = -j(-1)^n e^{-j(\beta_\mu^\sigma + \beta_\nu^\sigma) r} \qquad (\sigma=\text{TE or TM}) \qquad (2.12c)$$

and

$$\tilde{F}_{\mu n,\nu n}^{(\pm,\pm)\sigma\,\sigma} = e^{\pm j(\beta_\mu^\sigma + \beta_\nu^\sigma) r} \qquad (\sigma=\text{TM}) \qquad (2.13a)$$

$$\tilde{F}_{\mu n,\nu n}^{(+,-)\sigma\,\sigma} = -j(-1)^n e^{j(\beta_\mu^\sigma + \beta_\nu^\sigma) r} \qquad (\sigma=\text{TM}) \qquad (2.13b)$$

$$\tilde{F}_{\mu n,\nu n}^{(-,+)\sigma\,\sigma} = j(-1)^n e^{-j(\beta_\mu^\sigma + \beta_\nu^\sigma) r} \qquad (\sigma=\text{TM}) \qquad (2.13c)$$

For the case of TE-TM (TM-TE) coupling, assuming $\beta r >> 1$, it is not difficult to obtain from Eq.(2.6.), Eq.(2.7) and Eq.(2.11) the following results:

$$F_{\mu n,\nu n}^{(\pm,\pm)TETM}(r) = F_{\mu n,\nu n}^{(+,-)TETM}(r) = F_{\mu n,\nu n}^{(-,+)TETM}(r) = 0 \tag{2.14a}$$

$$F_{\mu n,\nu n}^{(\pm,\pm)TMTE}(r) = F_{\mu n,\nu n}^{(+,-)TMTE}(r) = F_{\mu n,\nu n}^{(-,+)TMTE}(r) = 0 \tag{2.14b}$$

2.2.4 Large Radius Approximation for Coupling Coefficients

Let σ=TE in Eqs.(12) and substitute the cylindrical-wave factors thus obtained into Eq.(2.5a), we obtain

$$K_{\mu n,\nu n}^{(\pm,\pm)TETE} = e^{\pm j(\beta_\mu^{TE} - \beta_\nu^{TE})r} K_{\mu\nu}^{TETE}(r) \tag{2.15a}$$

$$K_{\mu n,\nu n}^{(+,-)TETE} = j(-1)^n e^{j(\beta_\mu^{TE} + \beta_\nu^{TE})r} K_{\mu\nu}^{TETE}(r) \tag{2.15b}$$

$$K_{\mu n,\nu n}^{(-,+)TETE} = -j(-1)^n e^{-j(\beta_\nu^{TE} + \beta_\nu^{TE})r} K_{\mu\nu}^{TETE}(r) \tag{2.15c}$$

for TE-cylindrical waves.

Similarly, set σ=TM in Eqs.(2.12)-(2.13) and put the results into Eq.(2.5b), we get

$$K_{\mu n,\nu n}^{(\pm,\pm)TMTM}(r) = e^{\pm j(\beta_\mu^{TM} - \beta_\nu^{TM})r} [\tilde{K}_{\mu,\nu}^{TMTM}(r) + K_{\mu,\nu}^{TMTM}(r)] \tag{2.16a}$$

$$K_{\mu n,\nu n}^{(+,-)TMTM}(r) = -j(-1)^n e^{j(\beta_\mu^{TM} + \beta_\nu^{TM})r} [\tilde{K}_{\mu,\nu}^{TMTM}(r) - K_{\mu,\nu}^{TMTM}(r)] \tag{2.16b}$$

$$K_{\mu n,\nu n}^{(-,+)TMTM}(r) = j(-1)^n e^{-j(\beta_\mu^{TM} + \beta_\nu^{TM})r} [\tilde{K}_{\mu,\nu}^{TMTM}(r) - K_{\mu,\nu}^{TMTM}(r)] \tag{2.16c}$$

for TM-cylindrical waves.

For the case of TE-TM (TM-TE) coupling, substitution of Eqs.(2.14) into Eqs.(2.5)-(2.6) yields

$$K_{\mu n,\nu n}^{(\pm,\pm)TE\,TM}(r) = K_{\mu n,\nu n}^{(+,-)TE\,TM}(r) = K_{\mu n,\nu n}^{(-,+)TE\,TM}(r) = 0 \tag{2.17a}$$

$$K_{\mu n,\nu n}^{(\pm,\pm)TM\,TE}(r) = K_{\mu n,\nu n}^{(+,-)TM\,TE}(r) = K_{\mu n,\nu n}^{(-,+)TM\,TE}(r) = 0 \tag{2.17b}$$

Eqs.(2.17) are important result. It means that the inter-polarization coupling between higher order waves can be neglected for large radius ($\beta r >> 1$). This fact allows us to separate the TE-cylindrical waves from the TM-cylindrical waves. The validity of this approximation will be discussed in section 2.4

2.2.5 Large Radius Approximation of Coupled-Wave Equations

Since we can neglect the inter-polarization coupling under the large radius approximation ($\beta r >> 1$), by substituting the coupling coefficients from Eqs.(2.15), (2.16) and (2.17) into Eq.(2.4), we obtain

$$\frac{da_{\mu n}^{(+)TE}}{dr} = -j\sum_{\nu} K_{\mu\nu}^{TE\,TE}(r)\left[e^{j(\beta_\mu^{TE} - \beta_\nu^{TE})r} a_{\nu n}^{(+)TE} + j(-1)^n e^{j(\beta_\mu^{TE} + \beta_\nu^{TE})r} a_{\nu n}^{(-)TE}\right] \tag{2.18a}$$

$$\frac{da_{\nu n}^{(-)TE}}{dr} = j\sum_{\nu} K_{\mu\nu}^{TE\,TE}(r)\left[-j(-1)^n e^{-j(\beta_\mu^{TE} + \beta_\nu^{TE})r} a_{\nu n}^{(+)TE} + e^{-j(\beta_\mu^{TE} - \beta_\nu^{TE})r} a_{\nu n}^{(-)TE}\right] \tag{2.18b}$$

for TE cylindrical waves and

$$\frac{da_{\mu n}^{(+)TM}(r)}{dr} = -j\sum_{\nu}\{ e^{j(\beta_\mu^{TM} - \beta_\nu^{TM})r}\left[\tilde{K}_{\mu,\nu}^{TM\,TM}(r) + K_{\mu,\nu}^{TM\,TM}(r)\right] a_{\nu n}^{(+)TM}(r)$$

$$-j(-1)^n e^{j(\beta_\mu^{TM} + \beta_\nu^{TM})r}\left[\tilde{K}_{\mu,\nu}^{TM\,TM}(r) - K_{\mu,\nu}^{TM\,TM}(r)\right] a_{\nu n}^{(-)TM}(r) \tag{2.19a}$$

$$\frac{da_{\mu n}^{(-)TM}}{dr} = j\sum_{\nu}\{ j(-1)^n e^{-j(\beta_\mu^{TM} + \beta_\nu^{TM})r}\left[\tilde{K}_{\mu,\nu}^{TM\,TM}(r) - K_{\mu,\nu}^{TM\,TM}(r)\right] a_{\nu n}^{(+)TM}(r)$$

$$+ e^{-j(\beta_\mu^{TM} - \beta_\nu^{TM})r}\left[\tilde{K}_{\mu,\nu}^{TM\,TM}(r) + K_{\mu,\nu}^{TM\,TM}(r)\right] a_{\nu n}^{(-)TM}(r)\} \tag{2.19b}$$

for TM cylindrical waves.

Except for the factor of $\pm j(-1)^n$ in front of the cross-coupling terms, Eqs.(2.18)-(2.19) are essentially the same as the coupled-mode equations for conventional waveguides [67, 76, 83].

2.3 Single-Mode Planar Waveguides

Since single-mode planar waveguides are frequently used in practical devices, it is of interest to consider this special case. The subscripts " μ " and " ν " will be omitted in the following discussion because $\mu=\nu=0$.

2.3.1 Coupling Coefficients

From Eqs.(2.5), the coupling coefficients are expressed by

$$K_{n,n}^{(p,q)\sigma\tau} = F_{n,n}^{(p,q)\sigma\tau}(r)\, K^{\sigma\tau}(r) \qquad (\text{for } \sigma=\tau=\text{TE or } \sigma\neq\tau) \tag{2.20a}$$

$$= \tilde{F}_{n,n}^{(p,q)\sigma\tau}(r)\, \tilde{K}^{\sigma\tau}(r) + F_{n,n}^{(p,q)\sigma\tau}(r)\, K^{\sigma\tau}(r) \qquad (\text{for } \sigma=\tau=\text{TM}) \tag{2.20b}$$

with the K's being defined by

$$K^{\text{TE TE}}(r) = \frac{k_0^2}{2\beta^{\text{TE}}}\left[\int_{-\infty}^{\infty}\Delta\varepsilon(r,z)\left|Z^{\text{TE}}\right|^2 dz\right] / \left[\int_{-\infty}^{\infty}\left|Z^{\text{TE}}\right|^2 dz\right] \tag{2.21a}$$

$$\tilde{K}^{\text{TM TM}}(r) = \frac{\beta^{\text{TM}}}{2}\int_{-\infty}^{\infty}\Delta\varepsilon(r,z)\left|Z^{\text{TM}}\right|^2 dz \Big/ \int_{-\infty}^{\infty}\varepsilon\left|Z^{\text{TM}}\right|^2 dz \tag{2.21b}$$

$$K^{\text{TM TM}}(r) = \frac{1}{2\beta^{\text{TM}}}\int_{-\infty}^{\infty}\Delta\varepsilon(r,z)\left|\frac{dZ^{\text{TM}}}{dz}\right|^2 dz \Big/ \int_{-\infty}^{\infty}\varepsilon\left|Z^{\text{TM}}\right|^2 dz \tag{2.21c}$$

$$K^{TE\,TM}(r) = \frac{k_0}{2\sqrt{\beta^{TE}\,\beta^{TM}}} \frac{\int_{-\infty}^{\infty} \Delta\varepsilon\, Z^{TE*} \left(\frac{dZ^{TM}}{dz}\right) dz}{\sqrt{\int_{-\infty}^{\infty} \left|Z^{TE}\right|^2 dz \int_{-\infty}^{\infty} \varepsilon \left|Z^{TM}\right|^2 dz}} \tag{2.21d}$$

$$K^{TM\,TE}(r) = \frac{k_0}{2\sqrt{\beta^{TM}\,\beta^{TE}}} \frac{\int_{-\infty}^{\infty} \Delta\varepsilon \frac{dZ^{TM*}}{dz} Z^{TE} dz}{\sqrt{\int_{-\infty}^{\infty} \varepsilon \left|Z^{TM}\right|^2 dz \int_{-\infty}^{\infty} \left|Z^{TE}\right|^2 dz}} \tag{2.21f}$$

The cylindrical-wave factors are obtained from Eq.(2.6) as

$$F_{n,n}^{(p,q)\sigma\tau}(r) = \frac{\pi r}{4}\sqrt{\beta^{\sigma}\,\beta^{\tau}}\,[\,R_{n-1}^{(p)*}(\beta^{\sigma} r)\,R_{n-1}^{(q)}(\beta^{\tau} r) \pm R_{n+1}^{(p)*}(\beta^{\sigma} r)\,R_{n+1}^{(q)}(\beta^{\tau} r)\,]$$

$$(+ \text{ sign for } \sigma=\tau\ ;\ - \text{ sign for } \sigma\neq\tau\ ) \tag{2.22a}$$

$$\tilde{F}_{n,n}^{(p,q)\sigma\tau}(r) = \frac{\pi r}{2}\sqrt{\beta^{\sigma}\,\beta^{\tau}}\,R_{n}^{(p)*}(\beta^{\sigma} r)\,R_{n}^{(q)}(\beta^{\tau} r) \qquad (\sigma=\tau=TM) \tag{2.22b}$$

2.3.2 Large Radius Approximation For Coupling Coefficients

For single-mode waveguide ($\mu=\nu=0$), we have $\beta_\mu=\beta_\nu=\beta$. Under the large radius approximation, from Eqs.(2.15)-(2.16), we get

$$K_{n,n}^{(+,+)TE\,TE} = K_{n,n}^{(-,-)TE\,TE} = K^{TE\,TE}(r) \tag{2.23a}$$

$$K_{n,n}^{(+,-)TE\,TE} = j\,(-1)^n\, e^{j2\beta^{TE} r}\, K^{TE\,TE}(r) \tag{2.23b}$$

$$K_{n,n}^{(-,+)TE\,TE} = -j\,(-1)^n\, e^{-j2\beta^{TE} r}\, K^{TE\,TE}(r) \tag{2.23c}$$

for the case of TE cylindrical waves and

$$K_{n,n}^{(\pm,\pm)TM\,TM}(r) = [\tilde{K}^{TM\,TM}(r) + K^{TM\,TM}(r)] \tag{2.24a}$$

$$K_{n,n}^{(+,-)TM\,TM}(r) = -j\,(-1)^n e^{j2\beta^{TM} r}\,[\tilde{K}^{TM\,TM}(r) + K^{TM\,TM}(r)] \tag{2.24b}$$

$$K_{n,n}^{(-,+)TM\,TM}(r) = j\,(-1)^n e^{-j2\beta^{TM} r}\,[\tilde{K}^{TM\,TM}(r) + K^{TM\,TM}(r)] \tag{2.24c}$$

for the case of TM cylindrical waves.

As already shown in the previous section, the inter-polarization coupling approaches zero at large radius. It is not necessary to write down the coupling coefficients for this case.

The coupled-wave equations then become

$$\frac{da_n^+}{dr} = -j\,K(r)\,[\,a_n^+(r) + j\,(-1)^n\, e^{j2\beta r}\, a_n^-(r)\,] \tag{2.25a}$$

$$\frac{da_n^-}{dr} = j\,K(r)\,[\,-j\,(-1)^n\, e^{-j2\beta r} a_n^+(r) + a_n^-(r)\,] \tag{2.25b}$$

for TE cylindrical waves and

$$\frac{da_n^+}{dr} = -j\{[K(r)+\tilde{K}(r)]a_n^+(r) - j\,(-1)^n\, e^{j2\beta r}\,[K(r)-\tilde{K}(r)]a_n^-(r)\,\} \tag{2.26a}$$

$$\frac{da_n^-}{dr} = j\{j\,(-1)^n\, e^{-j2\beta r}\,[K(r)-\tilde{K}(r)]\, a_n^+(r) + [K(r)+\tilde{K}(r)]a_n^-(r)\} \tag{2.26b}$$

for TM cylindrical waves.

For simplicity, we have omitted the superscripts " TE " and " TM " in Eqs.(2.25)-(2.26).

2.3.3 Numerical Values of Cylindrical-Wave Factors

Making use of Eq.(2.7), the cylindrical-wave factors can be expressed explicitly as

$$F_{n,n}^{(+,+)\sigma\sigma}(r) = F_{n,n}^{(-,-)\sigma\sigma^*}(r) = \frac{\pi\beta^{\sigma} r}{4}\left[\left|H_{n-1}^{(1)}(\beta^{\sigma} r)\right|^2 + \left|H_{n+1}^{(1)}(\beta^{\sigma} r)\right|^2\right]$$

(σ=TE or TM) (2.27a)

$$F_{n,n}^{(+,-)\sigma\sigma}(r) = F_{n,n}^{(-,+)\sigma\sigma^*}(r) = \frac{\pi\beta^{\sigma} r}{4}\{[H_{n-1}^{(1)}(\beta^{\sigma} r)]^2 + [H_{n+1}^{(1)}(\beta^{\sigma} r)]^2\}$$

(σ=TE or TM) (2.27b)

$$\tilde{F}_{n,n}^{(+,+)\sigma\sigma}(r) = \tilde{F}_{n,n}^{(-,-)\sigma\sigma^*}(r) = \frac{\pi\beta^{\sigma} r}{2}\left|H_n^{(2)}(\beta^{\sigma} r)\right|^2$$

(σ=TM) (2.27c)

$$\tilde{F}_{n,n}^{(+,-)\sigma\sigma}(r) = \tilde{F}_{n,n}^{(-,+)\sigma\sigma^*}(r) = \frac{\pi\beta^{\sigma} r}{2}[H_n^{(1)}(\beta^{\sigma} r)]^2$$

(σ=TM) (2.27d)

$$F_{n,n}^{(+,+)\sigma\tau}(r) = F_{n,n}^{(-,-)\sigma\tau^*}(r) = \frac{\pi r}{4}\sqrt{\beta^{\sigma}\beta^{\tau}}\,[H_{n-1}^{(2)*}(\beta^{\sigma} r) H_{n-1}^{(2)}(\beta^{\tau} r) - H_{n+1}^{(2)*}(\beta^{\sigma} r) R_{n+1}^{(2)}(\beta^{\tau} r)]$$

($\sigma\neq\tau$; σ and τ =TE, TM) (2.27e)

$$F_{n,n}^{(+,-)\sigma\tau}(r) = F_{n,n}^{(-,+)\sigma\tau^*}(r) = \frac{\pi r}{4}\sqrt{\beta^{\sigma}\beta^{\tau}}\,[H_{n-1}^{(2)*}(\beta^{\sigma} r) H_{n-1}^{(1)}(\beta^{\tau} r) - H_{n+1}^{(2)*}(\beta^{\sigma} r) H_{n+1}^{(1)}(\beta^{\tau} r)]$$

($\sigma\neq\tau$; σ and τ =TE, TM) (2.27f)

Note that Eq.(2.27a) and Eq.(2.27c) are real. The amplitude of the cylindrical-wave factor in Eq.(2.27a) is different from that of Eq.(2.27b). Similar remarks can be said about Eq.(2.27e) and Eq.(2.27f). But Eq.(2.27c) and Eq.(2.27d) yield the same amplitude.

In Fig.5(a)-(e), we have plotted the amplitudes of the cylindrical-wave factors in Eqs.(2.27a)-(2.27b) for n=0, 1, 2, 10 and 15 against the normalized radius βr. The amplitudes of the cylindrical-wave factors asymptotically go to 1 as βr becomes large.

Similar results are shown in Fig.6(a)-(b) for Eqs.(2.27c)-(2.27d).

In Fig.7(a)-(d), the amplitudes of the cylindrical-wave factors for TE-TM (TM-TE) couplings are presented for the case of $(n^{TE}-n^{TM})/n^{TE}=10^{-3}$, where n^{TE} and n^{TM} are the effective index of the TE- and the TM slab modes, respectively. We see that the cylindrical-wave factor for TE-TM (TM-TE) coupling approaches zero as βr becomes very large. This tendency agrees with the large radius approximation presented above. Fig.7(a)-(d) show that the coupling between contra-directional TE and TM cylindrical waves (Eq.(2.27f)) is stronger than the case for co-directional propagation (Eq.(2.27f)).

It is observed that, in general, the amplitudes of the cylindrical-wave factors increase very rapidly as βr goes to 0. This is true even for TE-TM (TM-TE) coupling. This behavior is due to the singularity of Hankel functions at the origin [81-82]. We can properly choose the boundary condition such that the total field remains finite at r=0. This can be realized by setting $a_n^{(+)\sigma}(0) = a_n^{(-)\sigma}(0)$.

2.4. Discussions

2.4.1. Validity of Large Radius Approximation

As seen in the previous section, the large radius approximation yields simplified coupled-wave equations for cylindrical waves. But when can one safely apply this approximation ? As we have already seen in Fig.5-7, the range of validity of the large radius approximation depends on the order of the cylindrical waves. The higher the order, the larger the radius should be. The large radius condition for TE-TE and TM-TM couplings can be obtained as (see Appendix V)

$$r \geq r_0 = \frac{\sqrt{5(3n^2+1)}}{\beta} \qquad (2.28a)$$

and for TE-TM couplings as

$$r \geq r_0 = \frac{20\,n}{\beta} \qquad (2.28b)$$

where n is the order of the cylindrical wave and r_0 is the lower bound of the radius above which the large radius approximation is reasonably good as shown in Tables 2.1-2.3.

Tables 2.1-2.4 list the exact values of the amplitudes of the cylindrical wave factors calculated from Eqs.(2.27) for different wave order n at the normalized radius βr_0 given by Eq.(2.28). As can be seen from the tables, Eq.(2.28a) is a good criteria for TE-TE and TM-TM couplings while Eq.(2.28b) gives a reasonable guideline for TE-TM couplings. However, Eq.(28.a) is not suitable for TE-TM couplings as shown in Table 2.4.

For InGaAsP/InP material, we have $\beta \approx 16\ \mu m^{-1}$ at $\lambda = 1.3\mu m$. In Tables 2.2-2.4, the value of r_0 is also calculated for various n. For example, the r_0 obtained from Eq.(2.28a) is $r_0 = 0.14\ \mu m$ for n=0; $r_0 = 0.28\ \mu m$ for n=1 and $r_0 = 0.50\ \mu m$ for n=2. The smallest radius achievable by E-beam or focused ion beam (FIB) is 0.5 μm. These numerical values indicate that in practical devices, the large radius approximation generally applies, especially for lower order cylindrical waves.

2.4.2. Comparison with Other Results

It is not difficult to verify that for n=0, the cylindrical-wave factors defined in Eq.(2.6) and Eq.(2.27) are the same as the special case treated by Zheng and Lacroix [65-66].

On the other hand, the scalar-wave formulation for TE-cylindrical waves of Erdogan and Hall [63] gives different cylindrical-wave factors, thus different coupling coefficients. In their coupled-wave equations (see Eq.(26) in [63]), Hankel functions of order n appear, while as shown here in Eq.(2.6) and Eq.(2.27), the Hankel functions are of the order of n±1. The difference in the cylindrical-wave factors affect also the results of large radius approximation as we can see from Eq.(28) in [63] and Eq.(2.25) in this work. The signs of the factors $j(-1)^n$ are different in these two equations.

The difference between our results and those of Erdogan and Hall arises from the different approaches used to derive the coupled-wave equations. In [63], Erdogan and Hall first used the Green's function method to obtain a formal solution to the scalar-wave equation, and then by expressing the Green's function in Fourier series, they got their coupled-wave equations by differentiation. In contrast, we started with Maxwell's vector-wave equations in Chapter 1. We first defined the TE- and TM-cylindrical waves in an ideal uniform planar waveguide and proved the orthogonality of these waves. Then, we expanded the actual field in a circular grating planar waveguide in terms of the cylindrical

waves of the ideal uniform waveguide.

The coupling coefficients in [63] are defined by the overlap integrals of the scalar field (i.e., the non-zero component of the magnetic field) of the cylindrical waves with the grating. The scalar field of a cylindrical wave in a uniform planar waveguide is proportional to the Hankel functions of order n. This explains why the cylindrical-wave factors and the coupling coefficients in [63] are expressed by $H_n^{(1)}$ and $H_n^{(2)}$.

As given by Eq.(2.2) in this paper and Eq.(1.32) in Chapter 1, our coupling coefficients are calculated from the overlap integral of the electric field of the cylindrical waves with the grating. This is analogous to the well-established coupled-mode formulations for conventional waveguides by Kogelnik [67], Marcuse [76] and others [83]. The electric field of TE-cylindrical waves has one r-component which is proportional to $(n/r)H_n^{(1)}$ (or $(n/r)H_n^{(2)}$) and one θ-component which is proportional to $dH_n^{(1)}/dr$ (or $dH_n^{(2)}/dr$) . Because $(n/r)H_n^{(1)}$ and $dH_n^{(1)}/dr$ are related to the Hankel functions of order $(n\pm1)$ (see Eq.(A4.7) in Appendix IV and recurrence formulae in [81-82]), our cylindrical-wave factors and coupling coefficients are described by the Hankel functions of order $(n\pm1)$.

Even though Hall [85] applied the Green's function method to one-dimensional waveguide and derived successfully the same coupled-mode equations for two-mode coupling as given by others [67, 76, 80, 83], the applicability of the same approach to the problem of circular grating is dubious. In the case of one-dimensional waveguides, the propagation of a mode is described by the exponential function $\exp(\pm j\beta z)$. The exponential function has a very special property in that its derivatives are proportional to itself. This makes the electric field proportional to the magnetic field [67, 76]. Then, it does not matter whether the electric field or the magnetic field is used to calculate the overlap integral.

In the case of circular gratings, the propagation of cylindrical waves are described by the Hankel functions. Because the derivative of a Hankel function of order n is not proportional to itself, the electric field of a cylindrical wave then no longer relates linearly to its magnetic field. Thus, the overlap integral calculated by the electric field is not the same as that obtained by the magnetic field (or say the scalar field).

Since the approach used in Chapter 1 is a vector-wave formulation and in principle similar to the conventional coupled-mode theories [67, 76, 83]. it is believed that the coupled-wave equations derived in Chapter 1 and discussed here are more appropriate to the problem of circular grating devices.

2.5. Summary

A simplified form of the coupled-wave equations was derived for cylindrical waves in circular grating distributed feedback planar waveguides. Under the large radius approximation ($\beta r >> 1$), the coupling between TE and TM cylindrical waves can be neglected. This renders the coupled-wave equations separable into two sets, one for TE cylindrical waves and the other for TM cylindrical waves. The large radius approximation is valid for most practical cases. The difference between our theory and the scalar theory of Erdogan and Hall [63] is clarified. In the next Chapter, the simplified coupled-wave equations will be used to analyze circular grating DFB/DBR lasers.

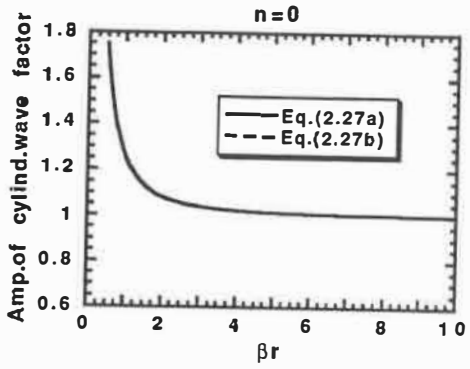

(a)

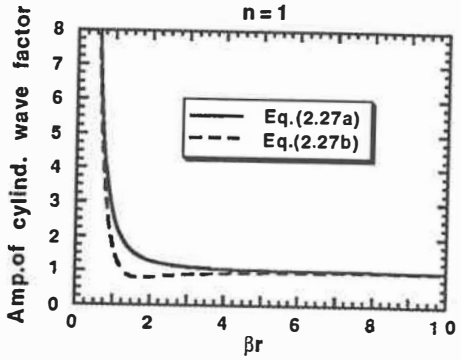

(b)

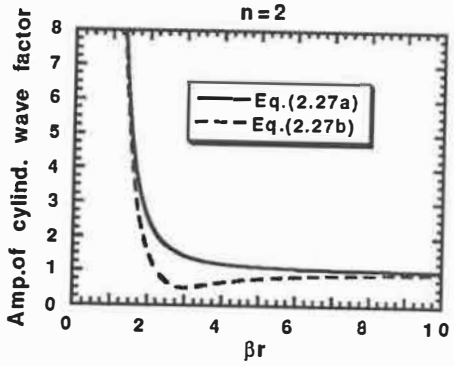

(c)

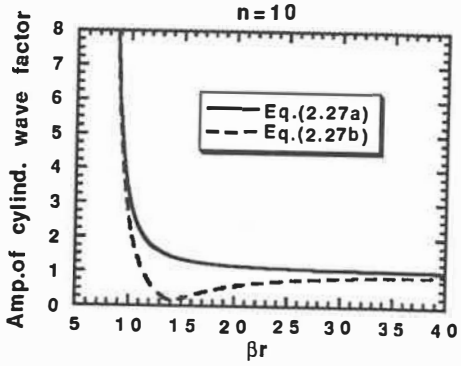

(d)

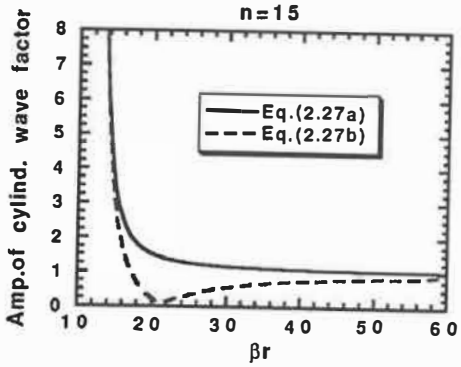

(e)

Fig.5 Amplitudes of cylindrical wave factors in Eq.(2.27a)-(2.27b) versus βr for : (a) n=0 ; (b) n=1 ; (c) n=2 ; (d) n=10 and (e) n=15.

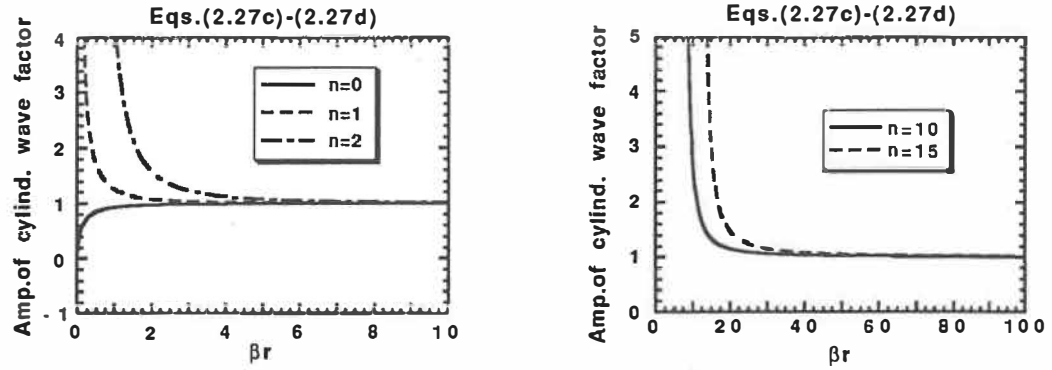

(a) (b)

Fig.6 Amplitudes of cylindrical wave factors in Eq.(2.27c)-(2.27d) versus βr for : (a) n=0, 1 and 2 ; (b) n=10 and 15.

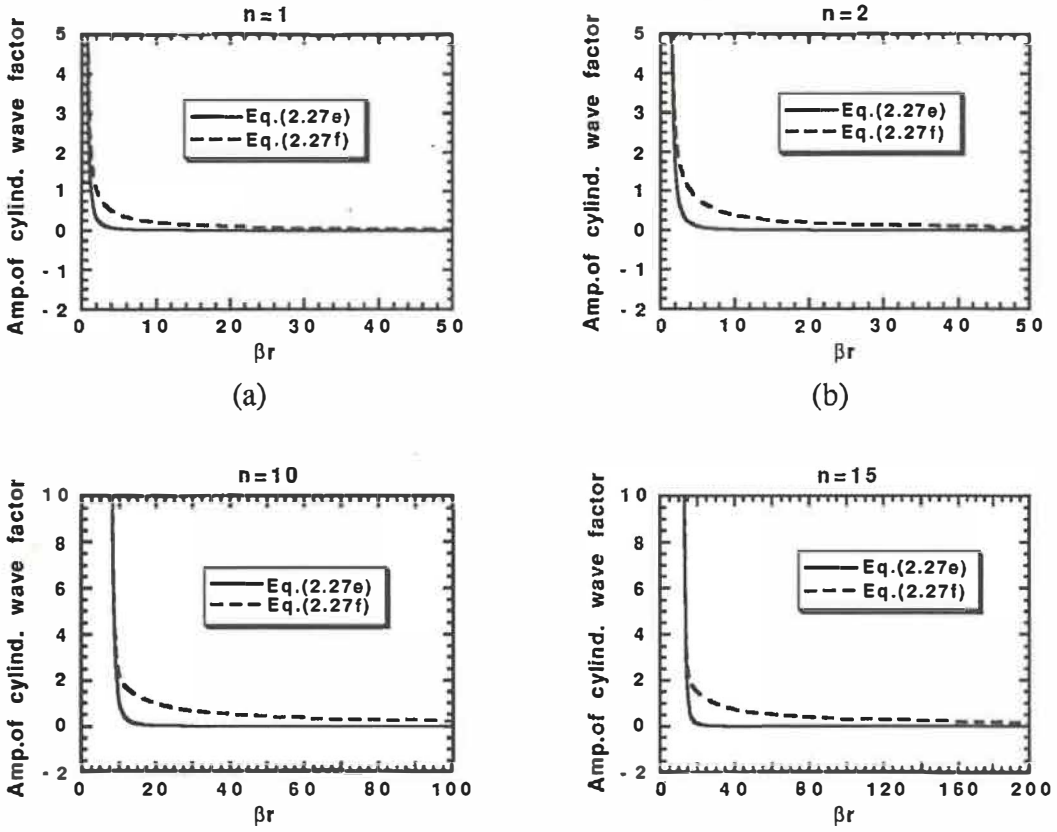

(a) (b)

(c) (d)

Fig.7 Amplitudes of cylindrical wave factors in Eqs.(2.27e)-(2.27f) versus βr for : (a) n=1; (b) n=2 ; (c) n=10 and (d) n=15 .

Table 2.1 Amplitude of Cylindrical-Wave Factors in Eq.(2.27a)-(2.27b)

$$\beta r_0 = \sqrt{5(3n^2+1)}$$

order n	βr_0	Eq.(2.27a)			Eq.(2.27b)		
		Exact	Large Radius Approx.	Relativ Error (%)	Exact	Large Radius Approx.	Relativ Error (%)
0	2.236	1.06618	1.0	6.6	1.06618	1.0	6.6
1	4.472	1.04682	1.0	4.7	0.94648	1.0	-5.4
2	8.062	1.03921	1.0	3.9	0.91313	1.0	-8.7
10	38.794	1.03529	1.0	3.5	0.89780	1.0	-10.2
15	58.138	1.03518	1.0	3.5	0.89740	1.0	-10.3
40	154.935	1.03511	1.0	3.5	0.89713	1.0	-10.3
100	387.304	1.03510	1.0	3.5	0.89709	1.0	-10.3

Table 2.2 Amplitude of Cylindrical-Wave Factors in Eq.(2.27c)-(2.27d)

$$\beta r_0 = \sqrt{5(3n^2+1)}$$

order n	βr_0	r_0 for $\beta = 16$ (μm)	Exact	Large Radius Approx.	Relative Error (%)
0	2.236	0.140	0.97990	1.0	-2.0
1	4.472	0.280	1.01801	1.0	1.8
2	8.062	0.504	1.02942	1.0	2.9
10	38.794	2.425	1.03484	1.0	3.5
15	58.138	3.634	1.03498	1.0	3.5
40	154.935	9.683	1.03508	1.0	3.5
100	387.304	24.207	1.03510	1.0	3.5

Table 2.3 Amplitude of Cylindrical-Wave Factors in Eq.(2.27e)-(2.27f)

$$\beta r_0 = 20\,n$$

order n	βr_0	r_0 for $\beta = 16$ (μm)	Eq.(2.27e) exact	Eq.(2.27f) exact	Large Radius Approx.
0	0.0	0.0	0.0	0.0	0.0
1	20	1.25	0.00251	0.10008	0.0
2	40	2.50	0.00126	0.10006	0.0
10	200	12.50	0.00026	0.10005	0.0
15	300	18.75	0.00017	0.10005	0.0
40	800	50	0.00008	0.10005	0.0
100	2000	125	0.00006	0.10005	0.0

Table 2.4 Amplitude of Cylindrical-Wave Factors in Eq.(2.27e)-(2.27f)

$$\beta r_0 = \sqrt{5(3n^2+1)}$$

order n	βr_0	r_0 for $\beta = 16$ (μm)	Eq.(2.27e) exact	Eq.(2.27f) exact	Large Radius Approx.
0	0.0	0.0	0.0	0.0	0.0
1	4.472	0.280	0.05270	0.45054	0.0
2	8.062	0.504	0.03356	0.49754	0.0
10	38.794	2.425	0.00736	0.51560	0.0
15	58.138	3.634	0.00492	0.51604	0.0
40	154.935	9.683	0.00185	0.51635	0.0
100	387.304	24.207	0.00074	0.51639	0.0

CHAPTER 3

ANALYSIS OF CIRCULAR GRATING LASERS

3.1 Introduction

Circular grating distributed feedback (CG-DFB) and distributed Bragg reflector (CG-DBR) lasers offer the possibility of emitting a circularly-symmetric, low-divergence output beam from the surface. A two-dimensional array of these devices may also be conceived for high power applications.

In this chapter, the threshold behavior of CG-DFB and CG-DBR lasers is analyzed by using the coupled-wave equations developed in the previous chapters. A threshold current analysis of these lasers is also provided. For simplicity, the circular grating is assumed to be a first-order grating and hence the coupling to radiation field necessary for surface emission is neglected. Although the circular grating usually couples TE-and TM-cylindrical waves, the inter-polarization coupling becomes very small under the large radius approximation as pointed out in Chapter 2. Therefore, the discussion in this Chapter is limited to TE-cylindrical waves. The effect of coupling between TE- and TM-cylindrical waves is left for future investigation.

The outline of this Chapter is as follows: first, the structures of CG-DFB and CG-DBR lasers are described in Section 3.2. Then, in Section 3.3, the coupled-wave equations for TE-cylindrical waves is briefly reviewed. In Section 3.4, the analytical solution is obtained for the coupled-wave equations under the large radius approximation. The threshold gain analysis of CG-DFB and CG-DBR lasers is presented in Section 3.5. The mode properties of CG-DFB/DBR lasers are discussed. It is found that by a proper choice of the total phase-shift, the even order waves can have a lower threshold gain and a lower threshold current than the odd order waves. This mode selectivity between the even and the odd cylindrical waves is important in practical design of CG-DFB and CG-DBR lasers.

3.2. Structure of Circular Grating Lasers

The structure of a CG-DFB and a CG-DBR laser is shown schematically in Fig.8(a) and Fig.8(b), respectively. Fig.9(a) shows the cross-section of a CG-DFB laser and Fig.9(b) that of a CG-DBR laser. In both figures, the shaded region represents the active material. For CG-DFB lasers, the active medium extends into the grating region. For CG-DBR lasers, the active layer is limited within a circle of radius R_1.

In order to obtain the eigenvalue equation valid for both the CG-DFB and the CG-DBR lasers, we consider the laser structure shown in Fig.10. Without loss of generality, the circular grating is assumed to be an etched grating and have a rectangular profile. The grating period is denoted by Λ. The spacing between the grating lines is represented by W_1 and the width of the grating line is denoted by W_2.

For $0 < r < R_1$, the permittivity of the structure is described by:

$$\begin{aligned}
\tilde{\varepsilon}(z,r) &= \varepsilon_s \quad , \quad z < d_1 = 0 \\
&= \varepsilon' + j\varepsilon'' \quad , \quad d_1 < z < d_2 \\
&= \varepsilon_b \quad , \quad d_2 < z < d_4 \\
&= \varepsilon_c \quad , \quad d_4 < z < \infty
\end{aligned} \tag{3.1a}$$

and for $R_1 < r < \infty$ by

$$\begin{aligned}
\tilde{\varepsilon}(z,r) &= \varepsilon_s \quad , \quad z < d_1 = 0 \\
&= \varepsilon'_f + j\varepsilon''_f \quad , \quad d_1 < z < d_2 \\
&= \varepsilon_{cl} \quad , \quad d_2 < z < d_3 \\
&= \varepsilon_g(z,r) \quad , \quad d_3 < z < d_4 \\
&= \varepsilon_c \quad , \quad d_4 < z < \infty
\end{aligned} \tag{3.1b}$$

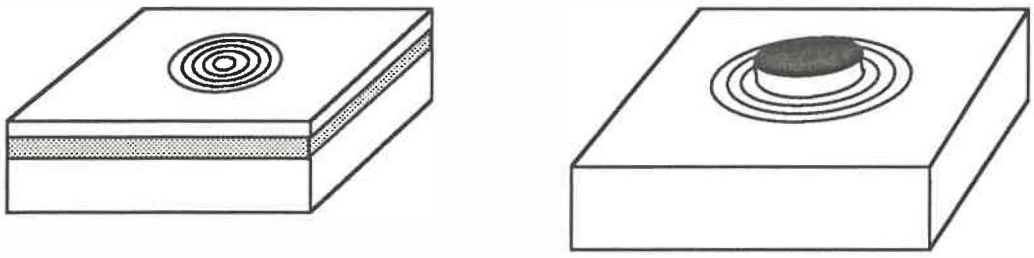

(a) (b)

Fig.8 Diagram of circular grating (CG) lasers: (a) CG-DFB laser; (b) CG-DBR laser.

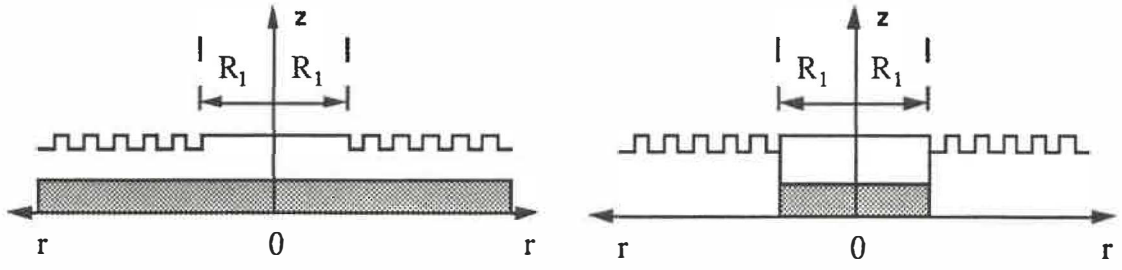

(a) (b)

Fig.9 Cross-section of circular grating (CG) lasers: (a) CG-DFB laser; (a) CG-DBR laser.

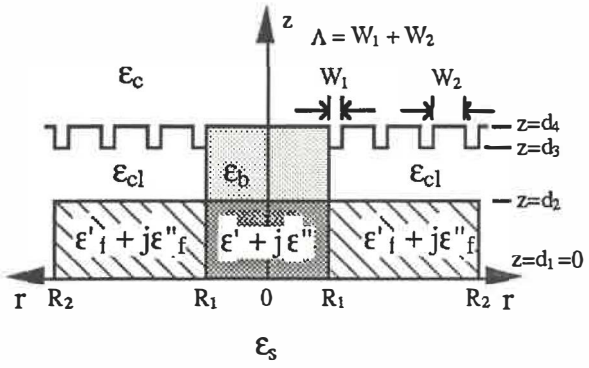

Fig.10 Cross-section and permittivity of circular grating lasers.

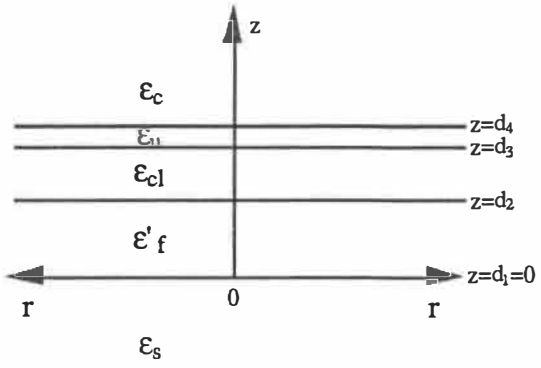

Fig.11 Structure and permittivity of the unperturbed planar waveguide.

In.Eqs.(3.3.1a)-(3.1b), ε_s is the permittivity of the substrate region, ε_c the permittivity of the cover region (normally air ε_c=1), ε_b the permittivity of the cladding for $0 < r < R_1$, ε_{cl} the permittivity of the cladding for $R_1 < r < \infty$. The permittivity of the active layer in the center region ($0 < r < R_1$) is denoted by ε (with the real part ε' and the imaginary part ε''). ε_f is the permittivity in the grating region for $d_1 < z < d_2$ and $R_1 < r < \infty$. For CG-DFB lasers, we have $\varepsilon_f = \varepsilon = \varepsilon' + j\varepsilon''$ and $\varepsilon_b = \varepsilon_{cl}$; for CG-DBR lasers, $\varepsilon_f = \varepsilon_f'$ and $\varepsilon_f''=0$. ε_g is the permittivity of the grating layer described by

$$\varepsilon_g(z,r) = \sum_{m=0}^{\infty} \{\varepsilon_c [u(r - R_1 - m\Lambda) - u(r - R_1 - w_1 - m\Lambda)]$$

$$+ \varepsilon_{cl} [u(r - R_1 - w_1 - m\Lambda) - u(r - R_1 - (m+1)\Lambda)]\}$$

$$(m = 0, 1, 2, 3, \ldots) \qquad (3.1c)$$

$$u(r) = 1, \quad r > 0$$
$$= 0, \quad r < 0 \qquad (3.1d)$$

As $\varepsilon_g(z,r)$ is periodic for $r > R_1$, we can expand it in terms of its Fourier series:

$$\varepsilon_g(z,r) = \sum_{m=-\infty}^{\infty} \varepsilon_{gm}(z)\, e^{j\frac{2\pi}{\Lambda} m (r - R_1)} \tag{3.2a}$$

with

$$\varepsilon_{gm}(z) = \frac{1}{\Lambda}\int_0^{\Lambda} \varepsilon_g(z, r'+R_1)\, e^{-j\frac{2\pi}{\Lambda} m r'}\, dr' \tag{3.2b}$$

For $m = 0$, we have

$$\varepsilon_{g0}(z) = \frac{1}{\Lambda}\int_0^{\Lambda} \varepsilon_g(z, r'+R_1)\, dr'$$

$$= \frac{1}{\Lambda}[\, \varepsilon_c W_1 + \varepsilon_{cl} W_2 \,]$$

$$= \varepsilon_{cl} - (\, \varepsilon_{cl} - \varepsilon_c \,)\frac{W_1}{\Lambda}\,] \tag{3.3a}$$

For $m \neq 0$,

$$\varepsilon_{gm}(z) = \frac{1}{\Lambda}\int_0^{\Lambda} \varepsilon_g(z, r'+R_1)\, e^{-j\frac{2\pi}{\Lambda} m r'}\, dr'$$

$$= \frac{1}{\Lambda}[\, \varepsilon_c \int_0^{W_1} e^{-j\frac{2\pi}{\Lambda} m r'}\, dr' + \varepsilon_{cl}\int_{W_1}^{\Lambda} e^{-j\frac{2\pi}{\Lambda} m r'}\, dr']$$

$$= -\frac{(\varepsilon_{cl} - \varepsilon_c)}{\pi m} e^{-j\frac{\pi}{\Lambda} m W_1}\, \sin(\pi m \frac{W_1}{\Lambda}) \tag{3.3b}$$

3.3 Coupled-Wave Equations For TE-Cylindrical Waves

To analyze CG-DFB and DBR lasers, we resort to the coupled-wave equations for cylindrical waves developed in Chapter 1. Even though TE-cylindrical waves are coupled with TM-cylindrical waves (except for the zeroth order cylindrical waves), the inter-polarization coupling is negligible when the radius becomes large (see Chapter 2). In the following analysis, we will consider only TE-cylindrical waves and neglect the coupling between TE- and TM-cylindrical waves.

Assuming that the circular grating is fabricated on a single-mode planar waveguide, the coupled-wave equations for TE-cylindrical waves are (see Chapter 2):

$$\frac{da_n^{(+)}}{dr} = -j\,K(r)\,[\,F_{n,n}^{(+,+)}(r)\,a_n^{(+)}(r) + F_{n,n}^{(+,-)}(r)\,a_n^{(-)}(r)\,] \tag{3.4a}$$

$$\frac{da_n^{(-)}}{dr} = j\,K(r)\,[\,F_{n,n}^{(-,+)}(r)\,a_n^{(+)}(r) + F_{n,n}^{(-,-)}(r)\,a_n^{(-)}(r)\,] \tag{3.4b}$$

where the a's are the amplitudes of the TE-cylindrical waves (with the superscript "+" denoting the outward-propagating waves and the superscript "-" the inward-propagating waves, respectively.). The subscript " n " is an integer and denotes the order of the cylindrical wave. The F's are the cylindrical-wave factors defined by

$$F_{n,n}^{(+,+)}(r) = F_{n,n}^{(-,-)*}(r) = \frac{\pi\beta r}{4}\,[\,\left|H_{n-1}^{(1)}(\beta r)\right|^2 + \left|H_{n+1}^{(1)}(\beta r)\right|^2\,] \tag{3.5a}$$

$$F_{n,n}^{(+,-)}(r) = F_{n,n}^{(-,+)*}(r) = \frac{\pi\beta r}{4}\,\{[\,H_{n-1}^{(1)}(\beta r)\,]^2 + [\,H_{n+1}^{(1)}(\beta r)\,]^2\,\} \tag{3.5b}$$

with β being the propagation constant of the fundamental TE slab-mode in the unperturbed planar waveguide and the H's denoting the Hankel functions.

K(r) in Eq.(3.4) is the coupling coefficient given by

$$K(r) = \frac{k_0^2}{2\beta}\left[\int_{-\infty}^{\infty} \Delta\varepsilon(r,z)\,|Z|^2 dz\right] / \left[\int_{-\infty}^{\infty} |Z|^2 dz\right] \tag{3.6}$$

in which k_0 is the wave number of light in the vacuum, $\Delta\varepsilon(r,z)$ is the permittivity perturbation due to the circular grating (see Eq.(3.12) below.). Z is the field distribution in the z direction of the fundamental TE slab-mode which satisfies the following scalar wave equation:

$$\frac{d^2Z}{dz^2} + [\, k_0^2 \bar{\varepsilon} - \beta^2 \,]\, Z = 0 \tag{3.7}$$

with $\bar{\varepsilon}$ as the permittivity of the unperturbed planar waveguide (see Fig.11 and Section 3.4).

As shown in Chapter 2, when βr satisfies the large radius condition :

$$\beta r \geq \beta r_0 = \sqrt{5(3n^2+1)} \tag{3.8}$$

we have

$$F_{n,n}^{(\pm,\pm)}(r) = 1 \tag{3.9a}$$

$$F_{n,n}^{(+,-)}(r) = F_{n,n}^{(+,-)*}(r) = j\,(-1)^n e^{j2\beta r} \tag{3.9b}$$

Then, the coupled-wave equations become :

$$\frac{da_n^{(+)}}{dr} = -j\,K(r)\,[\, a_n^{(+)}(r) + j\,(-1)^n\ e^{j2\beta r}\, a_n^{(-)}(r)\,] \tag{3.10a}$$

$$\frac{da_n^{(-)}}{dr} = j\,K(r)\,[\, -j\,(-1)^n\ e^{-j2\beta r} a_n^{(+)}(r) + a_n^{(-)}(r)\,] \tag{3.10b}$$

3.4 Solution of Coupled-Wave Equations

3.3.1 Coupling Coefficient

To analyze CG-DFB and DBR lasers we have to find the coupling coefficient K(r). As shown in Eq.(3.6), K(r) is determined by the perturbation $\Delta\varepsilon(r,z)$ and the field distribution of the fundamental slab-mode in the unperturbed waveguide.

Following Handa, et. al, [86], we choose the unperturbed waveguide as a lossless planar waveguide whose permittivity is:

$$\begin{aligned}
\bar{\varepsilon}(z) &= \varepsilon_s \ , \quad z < d_1 = 0 \\
&= \varepsilon'_f \ , \quad d_1 < z < d_2 \\
&= \varepsilon_{cl} \ , \quad d_2 < z < d_3 \\
&= \varepsilon_u = \varepsilon_{cl} - (\varepsilon_{cl} - \varepsilon_c)\left(\frac{w_1}{\Lambda}\right), \quad d_3 < z < d_4 \\
&= \varepsilon_c \ , \quad z > d_4
\end{aligned} \tag{3.11}$$

This is illustrated in Fig.11. The perturbation is then calculated from

$$\Delta\varepsilon(z,r) = \tilde{\varepsilon}(z,r) - \bar{\varepsilon}(z) \tag{3.12}$$

From Eq.(3.1), Eq.(3.2) Eq.(3.6) and Eq.(3.12), the coupling coefficient K(r) can be obtained as :

$$K(r) = \Delta + j\,\alpha_1 \qquad (\text{for } 0 < r < R_1) \tag{3.13a}$$

and

$$K(r) = j\alpha_2 - \sum_{m=-\infty}^{\infty}{}' K_m e^{-j\Omega_m} e^{j\frac{2\pi}{\Lambda} m r} \qquad (\text{for } R_1 < r < \infty) \qquad (3.13b)$$

The prime " ' " in the summation symbol means $m \neq 0$.

In Eqs.(3.13a)-(13b), we have

$$\Delta = (k_0^2 / 2\beta)\ \{(\varepsilon' - \varepsilon'_f)\,\Gamma_2 + (\varepsilon_b - \varepsilon_{cl})\,\Gamma_3 + (\varepsilon_b - \varepsilon_u)\,\Gamma_4\} \qquad (3.14a)$$

$$\alpha_1 = (k_0^2 / 2\beta)\,\varepsilon''\Gamma_2 \qquad (3.14b)$$

$$\alpha_2 = (k_0^2 / 2\beta)\,\varepsilon''_f\,\Gamma_2 \qquad (3.14c)$$

$$K_m = K_{-m} = \Gamma_4 \left(\frac{k_0^2}{2\beta}\right) \frac{(\varepsilon_{cl} - \varepsilon_c)}{\pi m} \sin\left(\pi m \frac{W_1}{\Lambda}\right) \qquad (3.14d)$$

$$\Omega_m = \frac{\pi}{\Lambda} m\,(W_1 + 2R_1) = -\Omega_{-m} \qquad (3.14e)$$

$(m \neq 0)$

K_m is the coupling coefficient of the mth-order circular grating. Δ is in fact the difference of the propagation constant in the gain region and that in the grating region. Ω_m is the phase-shift due to the center region. α_1 and α_2 denote the field gain (or loss). For CG-DFB lasers, $\alpha_1 = \alpha_2$; for CG-DBR lasers, $\alpha_2 = 0$.

The Γ's in Eq.(3.14) are the overlap integrals defined by

$$\Gamma_2 = \int_{d_1}^{d_2} |Z|^2\,dz \Big/ \int_{-\infty}^{\infty} |Z|^2\,dz \qquad (3.15a)$$

$$\Gamma_3 = \int_{d_2}^{d_3} |Z|^2\,dz \Big/ \int_{-\infty}^{\infty} |Z|^2\,dz \qquad (3.15b)$$

$$\Gamma_4 = \int_{d_3}^{d_4} |Z|^2 \, dz \, / \int_{-\infty}^{\infty} |Z|^2 \, dz \tag{3.15c}$$

Γ_2 is actually the confinement factor of the active layer and Γ_4 the overlap integral of the grating layer.

3.3.2 Solution for $0 < r < R_1$

By substitution of Eq.(3.13a) into Eq.(3.10), the coupled-wave equations becomes:

$$\frac{da_n^+}{dr} = -j(\Delta + j\alpha_1)[a_n^+(r) + j(-1)^n e^{j2\beta r} a_n^-(r)] \tag{3.16a}$$

$$\frac{da_n^-}{dr} = j(\Delta + j\alpha_1)[-j(-1)^n e^{-j2\beta r} a_n^+(r) + a_n^-(r)] \tag{3.16b}$$

for $0 < r < R_1$. Neglecting the fast oscillating terms in Eq.(3.16), we get

$$\frac{da_n^+}{dr} \approx -j(\Delta + j\alpha_1) a_n^+(r) \tag{3.17a}$$

$$\frac{da_n^-}{dr} \approx j(\Delta + j\alpha_1) a_n^-(r) \tag{3.17b}$$

The solution of Eq.(3.17) is

$$a_n^+(r) = a_n^+(0) \, e^{-j(\Delta + j\alpha_1)r} \tag{3.18a}$$

$$a_n^-(r) = a_n^-(0) \, e^{j(\Delta + j\alpha_1)r} \tag{3.18b}$$

In matrix form, we have

$$\begin{bmatrix} a_n^+(r) \\ a_n^-(r) \end{bmatrix} = \begin{bmatrix} e^{-j(\Delta+j\alpha_1)r} & 0 \\ 0 & e^{j(\Delta+j\alpha_1)r} \end{bmatrix} \begin{bmatrix} a_n^+(0) \\ a_n^-(0) \end{bmatrix} \qquad (0 < r < R_1) \tag{3.19}$$

3.3.3 Solution for $R_1 < r < \infty$

For $R_1 < r < \infty$, from Eq.(3.10) and Eq.(3.13.b), we have

$$\frac{da_n^+}{dr} = -j \left[j\alpha_2 - \sum_{m=-\infty}^{\infty}{}' K_m e^{-j\Omega_m} e^{j\frac{2\pi}{\Lambda} m r} \right] \left[a_n^+(r) + j(-1)^n e^{j2\beta r} a_n^-(r) \right] \tag{3.20a}$$

$$\frac{da_n^-}{dr} = j \left[j\alpha_2 - \sum_{m=-\infty}^{\infty}{}' K_m e^{-j\Omega_m} e^{j\frac{2\pi}{\Lambda} m r} \right] \left[-j(-1)^n e^{-j2\beta r} a_n^+(r) + a_n^-(r) \right] \tag{3.20b}$$

Let δ denote the deviation from the Bragg frequency of the grating with

$$\delta = \beta - \frac{\pi}{\Lambda} m \tag{3.21}$$

Then, if $|\delta| << 1$, we can keep only the resonant terms in Eq.(3.20) and obtain

$$\frac{da_n^+}{dr} = \alpha_2 a_n^+ - (-1)^n K_m e^{j\Omega_m} e^{j2\delta r} a_n^-(r) \tag{3.22a}$$

$$\frac{da_n^-}{dr} = -(-1)^n K_m e^{-j\Omega_m} e^{-j2\delta r} a_n^+(r) - \alpha_2 a_n^-(r) \tag{3.22b}$$

The solution of Eq.(3.22) can be obtained in the form of

$$\begin{bmatrix} a_n^+(r) \\ a_n^-(r) \end{bmatrix} = \begin{bmatrix} T_{11}(r) & T_{12}(r) \\ T_{21}(r) & T_{22}(r) \end{bmatrix} \begin{bmatrix} a_n^+(R_1) \\ a_n^-(R_1) \end{bmatrix} \quad (r > R1) \tag{3.23}$$

where

$$\gamma = \sqrt{K_m^2 + (\alpha_2 - j\delta)^2} \tag{3.24a}$$

$$T_{11}(r) = e^{j\delta(r-R_1)} \{\cosh[\gamma(r-R_1)] + (\frac{\alpha_2 - j\delta}{\gamma}) \sinh[\gamma(r-R_1)]\} \tag{3.24b}$$

$$T_{12}(r) = -(-1)^n (K_m/\gamma) e^{j\Omega_m} e^{j\delta(r+R_1)} \sinh[\gamma(r-R_1)]\} \tag{3.24c}$$

$$T_{21}(r) = -(-1)^n (K_m/\gamma) e^{-j\Omega_m} e^{-j\delta(r+R_1)} \sinh[\gamma(r-R_1)]\} \tag{3.24d}$$

$$T_{22}(r) = e^{-j\delta(r-R_1)} \{\cosh[\gamma(r-R_1)] - (\frac{\alpha_2 - j\delta}{\gamma}) \sinh[\gamma(r-R_1)]\} \tag{3.24e}$$

3.3.4 Threshold Eigenvalue Equation

At $r = R_2$ where R_2 is the outer radius of the grating region ($R_2 > R_1$), Eq.(3.23) gives

$$\begin{bmatrix} a_n^+(R_2) \\ a_n^-(R_2) \end{bmatrix} = \begin{bmatrix} T_{11}(R_2) & T_{12}(R_2) \\ T_{21}(R_2) & T_{22}(R_2) \end{bmatrix} \begin{bmatrix} a_n^+(R_1) \\ a_n^-(R_1) \end{bmatrix} \tag{3.25}$$

From Eq.(3.19), we have

$$\begin{bmatrix} a_n^+(R_1) \\ a_n^-(R_1) \end{bmatrix} = \begin{bmatrix} e^{(-j\Delta + \alpha_1)R_1} & 0 \\ 0 & e^{-(-j\Delta + \alpha_1)R_1} \end{bmatrix} \begin{bmatrix} a_n^+(0) \\ a_n^-(0) \end{bmatrix} \tag{3.26}$$

Substitution of Eq.(3.26) into Eq.(3.25), we obtain

$$\begin{bmatrix} a_n^+(R_2) \\ a_n^-(R_2) \end{bmatrix} = \begin{bmatrix} T_{11}(R_2)\, e^{(-j\Delta+\alpha_1)R_1} & T_{12}(R_2)\, e^{-(-j\Delta+\alpha_1)R_1} \\ T_{21}(R_2)\, e^{(-j\Delta+\alpha_1)R_1} & T_{22}(R_2)\, e^{-(-j\Delta+\alpha_1)R_1} \end{bmatrix} \begin{bmatrix} a_n^+(0) \\ a_n^-(0) \end{bmatrix} \tag{3.27}$$

Thus, the ratio of the amplitude of the inward-wave to that of the outward-wave is

$$\frac{a_n^-(R_2)}{a_n^+(R_2)} = \frac{\rho_0 T_{21}(R_2)\, e^{(-j\Delta+\alpha_1)R_1} + T_{22}(R_2)\, e^{-(-j\Delta+\alpha_1)R_1}}{\rho_0 T_{11}(R_2)\, e^{(-j\Delta+\alpha_1)R_1} + T_{12}(R_2)\, e^{-(-j\Delta+\alpha_1)R_1}} \tag{3.28}$$

where ρ_0 is the reflection coefficient ar r=0 defined as

$$\rho_0 = \frac{a_n^+(0)}{a_n^-(0)} \tag{3.29}$$

Similar to one-dimensional DFB lasers [2], in order to create self-sustained oscillations, the ratio of the amplitude of the incoming wave to that of the outgoing wave at the boundary $r=R_2$ must be zero with

$$\frac{a_n^-(R_2)}{a_n^+(R_2)} = 0 \tag{3.30}$$

This condition gives the eigenvalue equation for circular grating lasers :

$$\rho_0 T_{21}(R_2)\, e^{(-j\Delta+\alpha_1)R_1} + T_{22}(R_2)\, e^{-(-j\Delta+\alpha_1)R_1} = 0 \tag{3.31}$$

or in another form

$$\rho_0 \left[-\frac{T_{21}(R_2)}{T_{22}(R_2)} \right] e^{-j2\Delta R_1}\, e^{2\alpha_1 R_1} = 1 \tag{3.32}$$

From Eq.(3.25) and Eq.(3.30), we also have

$$T_{21}(R_2)\, a_n^+(R_1) + T_{22}(R_2)\, a_n^-(R_1) = 0 \tag{3.33}$$

Defining the reflection coefficient of the grating seen from $r = R_1$ outward by

$$\rho_{R_1} = \frac{a_n^-(R_1)}{a_n^+(R_1)} \tag{3.34}$$

Then, the eigenvalue equation in Eq.(3.32) can also be expressed as

$$\rho_0 \rho_{R_1} e^{-j2\Delta R_1} e^{2\alpha_1 R_1} = 1 \tag{3.35}$$

Eq.(3.35) is similar to the eigenvalue equation for conventional DBR lasers [87-88]. However, because the field must be finite at r=0, we must require :

$$a_n^+(0) = a_n^-(0) \tag{3.36}$$

i.e, $\rho_0 = 1$. This is equivalent to having a mirror with 100% reflectivity at the center.

Substitution of T_{21} and T_{22} from Eq.(3.24) into Eq.(3.34), we obtain explicitly :

$$\rho_{R_1} = \frac{(-1)^n K_m e^{-j\Omega_m} e^{-j2\delta R_1} \sinh[\gamma (R_2 - R_1)]}{\gamma \cosh[\gamma (R_2 - R_1)] - (\alpha_2 - j\delta) \sinh[\gamma (R_2 - R_1)]} \tag{3.37}$$

Note that the reflection coefficient ρ_{R_1} of the circular grating depends on the order of the cylindrical waves. This dependence is represented by the factor $(-1)^n$ in Eq.(3.37). For n=even, we have $(-1)^n = 1 > 0$; and for n=odd, $(-1)^n = -1 < 0$. We see that the magnitude of ρ_{R_1} is the same for all the cylindrical waves, but the sign for even order waves is positive and that for odd order waves is negative. This sign difference give different threshold gains for the even and odd order waves as will be seen below. However, all the even order waves have the the same threshold and so do all the odd order waves. The degeneracy

among the even (odd) order cylindrical waves is a direct result of the large radius approximation.

3.5 Threshold Gain of CG-DFB and CG-DBR Lasers

For simplicity, we consider only first-order gratings in our calculation. The results presented here could be used as a guideline for second-order gratings, because the effect of radiation can be considered as a loss factor [21]. We introduce the following parameters to facilitate the calculation:

$$S = R_1 / L$$

$$L = R_2 - R_1 = R_2 / (1+S)$$

$$\Omega = \Omega_m + 2 \Delta R_1 \qquad (3.38)$$

where Ω is actually the total phase-shift experienced by the cylindrical wave in the center region.

3.5.1 Mode Spectrum and Threshold Gain of CG-DFB Lasers

In the case of DFB lasers, because the active material extends over the whole grating region, we have $\alpha_1=\alpha_2=\alpha$.

In Figs.12(a)-(d), the normalized threshold gain $\alpha_{th}R_2$ is plotted against the normalized frequency deviation δR_2 for $\Omega=\pi/2$, π, $3\pi/2$ and 2π. The open and the solid circles represent the even-order and the odd-order cylindrical waves, respectively. The calculation is done for $KR_2=1.0$ and $S=0.0$. It is seen that for $\Omega=\pi/2$, the even cylindrical waves and the odd cylindrical waves have the same threshold gain, but the even cylindrical waves oscillate at a lower frequency ($\delta R_2 < 0$) than the odd ones ($\delta R_2 > 0$). The even cylindrical waves and the odd cylindrical waves are located symmetrically with respect to the Bragg frequency ($\delta R_2=0$). The same can be said for $\Omega=3\pi/2$ except that the lasing frequency of

the even waves and that of the odd waves are now interchanged. For $\Omega=\pi$, as shown in Fig.12(c), the odd waves have a much lower threshold gain than the even waves. The reverse is true for $\Omega=2\pi$. This clearly shows that by properly choosing the phase Ω, we can select either the even or the odd order cylindrical waves. This selectivity may be very important in designing CG-DFB lasers.

As shown by Eq.(3.38), the total phase-shift Ω is a function of the inner radius R_1. However, once the phase Ω is fixed, the influence of R_1 on threshold gain is negligible because R_1 is usually very small in comparison to the outer radius R_2 in CG-DFB lasers. This fact is shown in Figs.13(a)-(d) where we compare the case of S=0.0 and S=0.01 for even-order cylindrical waves. For $L=R_2-R_1=140$ μm, S=0.01 means an inner radius of $R_1=1.4$ μm. The threshold gain for S=0.01 is only slightly lower than for the case where S=0. Therefore, for a given phase-shift Ω, our calculation for S=0.0 offers a good estimation of the threshold gain of CG-DFB lasers.

In Fig.14(a), the normalized threshold gain of the lowest mode is shown as a function of Ω ($0 < \Omega < 2\pi$). The corresponding lasing frequency is presented in Fig.14(b). We conclude from these two figures that the lowest threshold gain occurs at the Bragg frequency ($\delta R_2=0$). This can be achieved by choosing $\Omega=2\pi$ for n=even, and $\Omega=\pi$ for n=odd. Fig.14(a) also shows that for $0 < \Omega < (1/2)\pi$ or $(3/2)\pi < \Omega < 2\pi$, the even waves have a lower threshold gain than the odd waves; the reverse is true for $(1/2)\pi < \Omega < (3/2)\pi$ It is seen from Fig.14(b) that for $0 < \Omega < \pi$, the even and odd waves oscillate below and above the Bragg frequency, respectively; for $\pi < \Omega < 2\pi$, the roles of the even and odd waves are interchanged. This characteristics can be used to distinguish the even waves from the odd waves.

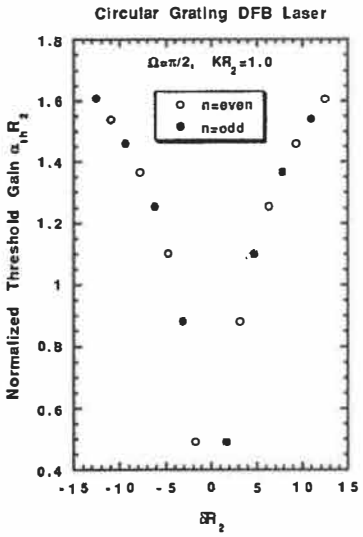

(a)

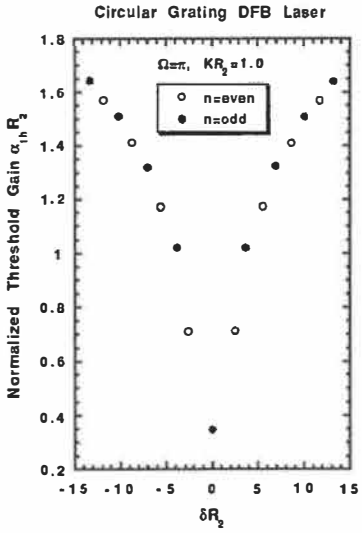

(b)

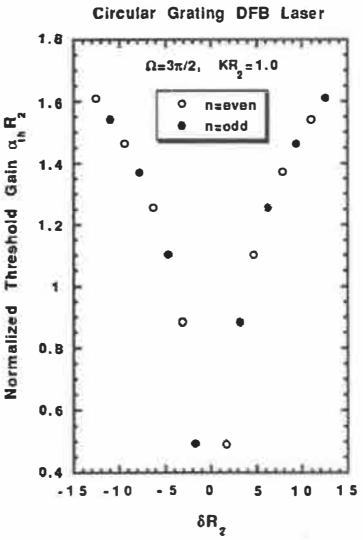

(c)

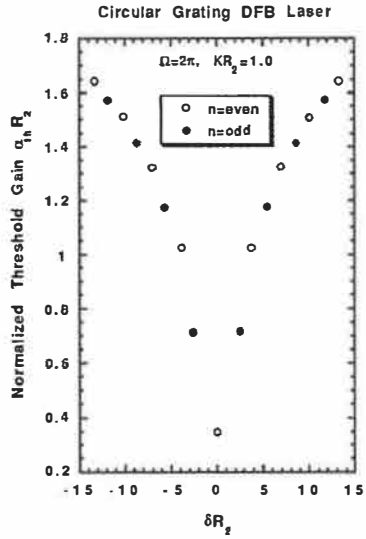

(d)

Fig.12 Mode spectrum of CG-DFB laser with KR_2=1.0 and S=0.0: (a) Ω=π/2; (b) Ω=π; (c) Ω=3π/2; (d) Ω=2π.

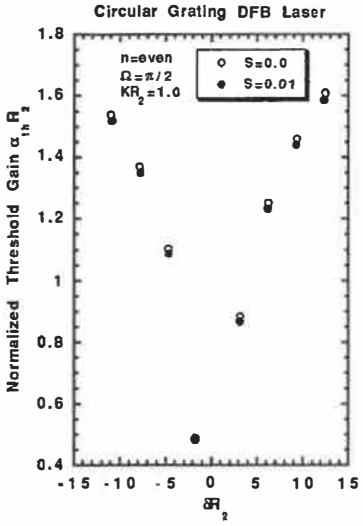

(a)

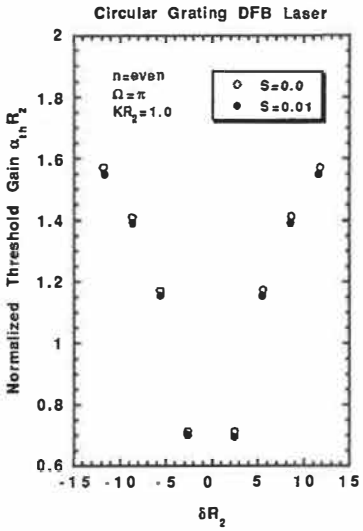

(b)

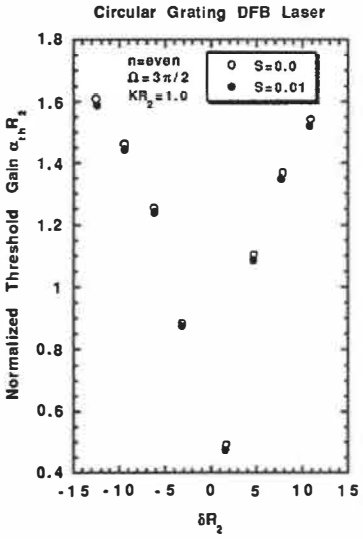

(c)

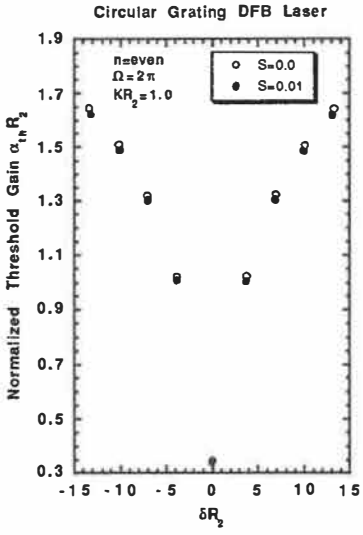

(d)

Fig.13 Effect of S on the mode spectrum of even order cylindrical waves in CG-DFB laser with KR_2=1.0, S=0.0 and S=0.01 : (a) $\Omega=\pi/2$; (b) $\Omega=\pi$; (c) $\Omega=3\pi/2$; (d) $\Omega=2\pi$.

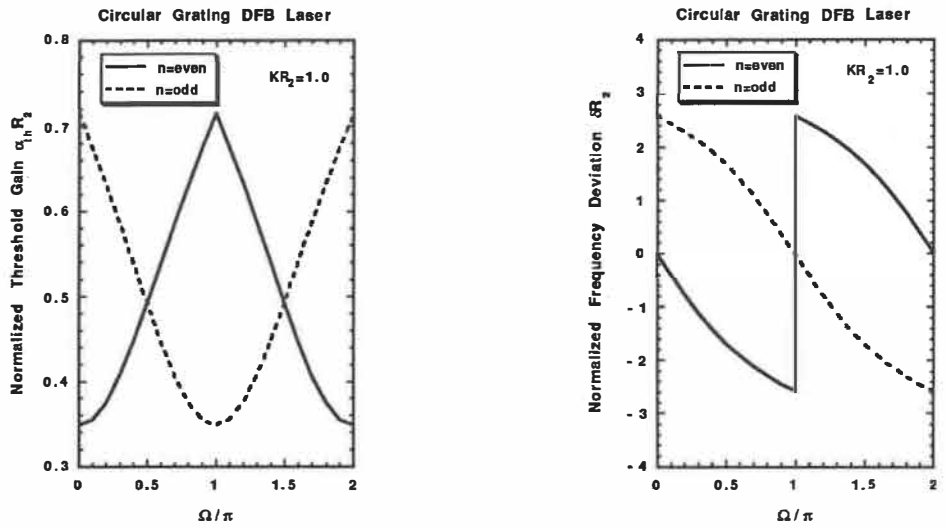

(a) (b)

Fig.14 Effect of the total phase-shift Ω on CG-DFB laser: (a) normalized threshold gain versus Ω; (b) normalized lasing frequency as a function of Ω.

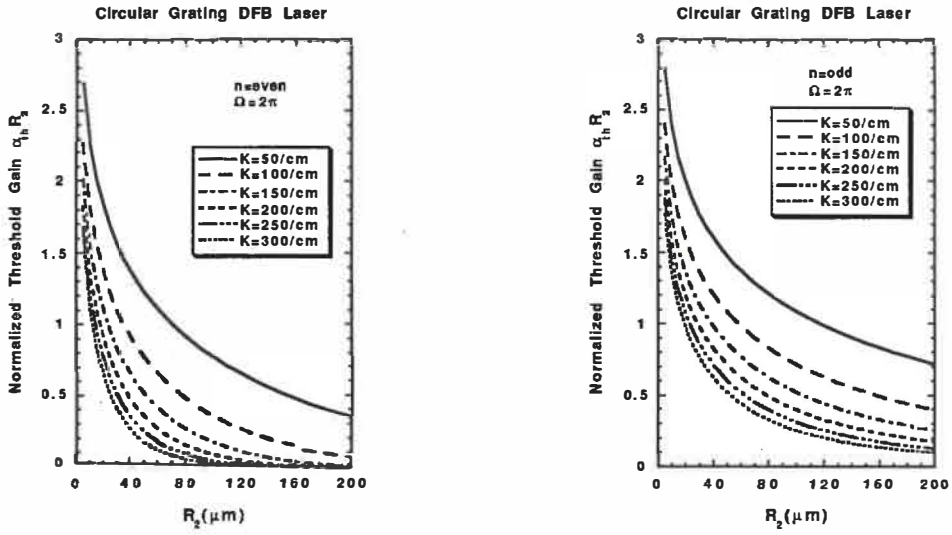

(a) (b)

Fig.15 Normalized threshold gain of CG-DFB laser as a function of grating radius R_2 with the coupling coefficient as a parameter : (a) n=even ; (b) n=odd.

The normalized threshold gain is shown as a function of the grating radius R_2 in Fig.15(a) for n=even and in Fig.15(b) for n=odd, respectively. For both cases the normalized threshold gain $\alpha_{th}R_2$ decreases as the grating radius R_2 increases.

3.5.2 Mode Spectrum and Threshold Gain of CG-DBR Lasers

For CG-DBR lasers, the gain region is limited within a circle of radius R_1 and the grating region has a length of $L=R_2-R_1$ (see Fig.9(b)). In the following calculation, we ignore the losses in the grating region, i.e., with $\alpha_2=0$. Then, from Eq.(3.14), we have $\alpha=\alpha_1$. Note that the inner radius R_1 of CG-DBR lasers is large compared to that of CG-DFB lasers.

Figs.16(a)-(d) show the mode spectrum of CG-DBR lasers for S=0.2 and KL=1.0. The phase Ω is used as a parameter. For a grating length $L=R_2-R_1=140\mu m$, S=0.2 is equivalent to an inner radius of $R_1=28\mu m$. Similarly to the case of CG-DFB lasers (see Figs.12(a)-(d)), for $\Omega=2\pi$, the even wave has the lowest threshold and oscillates right at the Bragg frequency; for $\Omega=\pi$, it is the odd wave that has the lowest threshold gain and lases at the Bragg frequency. For $\Omega=\pi/2$, the even and the odd waves have the same threshold gain, but the even wave oscillates below, and the odd wave above the Bragg frequency; for $\Omega=3\pi/2$, the role of the even waves and that of the odd waves are reversed.

In Figs.17(a)-(b), the normalized threshold gain is plotted against the phase Ω for n=even and n=odd, respectively. The lasing frequency of the modes is shown in Figs.17(c)-(d). As in the case of CG-DFB laser, for $0 < \Omega < (1/2)\pi$ or $(3/2)\pi < \Omega < 2\pi$, the even waves have a lower threshold gain than the odd waves; and it is just the opposite for $(1/2)\pi < \Omega < (3/2)\pi$. The even order waves have the lowest threshold gain and oscillate at the Bragg frequency when $\Omega=2\pi$; The same can be said about the odd order waves when $\Omega=\pi$. According to Figs.17(c), even wave oscillation occurs below the Bragg frequency when $0 < \Omega < \pi$, and above when $\pi < \Omega < 2\pi$. The results are just the opposite for odd wave oscillations (see Fig.17(d)).

In Figs.18(a)-(b), the normalized threshold gain is shown as a function of the gain region radius R_1 for n=even and n=odd, respectively. The phase Ω is set to 2π and the coupling coefficient K is used as a parameter. Fig.18(a) is plotted in the log scale because the normalized threshold gain is too small for $K=250cm^{-1}$. Note that for n=even and $\Omega=2\pi$, the lasing frequency is right at the Bragg frequency. In this case, the normalized threshold gain $\alpha_{th}R_1$ is a function of the coupling coefficient K only (see Eq.(3.35) with $\delta=0$). For

n=odd, because the lasing frequency is not located at the Bragg frequency and is dependent of the ratio $S=R_1/(R_2-R_1)$, the normalized threshold gain decreases monotonously as R_1 increases. This difference between the even waves and the odd waves makes the corresponding threshold current behave differently as to be seen in the next section.

3.6 Threshold Current of CG-DFB and CG-DBR Lasers

In the previous section, we have just calculated the mode field gain for CG-DFB and CG-DBR lasers. We have learned that by a proper choice of the phase shift, we can select either the even cylindrical waves or the odd cylindrical waves. We have found that the lowest threshold gain for the even cylindrical waves and for odd cylindrical waves is at $\Omega=2\pi$ and $\Omega=\pi$, respectively. The lasing frequency is then right at the Bragg frequency. This is true for both the CG-DFB and the CG-DBR lasers. In this section, we give an estimation of the threshold current density and the threshold current of CG-DFB and CG-DBR lasers. The analysis is based on a linear model for the relation between the material gain and the carrier density. The information obtained here is important in designing a good circular grating laser.

3.6.1 Model

In order to analyze the threshold current and threshold current density, it is more appropriate to use the material gain g. As in [88], the relationship between the material gain and the field gain can be obtained as

$$g_{th}\,\Gamma_2 = 2\,\alpha_{th} + \alpha_{int} \tag{3.39}$$

where Γ_2 is the optical confinement factor of the active layer defined by Eq.(3.15a), g_{th} is the material threshold gain, α_{th} is the threshold field gain calculated from Eq.(3.35) and α_{int} is the total internal power loss.

Assuming that the gain satisfies the following linear relation [88]:

$$g(N) = A_0\,(N - N_0) \tag{3.40}$$

where g is the peak gain, A_0 is the gain coefficient, N is the carrier density and N_0 is the carrier density to achieve transparency (corresponding to the onset of population inversion), the threshold carrier density N_{th} is obtained from Eqs.(3.39)-(3.40) as

$$N_{th} = N_0 + (2\,\alpha_{th} + \alpha_{int})/(A_0\Gamma_2) \tag{3.41}$$

and the threshold current density J_{th} can be calculated from [89] :

$$J_{th} = e\,(d_a/\eta_i)\,B_{eff}\,(N_{th})^2 \tag{3.42}$$

In Eq.(3.42), e is the charge of an electron, d_a is the thickness of the active layer, η_i is the internal quantum efficiency, B_{eff} is the effective recombination constant.

As before, we use 1.3 μm InGaAsP/InP CG-DFB and CG-DBR lasers as examples. The following parameters are used in the calculation : A_0=2.5x10^{-16} cm^2, N_0 =1.5x10^{18} cm^{-3}, B_{eff} = 1.0x10^{-10} cm^{3}s^{-1} [89], Γ = 0.5, d_a = 0.2 μm, η_i = 1 and α_{int} = 50 cm^{-1}.

3.6.2 Threshold Current of CG-DFB Lasers

For CG-DFB lasers, the whole grating region of radius R_2 is pumped. Then, the threshold current I_{th} is obtained from :

$$I_{th} = \pi\,(R_2)^2\,J_{th} \tag{3.43}$$

where R_2 is the outermost radius of the circular grating.

Fig.19(a) shows the threshold current density as a function of the grating radius R_2 for even cylindrical waves and different values of the coupling coefficient K. The corresponding threshold current is shown in Fig.19(b). The threshold current density first decreases as the grating radius increases. With further increase of the grating radius, the threshold current density approaches a lower limit. This is expected because the threshold gain α_{th} is a decreasing function of R_2 as shown in Fig.15(a). The lower limit exists because a certain amount of current is needed to achieve transparency and compensate the total internal loss. For each value of K, there is an optimum grating radius that gives the lowest threshold current. This can be explained as follows: for small R_2, because α_{th}

decreases much faster than $1/R_2$ (see Fig.15(a)), J_{th} decreases much faster than $(1/R_2)^2$, and thus overcomes the increase of I_{th} due to $(R_2)^2$ (see Eq.(3.43)). For larger R_2, the factor $(R_2)^2$ in Eq.(3.43) becomes dominant, therefore, I_{th} goes up as R_2 increases. Depending on the coupling coefficient K, the optimum grating radius for CG-DFB is between 40-80 μm.

A comparison between the even wave and the odd wave is shown in Figs.20(a)-(b) for $\Omega=2\pi$ and K=300 cm^{-1}. For CG-DFB lasers, the threshold current of the odd waves follows the same trend as the even waves but has a higher value. At the optimum radius, the threshold current of the odd waves is about twice that of the even waves.

3.6.3 Threshold Current of CG-DBR Laser

For CG-DBR lasers, the gain region is confined within a circle of radius R_1. The threshold current is then calculated from :

$$I_{th} = \pi (R_1)^2 J_{th} \tag{3.44}$$

The threshold current density for CG-DBR lasers is presented in Figs.21(a)-(b). The threshold current is shown in Figs.22(a)-(b). The comparison between even wave and odd wave is given in Figs.23(a)-(b).

The threshold current of even waves increases monotonously as a function of R_1, while that of odd waves has a minimum at a certain radius. The reason for the even waves to behave differently from the odd waves is that for even waves, the threshold gain α_{th} decreases as $1/R_1$ (see Fig.18(a)). When substituted into Eq.(3.44), I_{th} becomes proportional to $(R_1)^2$, thus gives the monotonously increasing behavior. The explanation for odd waves is similar to the case of CG-DFB lasers. Because α_{th} decreases much faster than $1/R_1$ (see Fig.18(b)), J_{th} decreases much faster than $(1/R_1)^2$, thus overcomes the increase of I_{th} due to $(R_1)^2$ (see Eq.(3.44)). For larger R_1, the factor $(R_1)^2$ in Eq.(3.44) becomes dominant, therefore, I_{th} goes up as R_1 increases. Another interesting feature is that for a reasonable gain region radius, both the threshold current density and the threshold current of even waves are much less than those of odd waves.

3.6.4 Discussions

Comparing the results for CG-DFB lasers with those for CG-DBR lasers, we observe that the latter has a much lower threshold current density and a much lower threshold current than the former. For example, for $K=100cm^{-1}$, the threshold current density is $9.82kA/cm^2$ (Fig.19(a)) and the threshold current is 494 mA (Fig.19(b)) for a CG-DFB laser (n=even, $\Omega=2\pi$, $R_2=40\mu m$), while the corresponding values of a CG-DBR laser (n=even, $\Omega=2\pi$, $R_1=40\mu m$) is only $1.47kA/cm^2$ (Fig.21.(a)) and 74 mA (Fig.22(a)), respectively. The values for CG-DBR lasers are about seven times less than those for CG-DFB lasers.

3.7 Summary

In this Chapter, a detailed threshold analysis for TE-cylindrical waves in CG-DFB and CG-DBR lasers is presented. The analysis is based on the large radius approximation of the coupled-wave theory developed in Chapter 1-2. Our numerical results show that by proper choice of the phase Ω (in other words, the inner radius R_1), we can select either the even wave or the odd wave. This is an important result for the design of practical CG-DFB and CG-DBR lasers. We have also shown that CG-DFB lasers normally have a higher a higher threshold current density and a higher threshold current than CG-DBR lasers.

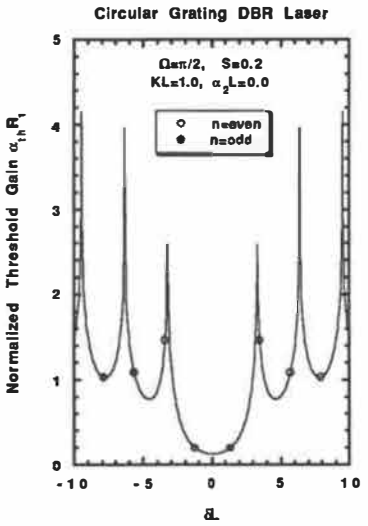

(a)

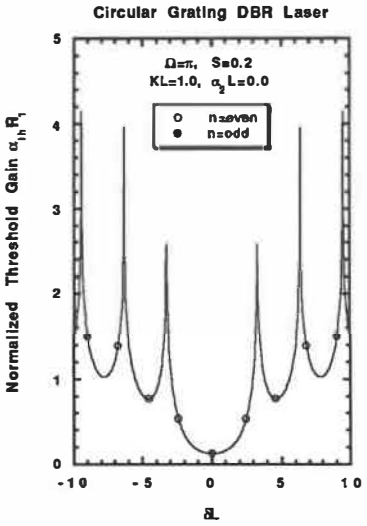

(b)

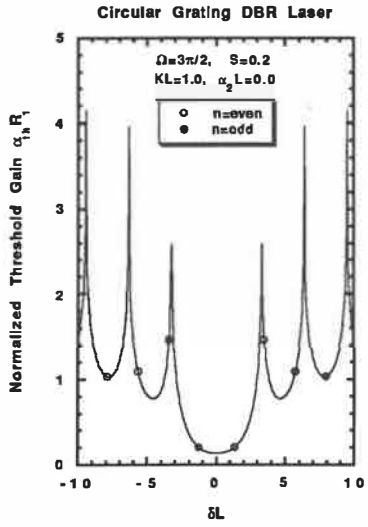

(c)

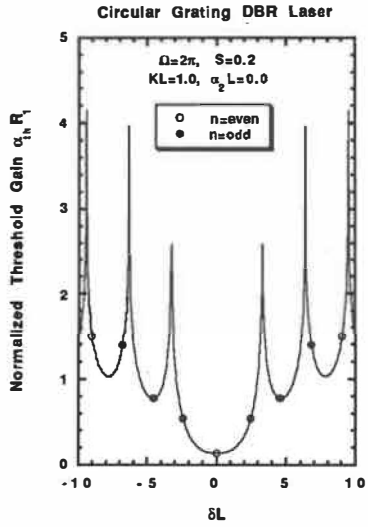

(d)

Fig.16 Mode spectrum of CG-DBR laser with KL=1.0, α_2L=0.0 and S=0.2: (a) $\Omega=\pi/2$; (b) $\Omega=\pi$; (c) $\Omega=3\pi/2$; (d) $\Omega=2\pi$.

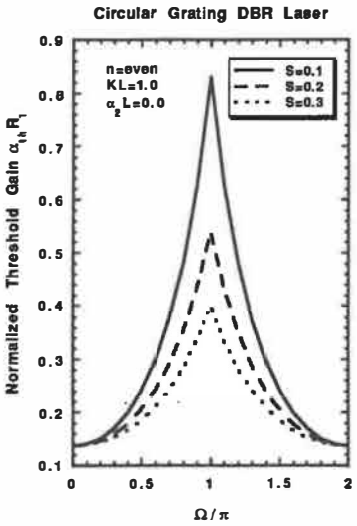

(a)

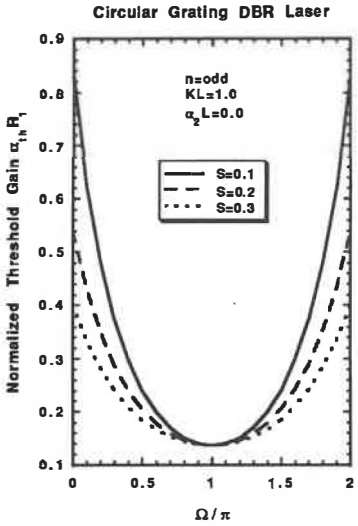

(b)

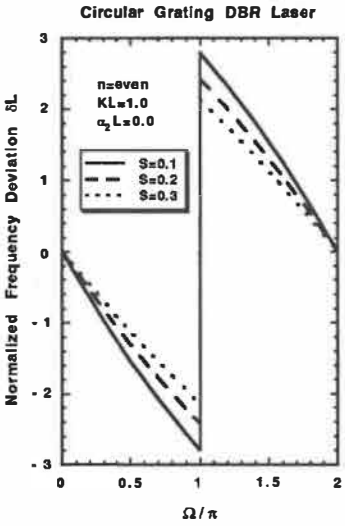

(c)

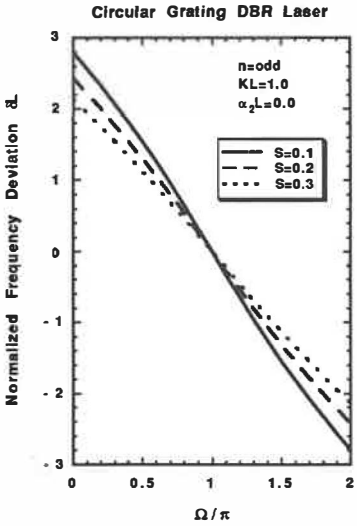

(d)

Fig.17 Effect of the total phase-shift Ω on CG-DBR laser: (a) normalized threshold gain versus Ω for n=even; (b) normalized threshold gain versus Ω for n=odd; (c) lasing frequency against Ω for n=even; (d) lasing frequency against Ω for n=odd.

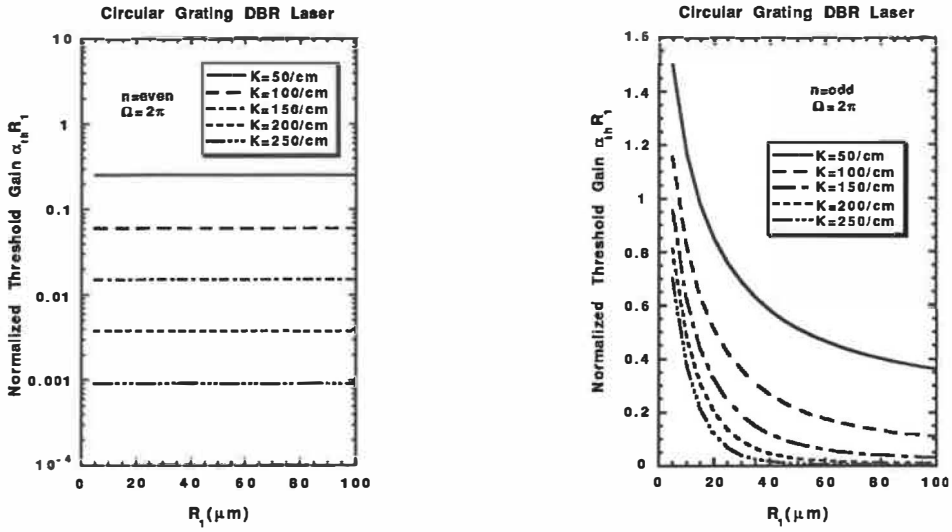

(a) (b)

Fig.18 Normalized threshold gain of CG-DBR laser as a function of gain region radius R_1 : (a) n=even; (b) n=odd.

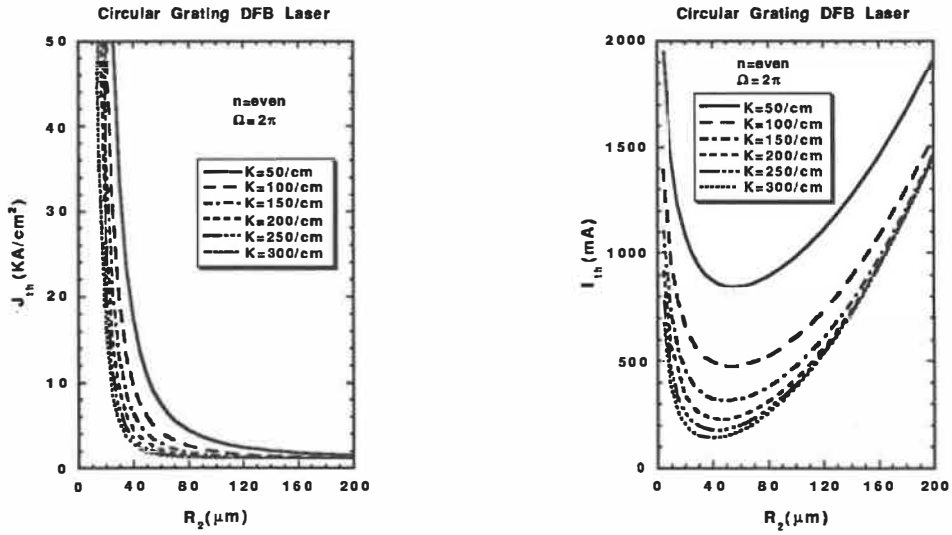

(a) (b)

Fig.19 Threshold current density and threshold current of CG-DFB laser as a function of grating radius R_2 for n=even and $\Omega=2\pi$: (a) threshold current density versus R_2 ; (b) threshold current versus R_2.

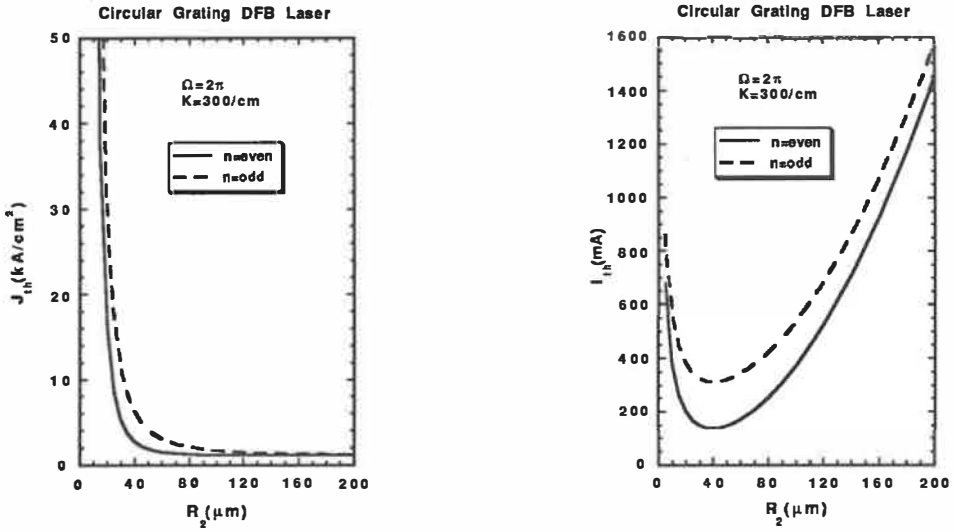

(a) (b)

Fig.20 Comparison of even waves with odd waves in a CG-DFB laser : (a) threshold current density versus grating radius R_2 ; (b) threshold current versus grating radius R_2.

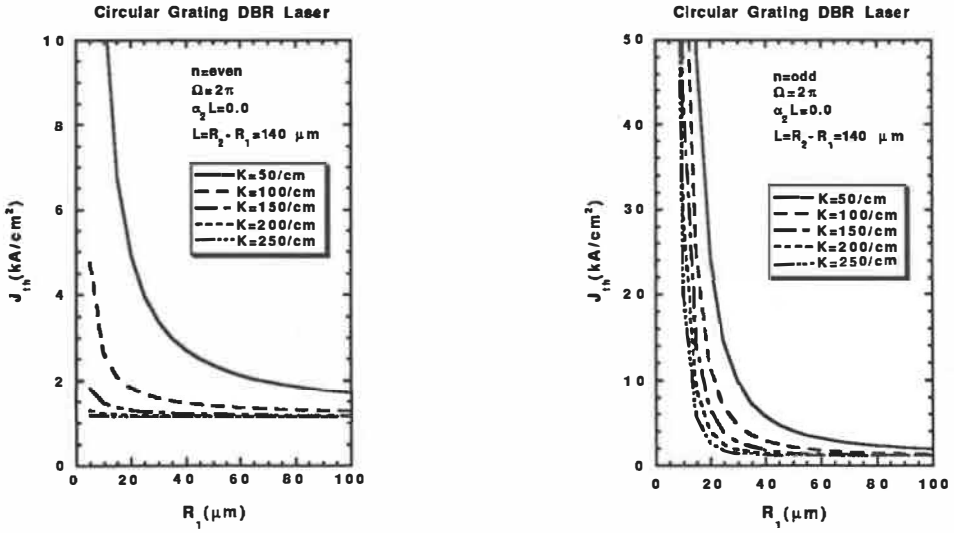

(a) (b)

Fig.21 Threshold current density of CG-DBR laser versus gain region radius R_1 for $\Omega=2\pi$, $\alpha_2 L=0.0$ and $L=R_2-R_1=140\mu m$: (a) n=even ; (b) n=odd.

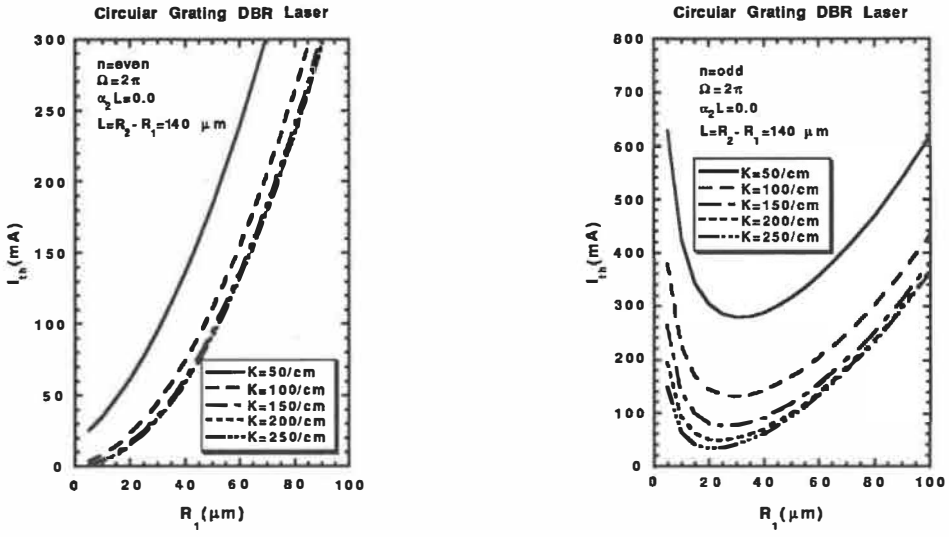

(a) (b)

Fig.22 Threshold current of CG-DBR laser versus gain region radius R_1 (a) n=even ; (b) n=odd.

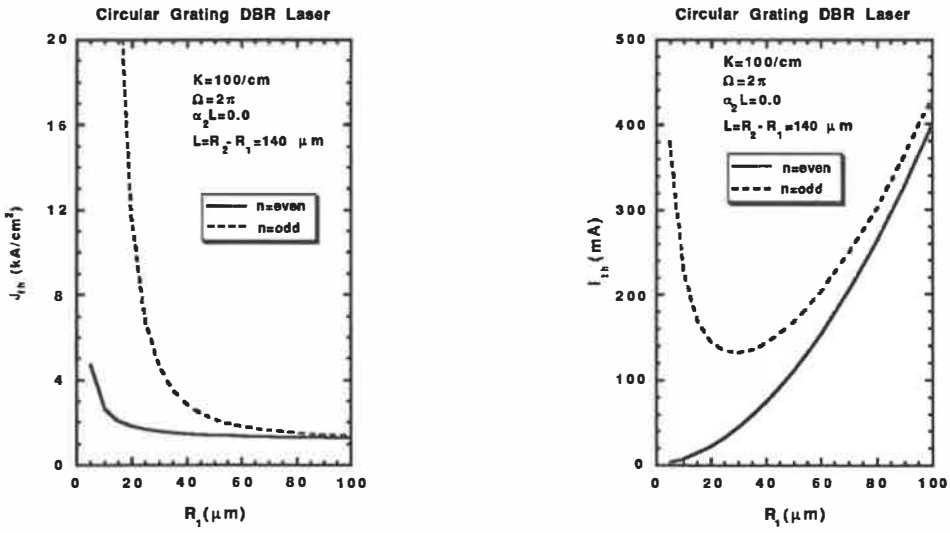

(a) (b)

Fig.23 Comparison of even waves with odd waves in a CG-DBR laser: (a) threshold current density versus gain region radius R_1 ; (b) threshold current against gain region radius R_1.

CHAPTER 4

CIRCULAR GRATING DFB LASERS: FABRICATION AND MEASUREMENTS

4.1 Introduction

In previous chapters, we have formulated the coupled-wave theory for cylindrical waves and applied the theory to analyze CGDFB and CG-DBR lasers. The threshold gain and the threshold current analysis of Chapter 3 gives the design guide lines for practical circular grating lasers.

In this Chapter, we discuss the fabrication of semiconductor CG-DFB lasers and present the measured lasing characteristics of the first optically pumped GaInAsP/InP CG-DFB lasers.

The structure of our CG-DFB laser is first described in Section 4.2. The fabrication procedures are explained in Section 4.3. Experimental results of the first optically-pumped CG-DFB lasers are given in Section 4.4.

4.2 Design of CG-DFB Lasers

Since we are interested in long-wavelength lasers, we choose the InGaAsP/InP double hetero-structure as the semiconductor material to fabricate our CG-DFB lasers. The lasing wavelength is chosen to be at 1.3 μm. Fig.24(a) shows schematically a surface-emitting CG-DFB laser. The cross-section of the CG-DFB laser is illustrated in Fig.24(b).

A surface-emitting CG-DFB laser can be realized by etching second-order circular gratings into the cladding layer. The second-order Bragg reflection provides the necessary feedback to sustain the lasing action while the first-order Bragg effect serves to diffract light

out normally from the surface [57]. This would give us a surface-emitted, circularly symmetric beam.

The planar waveguide formed by the double hetero-structure is designed to support only the fundamental slab mode. The thickness of the active layer (GaInAsP, λ_g = 1.3 μm) is d=0.17 μm. The thickness of the top cladding layer (GaInAsP, λ_g = 1.0 μm) is t = 0.2 μm. The bottom cladding layer (InP) has a thickness of 1.0 μm.

For the planar waveguide depicted in Fig.24, the propagation constant of the fundamental TE-mode is β=15.8215/μm. This means that the grating period of second-order grating is 0.397μm.

Fig.25 shows the coupling coefficient K of a second-order grating against the grating aspect ratio W_1/Λ. The etching depth Δh is used as a parameter. This figure indicates that the optimum aspect ratio for second-order grating is around $W_1/\Lambda = 1/4$.

Fig.26 shows the coupling coefficient K as a function of the etching depth Δh with the grating aspect ratio as a parameter. For reference, the case of first-order grating is also included in the plot.

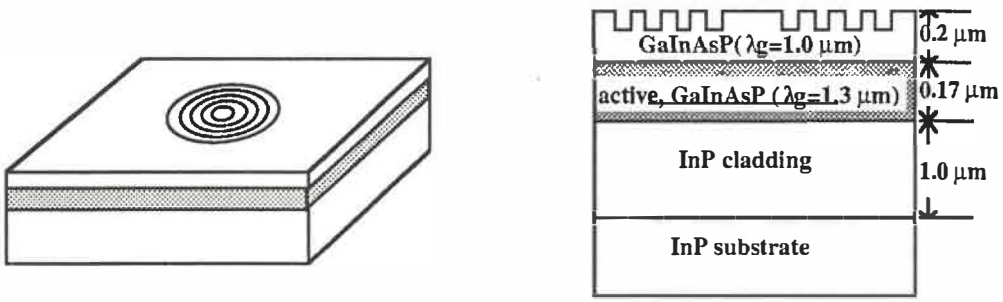

Fig.24 Structure of GaInAsP/InP semiconductor CG-DFB laser: (a) schematic view; (b) cross-section.

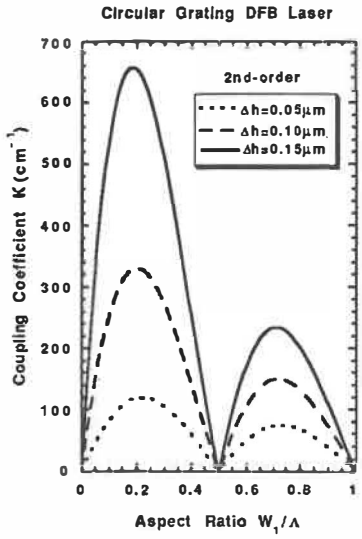

Fig.25 Coupling coefficient K against grating aspect ratio W_1/Λ.

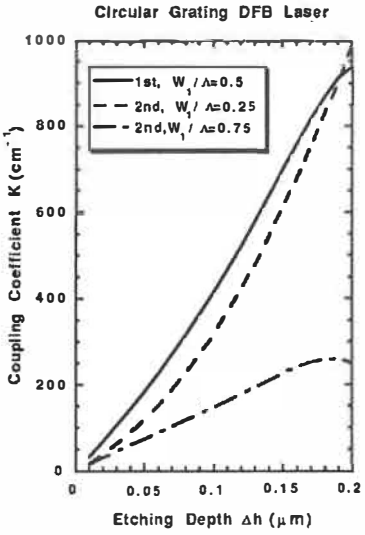

Fig.26 Coupling coefficient K as a function of etching depth Δh.

4.3 Fabrication of CG-DFB Lasers

The fabrication procedures are summarized in Fig.27. First, a double hetero-structure GaInAsP/InP is grown by the metal-organic-chemical-vapor-deposition (MOCVD) technique. Then, a thin layer of SiO_2 (500 Å) is deposited on the top cladding layer. The SiO_2 layer is used for pattern transfer to the semiconductor because of its infinite etching selectivity. After that, a layer of PMMA resist (2000 Å) is spun on top of the SiO_2 layer. Circular gratings are patterned on the PMMA resist by the electron beam (E-beam) lithography [90]. The exposed PMMA is then developed to reveal the circular grating pattern. A two-step reactive-ion-etching (RIE) is used to transfer the desired circular grating from the PMMA to the SiO_2 layer, then into the top cladding layer. The grating is etched to a depth of 0.15μm. The inner and outer diameters of the grating were 1.29μm and 280μm respectively. Fig.28 shows the SEM photograph of a second-order grating CG-DFB laser.

(a) Growth of double hetero-structure by MOCVD

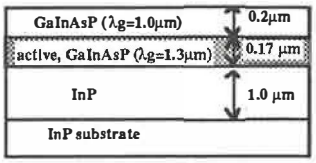

(b) Deposition of SiO_2 (500 Å)

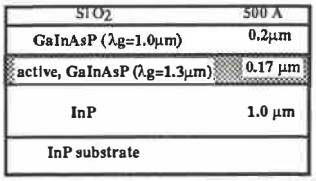

(c) Spin-on of PMMA (2000 Å)

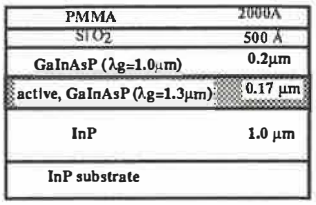

(d) Circular grating patterning by E-beam and development of PMMA

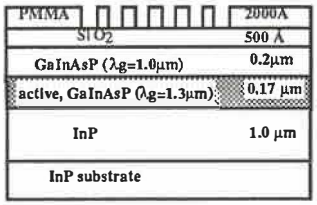

(e) Transfer of circular grating pattern to SiO_2 layer by first RIE

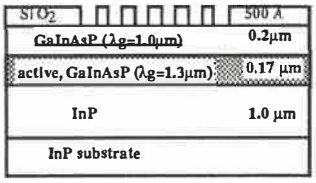

(f) Transfer of circular grating pattern to semiconductor by second RIE

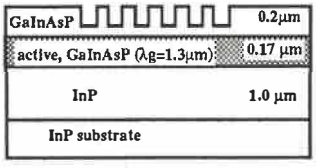

Fig.27 Fabrication procedures of optically-pumped CG-DFB lasers

4.4 Optical Pumping Measurement

The fabricated circular grating DFB lasers are tested by optical pumping at room temperature. The pumping source is a Q-switched and mode-locked YAG laser operating at a wavelength of 1.06μm. The pulse length from the YAG laser is 100 ps, the peak pumping power is up to 22kW.

The experiment setup is shown in Fig.29. The pumping beam is focussed onto the circular grating to a diameter of approximately 1 mm. The light emitted normally from the surface of the semiconductor laser is projected onto an optical power meter or coupled to a spectrum analyzer through an optical fiber for spectral analysis. In measuring the output power from the laser, an optical filter is inserted in front of the photo-detector to remove the pumping radiation of the YAG laser at 1.06μm.

Lasing action is observed at 1.283μm. which is very close to the designed wavelength of 1.3μm. The spectrum is shown in Fig.30. The observed linewidth is 2-3 nm, depending on the pumping power. This large value of the linewidth is due to simultaneous oscillation of the cylindrical wave modes which possess similar lasing thresholds (see Chapter 3 and [63]) and the coupling of the spontaneous emission to the stimulated emission [40]. The output power was measured as a function of the absorbed pumping power and is shown in Fig.31. The absorbed threshold power is estimated to be 10W (pulsed, peak), corresponding to a power density of 16.2kW/cm^2. The maximum pulsed output power is measured to be more than 25mW. This low output efficiency is due, in part, to the large absorption in the unpumped active layer, and in part, to the unoptimized design of the second-order grating used for surface-emission.

4.5 Summary

In this Chapter, the lasing action of optically pumped surface-emitting CG-DFB laser was demonstrated for the first time. The CG-DFB laser was fabricated on the double hetero-structure GaInAsP/InP semiconductor by the E-beam lithography and the reative-ion-etching (RIE) technique. The observed lasing wavelength was 1.283μm. The threshold pumping power density was estimated to be 16.2kW/cm^2. The pulsed output power was more than 25mW.

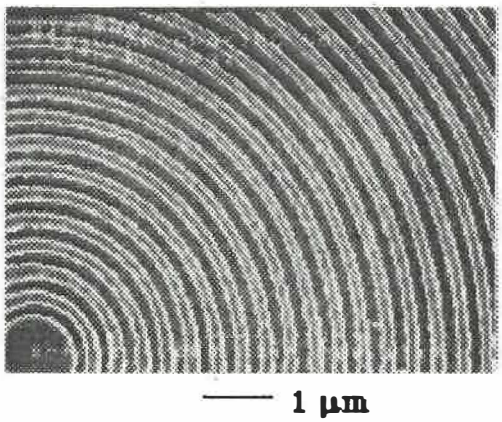

Fig.28 SEM micrograph of circular grating fabricated by E-beam lithography and RIE.

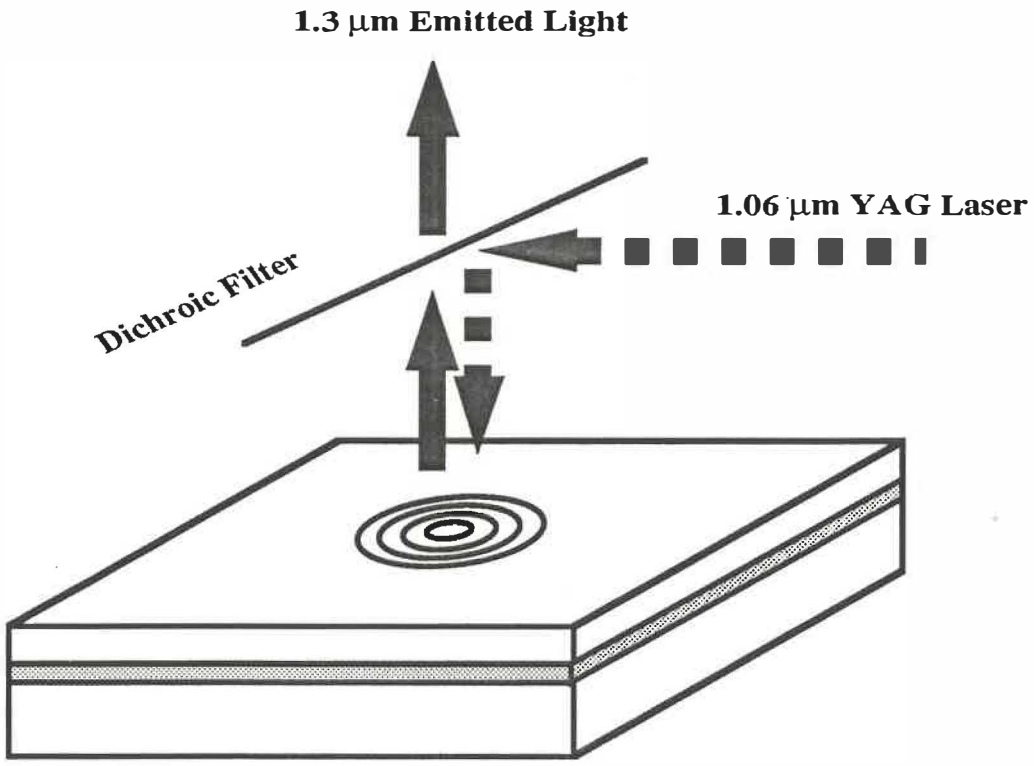

Fig.29 Schematic view of the experimental set-up for optical pumping measurement.

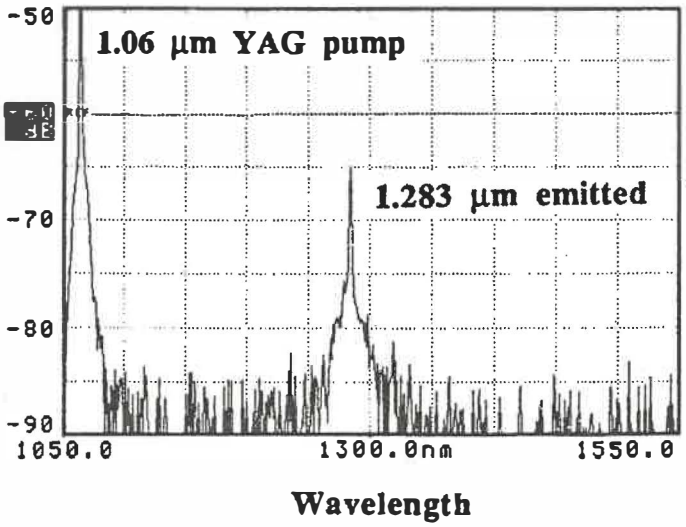

Fig.30 Spectrum of surface-emitting CG-DFB laser.

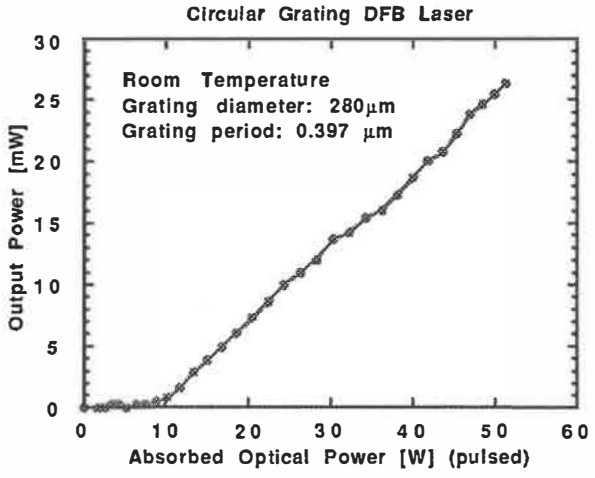

Fig.31 Surface-emitted power against pumping power.

CHAPTER 5

CIRCULAR GRATING DBR LASERS: FABRICATION AND MEASUREMENTS

5.1 Introduction

In the previous Chapter, we have demonstrated the first circular grating DFB laser by optical pumping. However, in practical applications, it is more desirable to have electrically-pumped lasers.

Since CG-DBR lasers have lower threshold current than CG-DFB lasers, and since it is easier to design the electrode for CG-DBR lasers than for CG-DFB lasers, we choose to study electrically-pumped CG-DBR lasers. In fact, we have fabricated and demonstrated the world's first CG-DBR laser.

This chapter is organized in the following way: we first give the design considerations for CG-DBR lasers in Section 5.2. Then, in Section 5.3, we describe the fabrication procedures of these lasers. The lasing characteristics of the first electrically-pumped CG-DBR lasers are presented in Section 5.4.

5.2. Design of CG-DBR Lasers

The structure of a circular grating distributed Bragg reflector (CG-DBR) laser is shown schematically in Fig.32, where the active medium is limited within a circle of radius R_1. The electrical pumping is realized by injection current from the contact in the center. The pumping region in the center is surrounded by circular grating lines. Without loss of generality, we assume that the circular grating has a rectangular profile. The period of the grating is denoted by Λ, the width of the grating valley is W_1, and the width of the grating ridge is W_2, with $\Lambda = W_1 + W_2$. The depth of the grating is denoted by Δh. The outer

radius of the grating is denoted by R_2. The length of the grating region is then equal to $L = R_2 - R_1$.

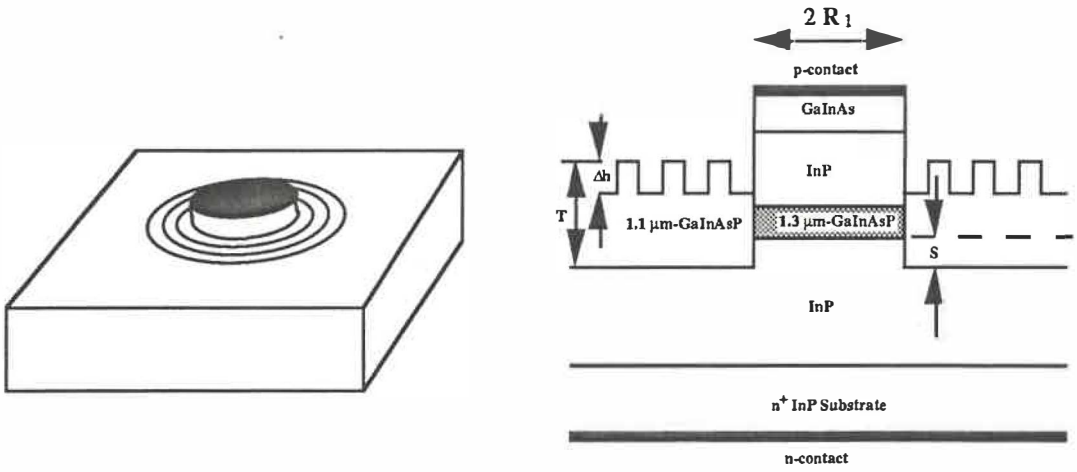

(a) schematic view (b) cross-section

Fig.32 Diagram of electrically-pumped circular grating (CG) DBR laser.

5.2.1. Threshold Condition of CG-DBR Lasers

Based on the large radius approximation of the coupled-wave theory in Chapter 2, we have obtained the following eigenvalue equation for the lasing modes in a circular grating DBR laser (see Eq.(3.35) in Chapter 3) :

$$\rho_0 \rho_{R_1} e^{-j2\Delta R_1} e^{2\alpha_1 R_1} = 1 \tag{5.1}$$

where ρ_0 and ρ_{R_1} are the field reflection coefficients of the center (r=0) and that of the grating seen from $r = R_1$ outward, respectively. Δ is the difference between the propagation constant of the pumping region and that of the grating region. α_1 is the mode loss (or gain) of a laser mode.

The finiteness of the optical field at r=0 implies $\rho_0 = 1$. This is equivalent to saying that the center is a mirror of 100% reflectivity. As shown in Chapter 3, for a circular grating of rectangular profile, we have

$$\rho_{R_1} = \frac{(-1)^n K_m e^{-j\Omega_m} e^{-j2\delta R_1} \sinh[\gamma(R_2 - R_1)]}{\gamma \cosh[\gamma(R_2 - R_1)] - (\alpha_2 - j\delta)\sinh[\gamma(R_2 - R_1)]} \tag{5.2a}$$

$$\gamma = \sqrt{K_m^2 + (\alpha_2 - j\delta)^2} \tag{5.2b}$$

$$\delta = \beta - \frac{\pi}{\Lambda} m \tag{5.2c}$$

$$\Omega_m = \frac{\pi}{\Lambda} m (W_1 + 2R_1) \tag{5.2d}$$

In Eqs.(5..2), n is an integer denoting the order of a cylindrical wave, m is the order of the grating, δ denotes the frequency deviation from the Bragg frequency of the grating, β is the propagation constant of the fundamental slab mode in the planar waveguide and K_m is the coupling coefficient between the inward-propagating wave and the outward-propagating wave due to the circular grating. Note that under the large radius approximation, as indicated by the expression for ρ_{R_1} in Eq.(5.2a), all the even order cylindrical waves (or all the odd order waves) have the same threshold.

Because the distributed Bragg reflector and the active region form two separate waveguides, transfer of the optical mode between them leads to coupling losses that reduce the effective reflectivity of the DBR. Therefore, the coupling losses between these two regions should be included in the design consideration of CG-DBR lasers.

Let C_0 denote the interface power coupling efficiency at r= R_1 defined by :

$$C_0 = \left| \int_{-\infty}^{\infty} Z_a Z_g \, dz \right|^2 \tag{5.3}$$

where Z_a and Z_g are the normalized electric field distributions along the z-direction in the gain region and the grating region, respectively. The coupling losses occur twice during each reflection, the effective reflection coefficient of the circular grating is thus given by

$$\rho_{eff} = \rho_{R_1} C_0 \tag{5.4}$$

The eigenvalue equation should be modified as :

$$C_0 \rho_0 \rho_{R_1} e^{-j2\Delta R_1} e^{2\alpha_1 R_1} = 1 \tag{5.5}$$

Comparing Eq.(5.5) with the eigenvalue equation for conventional DBR lasers [88], we see that in the case of CG-DBR lasers, the power coupling efficiency C_0 appears only once, while in conventional DBR lasers it is the square of C_0 that has to be used because there are two DBR sections. In practical terms, this means that in circular grating DBR lasers the coupling efficiency between the gain region and the grating region is less critical than in conventional ones.

5.2.2. Coupling Efficiency C_0 and Coupling Coefficient K_m

The power coupling efficiency C_0 and the coupling coefficient K_m are two very important parameters in the design of CG-DBR lasers. The imperfect coupling between the gain region and the grating region is equivalent to an additional loss α_0 given by

$$\alpha_0 = \frac{1}{2R_1} \ln\left(\frac{1}{C_0}\right) \tag{5.6}$$

Fig.33 shows the interface loss α_0 as a function of C_0 for different values of the inner radius R_1. It is seen that to obtain $\alpha_0 < 50\ cm^{-1}$, we require that $C_0 > 0.9$.

In Fig.34, the coupling efficiency C_0 is plotted as a function of the offset S between the active layer and the guiding layer in the grating region. The thickness of the active layer is d=0.17 μm. The thickness of the guiding layer is set to be T = 0.6 μm. Also given in the inset of the figure are the coupling coefficients of second-order grating with $W_1/\Lambda = 1/4$ for different grating depth Δh.

In Fig.35, the power coupling efficiency is plotted against the etching depth of the grating, for S=0.0μm, T = 0.6 μm and d = 0.17 μm.

The coupling coefficient depends strongly on the etching depth of the grating. This is shown in Fig.36.

The grating aspect ratio W_1/Λ also plays an important role in determining the power coupling efficiency and the coupling coefficient, thus affecting the threshold current of CG-DBR lasers. Fig.37 shows the power coupling efficiency C_0 as a function of W_1/Λ. Fig.38 shows the coupling coefficient against W_1/Λ. It is seen that for second-order grating, the coupling coefficient reaches its maximum around W_1/Λ =0.25.

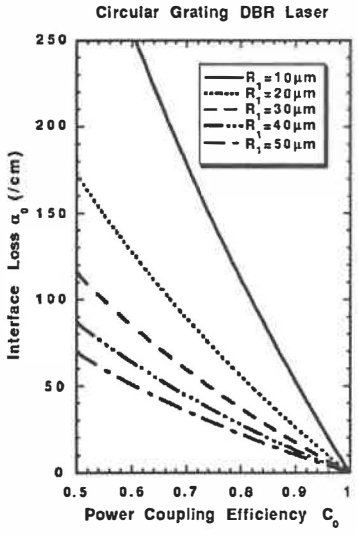

Fig.33 Interface loss as a function of the power coupling efficiency .

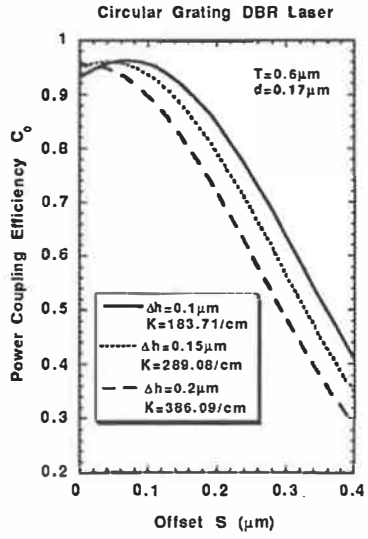

Fig.34 Power coupling efficiency as a function of the offset .

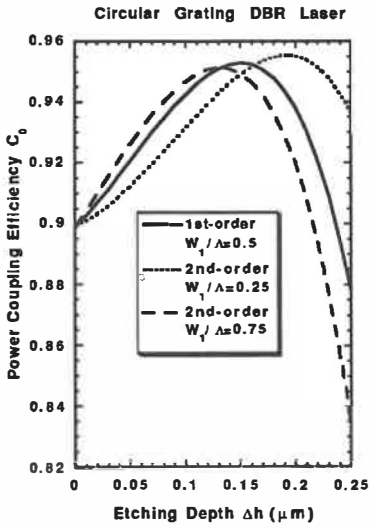

Fig.35 Power coupling efficiency as a function of the etching depth.

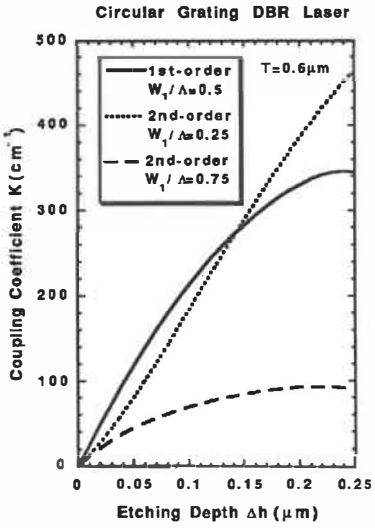

Fig.36 Coupling coefficient versus the etching depth.

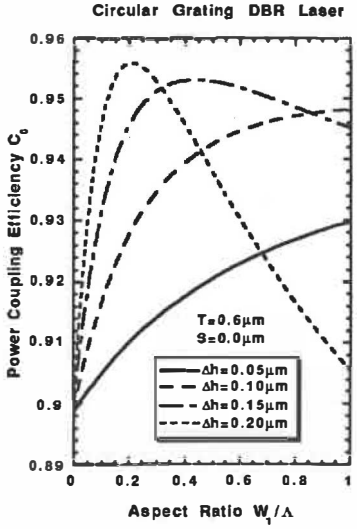

Fig.37 Power coupling efficiency as a function of the grating aspect ratio W_1/Λ.

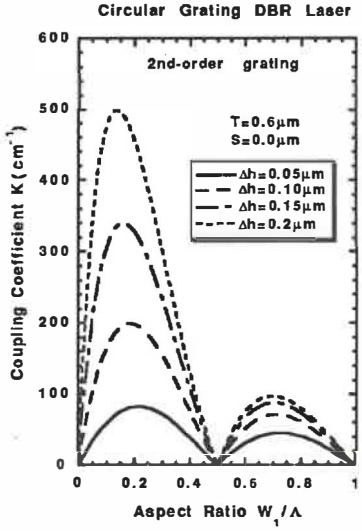

Fig.38 Coupling coefficient as a function of the grating aspect ratio W_1/Λ.

5.2.3. Threshold Current of CG-DBR Lasers

Once the power coupling efficiency and the coupling coefficient are determined, one can calculate the threshold modal gain from Eq.(5.5). The threshold current density of a CG-DBR laser is then estimated by (see Chapter 3 and [89]) :

$$J_{th} = e\,(d_a/\eta_i)\,B_{eff}\,[\,N_0 + (2\,\alpha_{th} + \alpha_{int})/(A_0\Gamma)\,]^2 \qquad (5.7)$$

where A_0 is the gain coefficient, N_0 is the carrier density to achieve transparency (corresponding to the onset of population inversion), e is the electron charge, d_a is the thickness of the active layer, η_i is the internal quantum efficiency, B_{eff} is the effective recombination constant, Γ is the optical confinement factor of the active layer. α_{th} is the mode gain calculated from Eq.(5.5) and α_{int} is the total internal loss.

The threshold current I_{th} is then calculated from :

$$I_{th} = \pi\,(R_1)^2\,J_{th} \qquad (5.8)$$

In our calculation, the following parameters are used in estimating the threshold current of a CG-DBR laser fabricated on InGaAsP/InP heterostructure: $A_0=2.5\times10^{-16}$ cm^2, $N_0=1.5\times10^{18}$ cm^{-3}, $B_{eff} = 1.0\times10^{-10}$ cm^{3}s^{-1} [89], $d_a = 0.17$ μm, $\eta_i = 1$ and $\alpha_{int} = 50$ cm^{-1}.

Fig.39 shows the threshold current density as a function of the pumping region radius R_1. The length of the grating region is $L=R_2-R_1=140\mu$m. The phase-shift Ω is chosen to be $\Omega=2\pi$ The coupling coefficient is assumed to be K=100/cm. The threshold current of the same DBR laser is shown in Fig.40. The power coupling efficiency is assumed to C_0 =0.8, 0.9, 0.95 and 1.0.

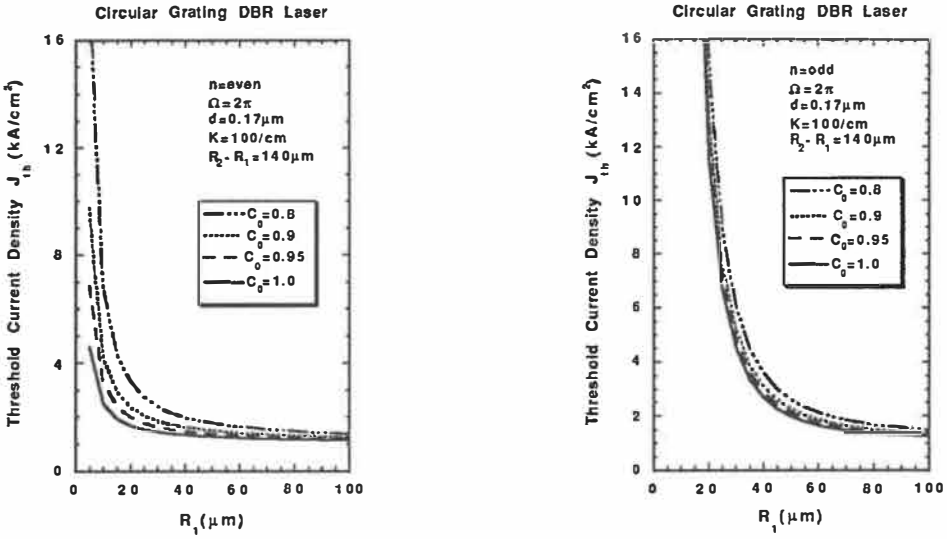

(a) n=even (b) n=odd

Fig.39 Threshold current density versus gain region radius.

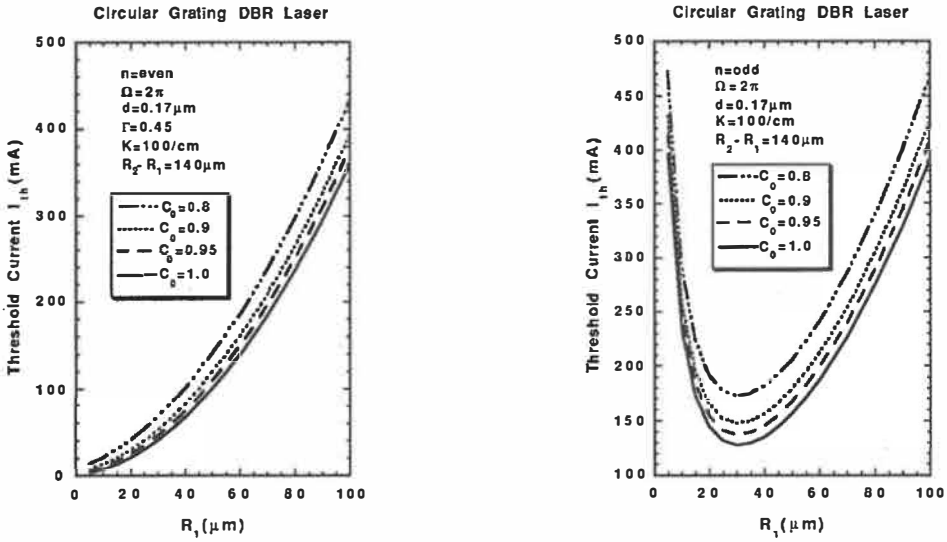

(a) n=even (b) n=odd

Fig.40 Threshold current versus gain region radius.

5.3. Fabrication of CG-DBR Lasers

CG-DBR lasers are fabricated by focused-ion beam (FIB) lithography and reactive-ion etch (RIE) techniques. The fabrication procedures are outlined in Fig.41.

First, a conventional double heterostructure GaInAsP/InP laser is grown by the metal-organic-chemical-vapor-deposition (MOCVD) method. The active layer (GaInAsP, λ_g =1.3μm) has a thickness of 0.17 μm. Then, circular mesas are etched by RIE to a depth just past the active layer. A 0.6 μm thick epilayer of semi-insulating Fe-doped GaInAsP (λ_g =1.1 μm) is then selectively regrown around the circular mesas by MOCVD [91]. Fabrication of the bottom n-contact and circular top p-contact follows the epitaxial regrowth. Finally, circular gratings are patterned by FIB lithography and transferred down to the guiding layer by RIE. The second-order grating is designed to have a period of 0.401μm , an aspect ratio of W_1/Λ = 0.25. Fig.42 shows a photograph of a fabricated second-order DBR laser. Fig.43 is a SEM photomicrograph of the circular grating. Fig.44 is the same CG-DBR laser at a higher magnification. The cross-section of the circular grating region is shown in Fig.45. The etching depth of the grating was around 0.15 μm.

5.4 Optical Characteristics of CG-DBR Lasers

The fabricated CG-DBR lasers have been tested at room temperature under pulsed condition (pulse width τ =100ns and pulse period T = 10 μs). Figs.46(a)-(d) show the surface-emitted power against the injected current (L-I curve) for CG-DBR lasers with R_1 =25, 30, 35 and 40 μm, respectively. The maximum output power reaches 10mW for the device with R_1=35μm whose threshold current is 170 mA. Examples of the lasing spectra are presented in Figs.47(a)-(b). The lasing wavelength ($\lambda \sim$ 1.306μm) is slightly longer than the designed Bragg wavelength (λ_b=1.3μm), i.e., the lasing frequency is lower than the Bragg frequency determined by the grating. Fig.48 shows the near field patterns of the surface-emitting CG-DBR lasers just above the threshold. The triangular-shaped dark sector is the probe needle used for current injection. The near field for the device with R_1=30μm is not shown because it was damaged during the measurement. Fig.49 gives the near field pattern of the same CG-DBR lasers at about twice the threshold current. It is observed that at low injection level, the devices with R_1=35μm and R_1=40μm give a dumb-

bell shaped near field, which implies that the laser oscillation is in the odd (n=1) rather than the even (n=0) cylindrical waves. For the case of R_1=25μm, the near field has four bright spots, as shown in Fig.48(a). It seems to indicate that this laser operates in the even (n=2) cylindrical wave. At high injection level, the emitted beam becomes circular, especially for for the laser with R_1= 35μm, as seen in Fig.49(b). This behavior is probably due to the multi-mode operation, particularly when the threshold of the even waves is just slightly higher than the odd waves.

The measured threshold currents of the first CG-DBR lasers are appreciably higher than predicted by theory. For an etching depth of Δh=0.15μm and an aspect ratio of W_1/Λ=0.25, the calculated coupling coefficient is K=289/cm (see Fig.38) and the calculated power coupling efficiency is C_0=0.95. For even-wave (n=0, $\Omega=2\pi$) or odd-wave (n=1, $\Omega=\pi$) operation, this would give a threshold current of I_{th}= 34 mA for R_1=30μm, as compared to the measured threshold current of 140 mA.

It should be noted that the cavity and the radiation losses have not been included in the theoretical calculations. The discrepancy between the theoretical values and the measured results may also be due to nonuniformity of the crystal regrowth, eccentricity of the circular gratings with respect to the center of the circular mesa (about 2μm for the devices presented here) and irregularities which cause additional scattering losses. Eccentricity does play an important role in determining the lasing characteristics of CG-DBR lasers. In fact, when the circular gratings were about 20μm off the center, no lasing was observed.

5.5. Summary

We have discussed the design and fabrication of electrically-pumped circular grating(CG) DBR lasers. Moreover, we have successfully fabricated electrically-pumped surface-emitting CG-DBR lasers which lase at room temperature under pulsed condition. To our best knowledge, this is the first demonstration of surface-emitting CG-DBR laser.

Step 1: Growth of double hetero-structure

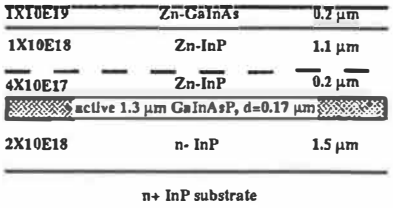

Step 2: Circular mesa by RIE

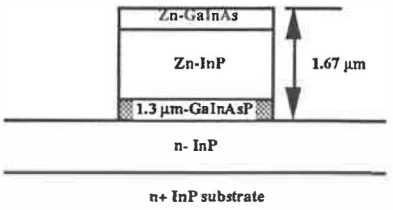

Step 3: Regrowth of semi-insulating 1.1μm GaInAsP epilayer

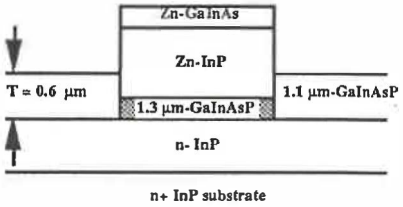

Step 4: Ohmic contact

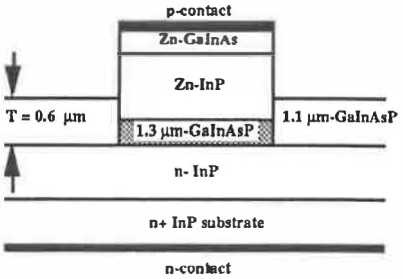

Step 5: Circular grating by FIB and RIE

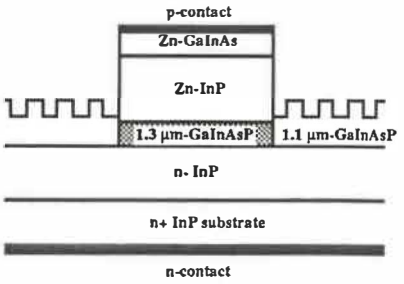

Fig.41 Fabrication procedures of electrically-pumped CG-DBR laser

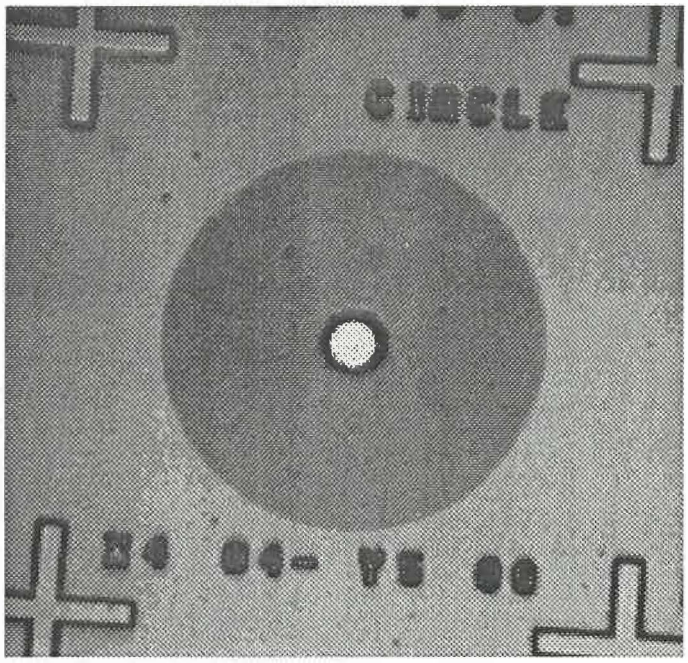

Fig.42 Photograph of a fabricated second-order surface-emitting CG-DBR laser.

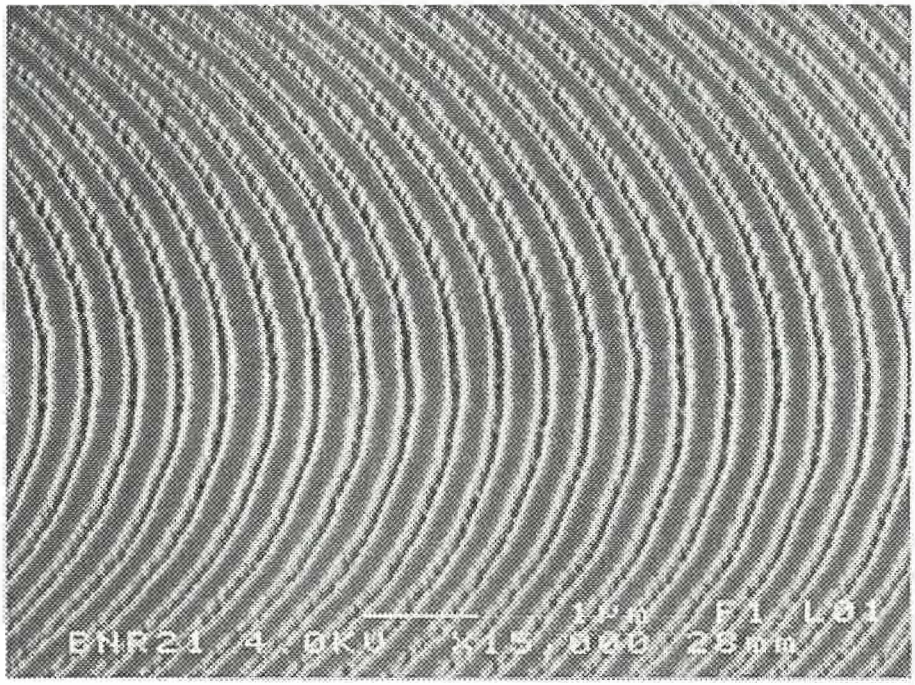

Fig.43 SEM photograph of second-order CG-DBR laser (grating region, X 15,000).

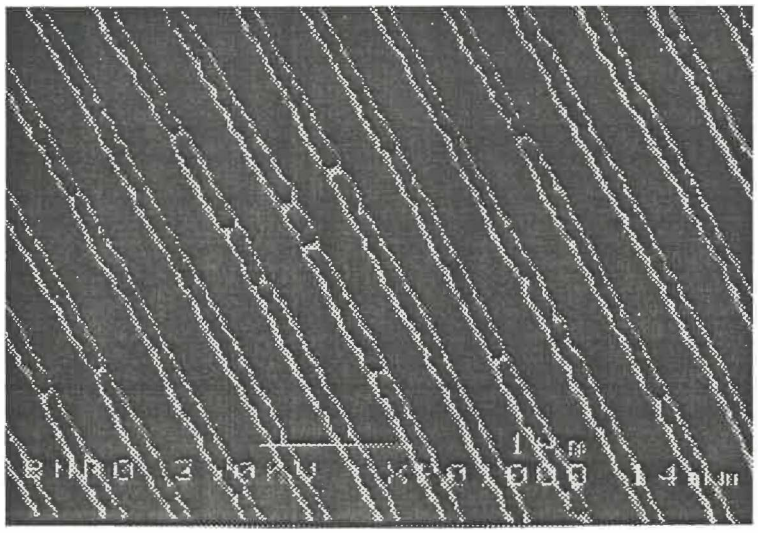

Fig.44 SEM photograph of second-order CG-DBR laser (grating region, X 20,000)

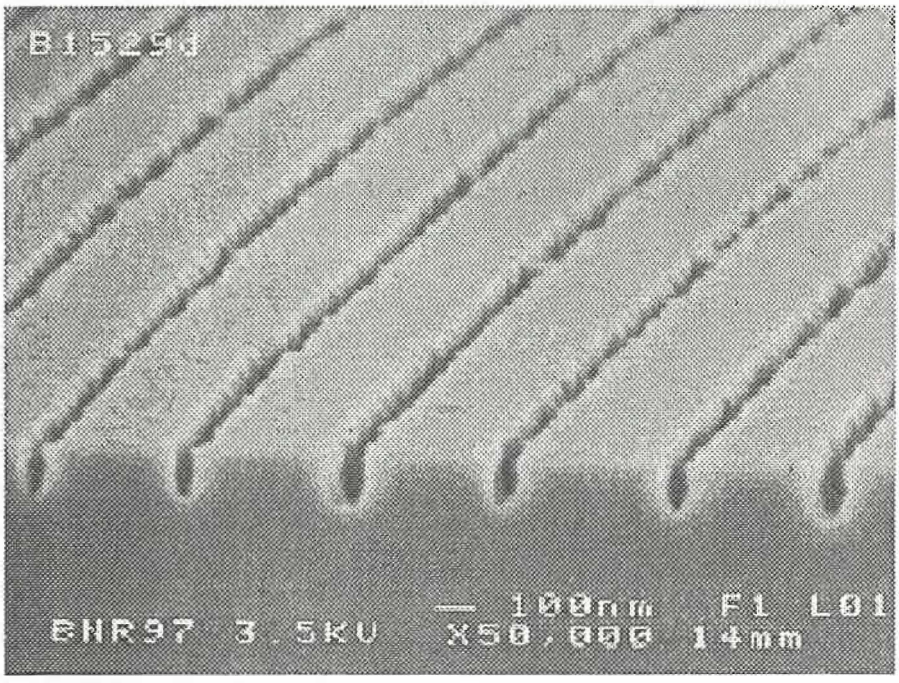

Fig.45 Cross-section of CG-DBR laser (grating region)

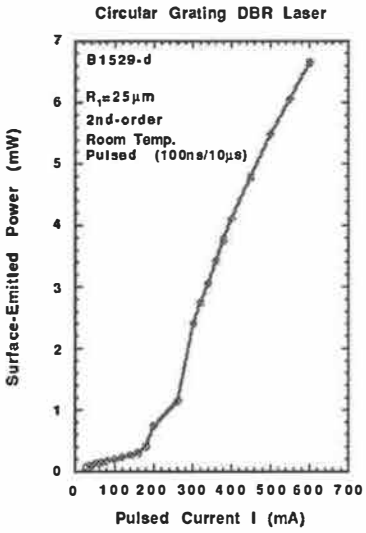

(a) $R_1 = 25\ \mu m$

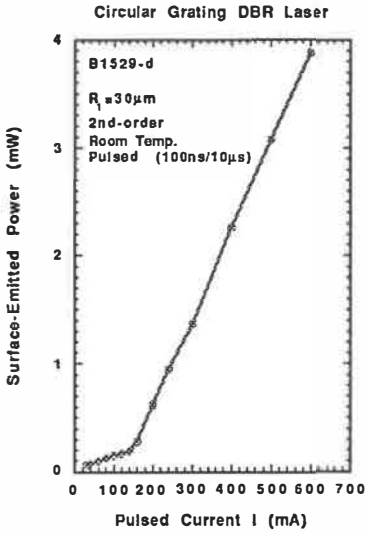

(b) $R_1 = 30\ \mu m$

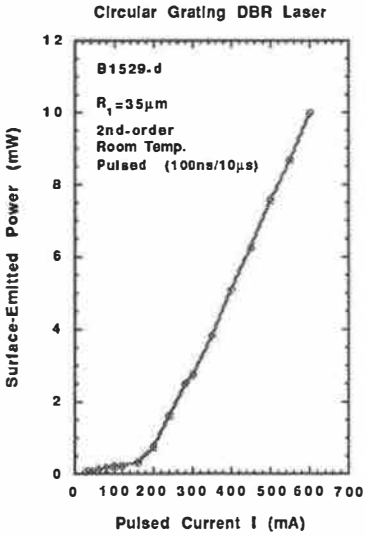

(c) $R_1 = 35\ \mu m$

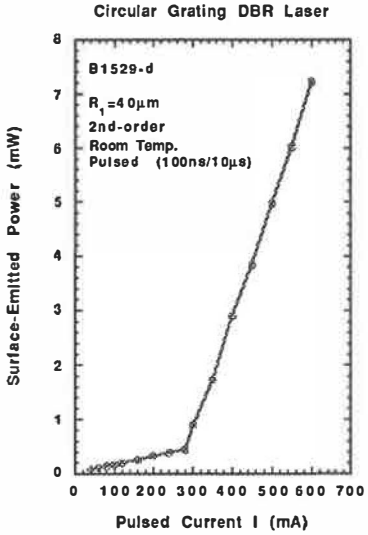

(d) $R_1 = 40\ \mu m$

Fig.46 Surface-emitted power versus injected current (L-I curve) of CG-DBR lasers.

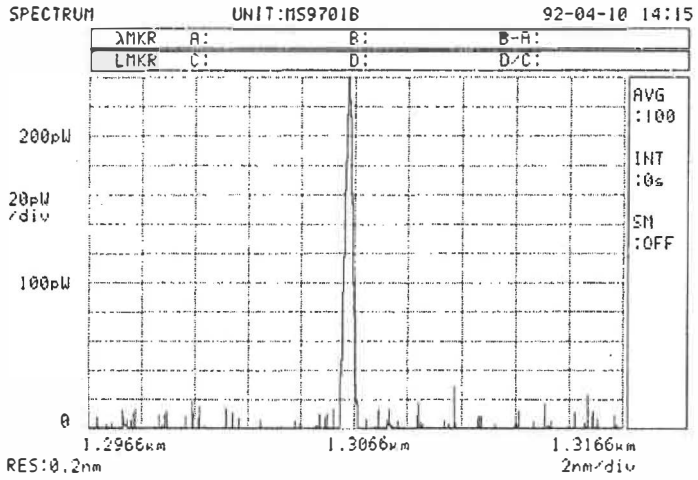

(a) R_1= 25μm, I= 230 mA (pulsed)

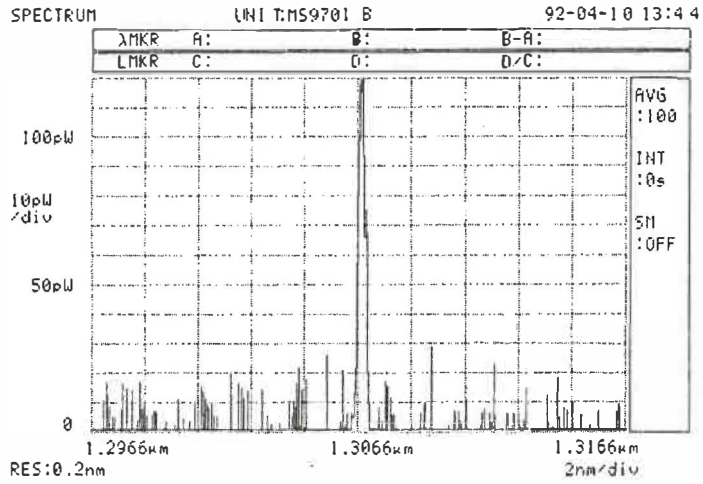

(b) R_1 = 40 μm, I = 300 mA (pulsed)

Fig.47 Examples of lasing spectrum of CG-DBR lasers at room temperature under pulsed conditions (100ns/10μs).

(a) R_1=25μm, I=200mA
I_{th} = 160mA

(b) R_1=35μm, I=200mA
I_{th} = 170mA

(c) R_1=40μm, I=300mA
I_{th} = 260mA

Fig.48 Near field of surface-emitting CG-DBR lasers just above threshold.

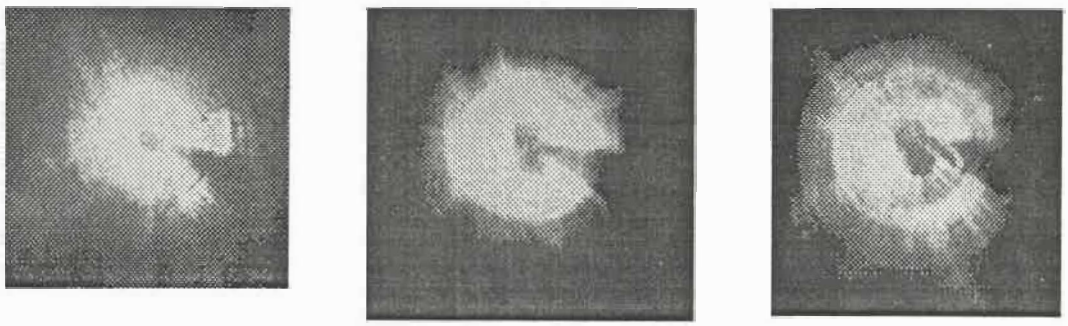

(a) R_1=25μm, I=400mA
I_{th} = 160mA

(b) R_1=35μm, I=400mA
I_{th} = 170mA

(c) R_1=40μm, I=500mA
I_{th} = 260mA

Fig.49 Near field of surface-emitting CG-DBR lasers at high injection level ($I \sim 2I_{th}$).

CONCLUSIONS

In this thesis, both theoretical and experimental studies have been made on the circular grating distributed feedback (CG-DFB) laser and the circular distributed Bragg reflector (CG-DBR) laser. The operation of the first surface-emitting CG-DFB and CG-DBR lasers have been successfully demonstrated by optical pumping and by current injection, respectively.

In Chapter 1, a new coupled-wave theory for cylindrical waves in circular grating planar waveguide is established. The theory is a general, self-consistent, vector-wave formulation based on Maxwell's equations. The coupled-wave equations are valid for both passive and active circular grating devices in integrated optics. It is shown that only cylindrical waves of the same order are coupled. These cylindrical waves can belong to different slab modes in the waveguide. For zeroth-order waves, pure TE-TE (TM-TM) couplings occur. For higher order waves, the TE- and the TM-cylindrical waves are cross-coupled. The coupled-wave equations for zeroth-order cylindrical waves are similar to those of two-mode coupling in one dimensional waveguides with straight gratings.

In Chapter 2, a simplified form of the coupled-wave equations is derived for cylindrical waves in circular grating planar waveguides. Under the large radius approximation ($\beta r >> 1$), the coupling between TE and TM cylindrical waves can be neglected. This renders the coupled-wave equations separable into two sets, one for TE cylindrical waves and the other for TM cylindrical waves. The large radius approximation is valid for most practical cases. The difference between our theory and the scalar theory of other researchers is clarified.

In Chapter 3, a detailed threshold analysis for TE-cylindrical waves in CG-DFB and CG-DBR lasers is presented. The analysis is based on the coupled-wave theory developed in Chapter 1 and 2. Numerical results show that by proper choice of the total phase-shift Ω (in other words, the inner radius R_1), the laser can be tuned to oscillate in either the even waves or the odd waves. This is an important result for the design of practical CG-DFB and CG-DBR lasers. It is also shown that CG-DFB lasers normally have a higher threshold current density and a higher threshold current than CG-DBR lasers.

In Chapter 4, experimental results of the first CG-DFB laser on a GaInAsP/InP double heterostructure were presented. The circular grating was fabricated by electron-beam (E-beam) lithography and reative-ion-etching (RIE). Second-order circular grating was

used to achieve surface-emission. Lasing action in the first surface-emitting CG-DFB laser was demonstrated at room temperature by optical pumping with a mode-locked, Q-switched, YAG laser. The observed lasing wavelength was 1.283μm. The peak threshold pumping power density was estimated to be 16.2kW/cm^2. The pulsed peak output power was more than 25mW.

In Chapter 5, the first electrically-pumped CG-DBR lasers were designed and fabricated on a GaInAsP/InP heterostructure. The CG-DBR lasers operated at room temperature under pulsed condition. The lowest threshold current was 140mA and the maximum optical power emitted from the surface exceeded 10mW. The lasing action was observed to be in the odd cylindrical-wave modes (with dumb-bell shaped radiation pattern). The trend of the measured threshold current as a function of the gain region radius agreed in general with the theoretical prediction. However, due to imperfections in crystal regrowth and the coupling loss encountered at the gain/grating interface, the threshold current of the CG-DBR lasers were higher than theoretical values.

There is still much work to do before circular grating lasers can be made truly practical. For example, these lasers have to be optimized in terms of the threshold current density, the threshold current to achieve continuous-wave (CW) operation at room temperature. Two important aspects --- the radiation efficiency (surface-emitted power) and the radiation pattern --- have not been studied yet. It would be of interest to see if operation in even cylindrical waves could give a circularly symmetric output beam. The dynamic characteristics and the spectral properties must also be investigated.

The theoretical and experimental studies in this thesis were conducted on bulk GaInAsP quaternary materials. Another area to be studied is circular grating lasers using quantum-well structures. Single-quantum-well (SQW) and multiple-quantum-well (MQW) DFB and DBR lasers are reported to have lower threshold and higher output power than their bulk counter-parts [59-60, 92-95].

There could also be improvement in fabrication techniques. Presently, the circular gratings are patterned by E-beam or FIB lithography, both are time-consuming and expensive techniques. It would be a great help toward production if other methods such as holographic patterning were made available.

The successful demonstration of both CG-DFB and CG-DBR lasers makes the concept proposed by Shimpe [61] a reality. These lasers are promising light sources for future optical communication systems, optical interconnections, and other free space applications.

REFERENCES

[1] KOGELNIK, H. and SHANK, C.V., " Stimulated emission in a periodic structure, "*Appl.Phys.Lett.*, vol.18, no.4, pp.152-154, 1971.

[2] KOGELNIK, H. and SHANK, C.V., " Coupled-wave theory of dsitributed feedback lasers, " *J. Appl. Phys.*, vol.43, pp.2327-2335, 1972.

[3] NAKAMURA, M., YARIV, A., YEN, H.W. and SOMEKH, S., " Optically pumped GaAs surface laser with corrugation feedback, " *Appl. Phys. Lett.*, vol 22, no.10, pp.515-516, 1973.

[4] CHINN, S. R., " Effects of mirror reflectivity in a distributed feedback laser, " *IEEE J. Quantum Electron.*, vol.QE-9, no.6, pp.574-580, 1973.

[5] SHUBERT, R., " Theory of optical-waveguide distributed lasers with nonuniform gain and coupling, " *J. Appl. Phys.*, vol.45, no.1, pp.209-215, 1974.

[6] WANG, S., CORDERO, R. F. and TSENG, C. C., " Analysis of distributed-feedback and distributed-Bragg-reflector laser structures by method of multiple reflections, " *J. Appl. Phys.*, vol.45, no.9, pp.3975-3977, 1974.

[7] WANG, S, " Principles of distributed feedback and distributed Bragg-reflector lasers, " *IEEE J. Quantum Electron.*, vol.QE-10, pp.413-427, 1974.

[6] STREIFER, W., SCIFRES, D.R. and BURNHAM, R. D., " Coupling coefficients for distributed feedback single and double heterostructure diode lasers, " *IEEE J. Quantum Electron.*, vol.QE-11, pp.867-873, 1975.

[7] STREIFER, W., SCIFRES, D.R. and BURNHAM, R. D., " Analysis of grating-coupled radiation in GaAs:GaAlAs lasers and waveguides, " *IEEE J. Quantum Electron.*, vol.QE-12, no.7, pp.422-428, 1975.

[8] TSANG, W. T. and WANG, S., " GaAs-Ga1-xAlxAs double-heterostructure injection lasers with distributed Bragg reflectors, " *Appl. Phys. Lett.*, vol.28, no.10, pp. 596-598, 1976.

[9] YARIV, A. and NAKAMURA, M., " Periodic structures for integrated optics, " *IEEE J. Quantum Electron.*, vol.QE-13, no.4, pp.233-253, 1977.

[10] YAMAMOTO, Y., KAMIYA, T. and YANAI, H., " Improved coupled mode analysis of corrugated waveguides and lasers, " *IEEE J. Quantum Electron.*, vol.QE-14, no.4, pp.245-258, 1978.

[11] SUZUKI, A. and TADA, K., " Theory and experiment on distributed feedback lasers with chirped grating, " *SPIE vol.239, Guided-Wave Optical and Surface Acoustic Wave Devices, Systems and Applications*, , pp.10-18, 1980.

[12] KITAMURA, M., SEKI, M., YAMAGUCHI, M., MITO, I., KOBAYASHI, Ke. and KOBAYASHI, Ko., " High-power single-longitudinal-mode operation of 1.3 μm DFB-DC-PBH LD, " *Electron. Lett.*, vol.19, no.20, pp.840-841, 1983.

[13] OKUDA, H. HIRAYAMA, Y., KINOSHITA, J., FURUYAMA, H. and UEMATSU, Y., " High-quality 1.3 μm GaInAsP/InP BH-DFB lasers with first order gratings, " *Electron. Lett.*, vol.19, no.22, pp.941- 943, 1983.

[14] KOYAMA, F., SUEMATSU, Y., ARAI, S. and TAWEE, T., " 1.5-1.6μm GaInAsP/InP dynamic-single-mode (DSM) lasers with distributed Bragg reflector, " *IEEE J. Quantum Electron.*, vol.QE-19, no.6, pp.1042-1051, 1983.

[15] BLONDEAU, R., RAZEGHI, M., KRAKOWSKI, M., VILAIN, G., DE CREMOUX, B. and DUCHEMIN, J. P., " CW operation of GaInAsP buried ridge structure laser at 1.5 μm grwon by LP-MOCVD, " *Electron. Lett.*, vol.20, no.21, pp.850-851, 1984.

[16] SUZUKI, Y., NAGAI, H., NOGUCHI, Y., MATSUOKA, T. and KURUMADA, K., " High-power SLM operation of 1.3μm InP/InGaAsP DFB LD with doubly buried heterostructure on p-type InP substrate, " *Electron. Lett.*, vol.20, no.21, pp.881-882, 1983.

[17] ITAYA, Y., MATSUOKA, T., KUROIWA, K. and IKEGAMI, T., " Longitudinal mode behaviors of 1.5μm range GaInAsP/InP distributed feedback lasers, " *IEEE J. Quantum Electron.*, vol.QE-20, no.3, pp.230-235, 1984.

[18] UTAKA, K., AKIBA, S., SAKAI, K. and MATSUSHIMA, Y., " Effect of mirror facets on lasing characteristics of distributed feedback InGaAsP/InP laser diodes at 1.5μm range, " *IEEE J. Quantum Electron.*, vol.QE-20, no.3, pp.236-245, 1984.

[19] AGRAWAL, G. P., " Line narrowing in a single-mode injection laser due to external optical feedback, " *IEEE J. Quantum Electron.*, vol.QE-20, no.5, pp.468-471, 1984.

[20] EDA, N., FURUYA, K. , KOYAMA, F. and SUEMATSU, Y. , " Axial mode selectivity in active distributed-reflector for dynamic-single-mode lasers, " J. Lightwave Technol.,vol.LT-3, no.2, pp.400-407, 1985.

[21] KAZARINOV, R. F. and HENRY, C. H., " Second-order distributed feedback lasers with mode selection provided by first-order radiation losses, " *IEEE J. Quantum Electron.*, vol.QE-21, no.2, pp.144-150, 1985.

[22] KAZARINOV, R. F. and HENRY, C. H., " Observation of destructive interference in the radiation loss of second-order distributed feedback lasers, " *IEEE J. Quantum Electron.*, vol.QE-21, no.2, pp.151-153, 1985.

[23] AGRAWAL, G. P. and DUTTA, N. K., " Analysis of ridge-waveguide distributed feedback lasers, " *IEEE J. Quantum Electron.*, vol.QE-21, no.6, pp.534-538, 1985.

[24] McCALL, S. L. and PLATZMAN, P. M., " An optimized $\pi/2$ distributed feedback laser, " *IEEE J. Quantum Electron.*, vol.QE-21, no.12, pp.1899-1904, 1985.

[25] UTAKA, K., AKIBA, S., SAKAI, K. and MATSUSHIMA, Y., " λ/4-shifted InGaAsP/InP DFB lasers, " *IEEE J. Quantum Electron.*, vol.QE-22, no.7, pp.1042-1051, 1986.

[26] FAVRE, F., " Theoretical analysis of external optical feedback on DFB semiconductor lasers, " *IEEE J. Quantum Electron.*, vol.QE-23, no.1, pp.81-88, 1987.

[27] HONDA, K., HIRATA, S., OHATA, T., HORII, S. and KOJIMA, C., " Low threshold current AlGaAs/GaAs rib-waveguide separate-confinement-heterostrucutre distributed-feedback lasers grown by metalorganic chemical vapor deposition, " *IEEE J. Quantum Electron.*, vol.QE-23, no.6, pp.144-150, 1987.

[28] SODA, H., KOTAKI, Y., SUDO, H., ISHIKAWA, H., YAMAKOSHI, S. and IMAI, H., " Stability in longitudinal mode operation in GaInAsP/InP phase-adjusted DFB lasers, " *IEEE J. Quantum Electron.*, vol.QE-23, no.6, pp.804-814, 1987.

[29] OISHI, M., NAKAO, M., ITAYA, Y., SATO, K. and IMAMURA, Y., " MOVPE-grown 1.5μm distributed feedback lasers on corrugated InP substrates, " *IEEE J. Quantum Electron.*, vol.QE-23, no.6, pp.822-827, 1987.

[30] COLDREN, L.A. and CORZINE, S. W., " Continuously-tunable single-frequency semiconductor lasers, " *IEEE J. Quantum Electron.*, vol.QE-23, no.6, pp.903-908, 1987.

[31] TROMBORG, B., GLESEN, H., PAN, X. and SAITO, S., " Transmission line description of optical feedback and injection locking for Fabry-Perot and DFB lasers, " *IEEE J. Quantum Electron.*, vol.QE-23, no.11, pp.1875-1989, 1987.

[32] KOJIMA, K., NODA, S., MITSUNAGA, K., KYUMA, K. and HAMANAKA, K., " Continuous wave operation of a surface-emitting AlGaAs/GaAs multiquantum well distributed Bragg reflector laser, " *Appl. Phys. Lett.*, vol.50, no.24, pp. 1705-1707, 1987.

[33] MAKINO, T. and GLINSKI, J., " Effects of radiation loss on the performance of second-order DFB semiconductor lasers, " *IEEE J. Quantum Electron.*, vol.QE-24, no.1, pp.73-82, 1988.

[34] MAKINO, T. and GLINSKI, J., " Transfer matrix analysis of the amplified spontaneous emission of DFB semiconductor laser amplifiers, " *IEEE J. Quantum Electron.*, vol.QE-24, no.8, pp.1507-1518, 1988.

[35] PALFREY, S.L., HAMMER, J.M., LONGEWAY, P.A., CARLSON, N.W., EVANS, G.A., ANDREWS, J.T., JAKLIK, J., KIRK, J.B., STOLZENBERGER, R. and TRIANDO, A.R., " Phase-locked operation of a three-element InGaAsP/InP grating-surface-emitting diode laser array, " *Appl. Phys. Lett.*, vol.54, no.14, pp. 1296-1298, 1989.

[36] NAKANO, Y., LUO, Y. and TADA, K., " Facet reflection independent, single longitudinal mode oscillation in a GaAlAs/GaAs distributed feedback laser equipped with a gain-coupling mechanism, " *Appl. Phys. Lett.*, vol.55, no.16, pp. 1606-1608, 1989.

[37] KOMORI, K., ARAI, S., SUEMATSU, Y., ARIMA, I. and AOKI, M., " Single-mode properties of distributed-reflector laser, " *IEEE J. Quantum Electron.*, vol.QE-25, no.6, pp.1235-1244, 1989.

[38] EVANS, G. A., CARLSON, N.W., HAMMER, J.M., LURIE, M., BUTLER, J. K., PALFREY, S.L., AMANTEA, R., CARR, L.A., HAWRYLO, F.Z., JAMES, E.A., KAISER, C.J., KIRK, J. B. and REICHERT, W.F., " Two-dimensional coherent laser arrays using grating surface emission, " *IEEE J. Quantum Electron.*, vol.QE-25, no.6, pp.1525-1538, 1989.

[39] CARLSON, N.W., EVANS, G.A., BOUR, D.P. and LIEW, S.K., " Demonstration of a grating-surface-emitting diode laser with low-threshold current density, " *Appl. Phys. Lett.*, vol.56, no.1, pp. 16-18, 1989.

[40] MAKINO, T., " Analysis of the spontaneous emission rate of multiple-phase-shifted distributed feedback semiconductor lasers, " *Electron. Lett.*, vol.26, no.10, pp.629-631, 1990.

[41] HORI, Y. and SATO, H., " Analysis of distributed feedback semiconductor lsaers by two-dimensional theory, " *IEEE J. Quantum Electron.*, vol.QE-26, no.4, pp.655-662, 1990.

[42] VANKWIKELBERG, P., MORTHIER, G. and BAETS, R., " CLADISS - a longitudinal multimode model for the analysis of the static, dynamic and stochastic behavior of diode lasers with distributed feedback, " *IEEE J. Quantum Electron.*, vol.QE-26, no.10, pp.1728-1741, 1990.

[43] MATSUYAMA, T., MAKUTA, A., TANAKA, A., OHTRUKA, K., AGATSUMA, H. and KINOSHITA, J., " TM mode suppression property of DFB lasers with a narrow stripe region, " *IEEE Photon.Technol. lett.,* vol.2, no.9, pp.612-613, 1990.

[44] LUO, Y., NAKANO, Y. and TADA, K., " Purely gain-coupled distributed feedback semiconductor lasers, " *Appl. Phys. Lett.*, vol.56, no.17, pp. 1620-1622, 1991.

[45] MORTHIER, G. and BAETS, R., " Design of index-coupled DFB lasers with reduced longitudinal spatial hole burning, " *J. Lightwave Technol.*, vol.9, no.10, pp.1305-1313, 1991.

[46] ROZZI, T. , CHIARALUCE, F. and LANARI, M., " A rigorous analysis of DFB lasers with large and aperiodic corrugations, " *IEEE J. Quantum Electron.*, vol.QE-27, no.2, pp.212-223, 1991.

[47] MAKINO, T., " Transfer-matrix formulation of spontaneous emission noise of DFB semiconductor lasers, " *J. Lightwave Technol.,* vol.9, no.1, pp.84-91, 1991.

[48] MAKINO, T., " Analysis of surface-emitting λ/4-shifted DFB lasers with a distributed Bragg reflector, " *IEEE Photon.Technol. lett.,* vol.3, no.1, pp.12-14, 1991.

[49] CHIEN, M., KOREN, U., KOCH, T.L., MILLER, B.I., ORON, M., YOUNG, M. G. and DEMIGUEL, J. L., " Short-cavity distributed Bragg reflector laser with an integrated tapered output waveguide, " *IEEE Photon.Technol. lett.,* vol.3, no.5, pp.418-420, 1991.

[50] DAVID, K., BUUS, J., MORTHIER, G. and BAETS, R., " Coupling coefficients in gain-coupled DFB lasers: inherent compromise between coupling strength and loss, " *IEEE Photon.Technol. lett.,* vol.3, no.5, pp.439-441, 1991.

[51] HORI, Y. and SATO, H., " Analysis of TE and TM modes in DFB lasers by two-dimensional theory, " *IEEE J. Quantum Electron.*, vol.QE-27, no.7, pp.1874-1885, 1991.

[52] MAKINO, T., " Transfer-matrix analysis of the intensisty and phase noise of multi-section DFB semiconductor lasers, " *IEEE J. Quantum Electron.,* vol.QE-27, no.11, pp.2404-2414, 1991.

[53] TAKIGAWA, S., BACHER, K., AROSON, L.B. and HARRIS, J. S., Jr., " Low threshold current grating-coupled surface-emitting strained-InGaAs single quantum well laser with GaAs optical confinement structure, " *Appl. Phys. Lett.*, vol.60, no.3, pp. 265- 267, 1992.

[54] DAVID, K., BUUS, J. and BAETS, R., " Basic analysis of AR-coated, partly gain--couppled DFB lasers, the standing wave effect, " *IEEE J. Quantum Electron.*, vol.QE-28, no.2, pp.427-433, 1992.

[55] MAKINO, T., " Effective-index matrix analysis of distributed feedback semiconductor lasers, " *IEEE J. Quantum Electron.*, vol.QE-28, no.2, pp.434-440, 1992.

[56] SUEMATSU, Y., ARAI, S. and KISHIMO, K., " Dynamic single-mode semiconductor lasers with a distributed reflector, " *IEEE J. Lightwave Technol.*, vol.LT-1, No.1, pp.161-176, 1983; also see Y. Suematsu, " Progress in integrated optics lasers, " Integrated Optics, *Proc.of the 3rd European Conf., ECIO'85*, Berlin, Germany, editors H.-P Nolting and R. Ulrich, May 6-8, 1985.

[57] ALFEROV, Zh. I., ANDREYEV, V. M., GUREVICH, S. A., KAZARINOV, R. F., LARIONOV, V. R., MIZEROV, M.N. and PORTNOY, E.L.," Semicondutor lasers with the light output through the diffraction grating on the surface of the waveguide layer, " *IEEE J. Quantum Electron.,* vol.QE-11, no.7, pp.449-451, July 1975.

[58] MACOMBER, S.H., MOTT, J.S., NOLL, R.J., GALLATIN, G.M., E.J. GRATRIX, and O'DWYER, S.L., " Surface-emitting distributed feedback semiconductor laser, " *Appl. Phys. Lett.*, vol.51, no.7, pp.472-474, 1987.

[59] WELCH, D. F., PARKE, R., HARDY, A., STREIFER, W. and SCIFRES, D. R. , " Low-threshold grating-coupled surface-emitting lasers, " *Appl. Phys. Lett.*, vol..55, no. 9, pp.813-815, 1989.

[60] CARLSON, N.W., EVANS, G.A., BOUR, D.P. and LIEW, S.K., " Demonstration of a grating-surface-emitting diode laser with low-threshold current density, " *Appl. Phys. Lett.*, vol.56, no. 1, pp.16-18, 1990

[61] SHIMPE, R.M., " Cylindrical diffraction grating couplers and distributed feedback resonators for guided wave devices", *U.S. patent*, No. 4 743 083, May 10, 1988.

[62] TODA, M., " Single-mode behavior of a circular grating for potential disk-shaped DFB lasers". *IEEE J. Quantum Electron.*, vol.QE-26, No.3, pp.473-481, March 1990.

[63] ERDOGAN, T. and HALL, D.G., " Circularly symmetric distributed feedback semiconductor laser: an analysis ", *J. Appl. Phys.*, vol.68, no.4, pp.1435 - 1444, Aug. 1990.

[64] GONG, X.M., CHAN, A. K. and TAYLOR, H.F., " Lateral mode discrimination in surface emitting DBR lasers with cylindrical symmetry, " *SPIE Laser Diode Technology and Applications III*, vol. 1418, pp.422-433, 1991.

[65] ZHENG, X., " Theory of two-dimensional ' fingerprint' resonators", *Electron. Letts.*, vol.25, No.19, pp.1311-1312, 1989.

[66] ZHENG, X. and LACROIX, S., " Mode coupling in circular cylindrical system and its application to finger-print resonators". *J. Lightwave Technol.*, Vol.8, No.10, pp. 1509-1516, October 1990.

[67] KOGELNIK, H., " Theory of dielectric waveguides", in Integrated Optics, ed. TAMIR., T., 2nd edition, Springer-Verlag, 1982.

[68] TIEN, P.K., " Method of forming novel curved-line gratings and their use as reflectors and resonators in integrated optics". *Opt. Letts.*, vol.1, No.2, pp.64-66, August 1977.

[69] HORI, Y., SOGAWA, F., ASAKURA, H., KATO, M. and SERIZAWA, H., " Fabrication of a focusing grating mirror by electron beam lithography ". *Appl. Opt.*, vol.29, no.17, pp.2522-2526, June 1990.

[70] SHIONO, T., SETSUNE, K., YAMAZAKI, S. and WASA, K., " Rectangular-apertured micro-Fresnel lesns arrays fabricated by electron-beam lithography". *Appl.Opt.*, vol.26, no.3, pp.587-591, February, 1987.

[71] IP, A. and JACKSON, D. R., " Radiation from cylindrical leaky waves". *IEEE Trans. On Antennas and Propagations*, vol.38, no.4, pp.482-488, April 1990.

[72] ALEXOPOULOS, N.G. and KERNER, S.R., " Coupled-power theorem and orthogonality relations for optical disk waveguides". *J. Opt. Soc. Am.*, vol.67, no.12, pp.1634-1638, December 1977.

[73] SUDBϕ, A.S. and KAZARINOV, R.F., " Reflectivity of integrated optical filters based on elliptic Bragg reflectors". *J. Lightwave Technol.*, vol.8, no.6, pp. 998-1006, June 1990.

[74] SNYDER, A.W. and LOVE, J.D., Optical Waveguide Theory, Chapman and Hall , 1983.

[75] MARCUSE, D., Light Transmission Optics, Van Nostrand Reinold Co., New York, 1972.

[76] MARCUSE, D., Theory of Dielectric Optical Waveguides, Academic Press, 1974.

[77] YARIV, A., " Coupled-mode theory for guidede-wave optics ", *J. Quantum Electron.*, vol.QE-9, pp. 919-933, 1973,

[78] VASSALLO, C., " About coupled-mode theories for dielectric waveguides ", *J. Lightwave Technol.*, vol.6, no.2, pp.294 - 303, February, 1988, and the references cited therein.

[79] HAUS, H.A. and HUANG, W. " Coupled-mode theory, " *Proc. IEEE*, vol.79, no.10, pp. 1505-1517, Oct. 1991.

[80] HARRINGTON, R.F., Time-Harmonic Electromagnetic Fields, McGraw-Hill, 1961.

[81] BELL, W.W., Special Functions For Scientists And Engineers, D.Van Nostrand Company Ltd., 1968.

[82] MORSE, P.M. and FESHBACH, H., Methods of Theoretical Physics, McGraw-Hill, 1953.

[83] STREIFER, W., SCIFRES, D.R. and BURNHAM, R.D. " TM-mode coupling coefficients in guided-wave distributed feedback lasers ", *IEEE J. Quantum. Electron.*, vol.QE-12, no.2, pp. 74-78, Feb. 1976.

[84] WAGATSUMA, K., SASAKI, H. and SATO, S., " Mode conversion and optical filtering of obliquely incident waves in corrugated waveguide filters, " *IEEE J. Quantum Electron.*, vol.QE-15, no.7, pp. 632-637, 1979.

[85] HALL, D. G., " A comment on the coupled-mode equations used in guided-wave optics, " *Optics Commun.*, vol. 82, n. 5-6, pp. 453-455, 1991.

[86] HANDA, K., PENG, S.T. and TAMIR, T., " Improved perturbation analysis of dielectric grating, " *J. Appl. Phys.*, vol.5, pp.325-328, 1975.

[87] SUEMATSU, Y., ARAI, S. and KISHINO, K., " Dynamic single-mode semiconductor lasers with a distributed reflector, " *J. Lightwave Technol.*, vol. 1, no. 1, pp. 161- 176, Mar. 1983.

[88] AGRAWAL, G.P. and DUTTA, N.K., Long-wavelength semiconductor lasers, New York: van Nostrand Reinhold, 1986.

[89] IGA, K. and UCHIYAMA, S., " GaInAsP/InP surface-emitting laser diode, " *Optical and Quantum Electronics*, vol. 18, pp. 403-422, 1986.

[90] FALLAHI, M., WU, C., MARITAN, C., FOX, K. and BLAAUW, C., " Fabrication of circular gratings on InP by E-beam lithography and reactive ion etching, " presented at *1991 IEEE/LEOS Summer Topical Meeting: Microfabrication for Photonics and Optoelectronics*, Newport Beach, CA, U.S.A, July 31-Aug.2, 1991.

[91] KNIGHT, D. G., MOORE, W.T. and BRUCE, R. A., " Growth of semi-insulating InGaAsP alloys using low pressure MOCVD, " accepted for presentation at *VI International. Conf. on MOVPE*, Cambridge, M.A., U.S.A, 1992; also submitted to J. Crystal Growth.

[92] ARAKAWA, Y. and YARIV, A., " Quantum well lasers --- gain, spectra, dynamics, " *IEEE J. Quantum. Electron.*, vol.QE-22, no.9, pp. 1887-1899, Sep.1986.

[93] KITAMURA, M., SASAKI, T., TAKANO, S., YAMADA, H., HASUMI, H. and MITO, I., " Low-threshold, high-power single-longitudinal-mode operation in 1.5μm multiple-quantum-well distributed-feedback laser diodes, " *Electron. Letts*, vol.24, no.23, pp.1424-1426, Nov. 1988.

[94] PERALES, A., GOLDSTERN, L., ACCARD, A., FERNIER, B., LEBLOND, F., GOURDAIN, C. and BROSSON, P., " High performance DFB-MQW lasers at 1.5 μm grown by GSMBE, " *Electron. Letts*, vol.26, no.4, pp.236-238, Feb. 1990.

[95] XIAO, J.W., XU, J.Y., YANG, G.W., ZHANG, J.M., XU, Z.T. and CHEN, L. H., " Extremely low threshold current, buried-heterostructure strained InGaAs-GaAs multiquantum well lasers, " *Electron. Letts*, vol.28, no.2, pp.154-156, Jan. 1992.

Appendix I

Field Components In Cylindrical Coordinates

The Maxwell's equations are

$$\nabla \times \mathbf{E} = -j\omega\mu_0 \mathbf{H} \tag{A1.1}$$

$$\nabla \times \mathbf{H} = j\omega\varepsilon_0 \varepsilon \mathbf{E} \tag{A1.2}$$

In cylindrical coordinates, we can write

$$\mathbf{E} = E_\theta \hat{\theta} + E_z \hat{z} + E_r \hat{r} = \mathbf{E}_t + E_r \hat{r} \tag{A1.3}$$

$$\mathbf{H} = H_\theta \hat{\theta} + H_z \hat{z} + H_r \hat{r} = \mathbf{H}_t + H_r \hat{r} \tag{A1.4}$$

$$\nabla = \hat{\theta} \frac{1}{r} \frac{\partial}{\partial \theta} + \hat{z} \frac{\partial}{\partial z} + \hat{r} \frac{\partial}{\partial r} = \nabla_t + \hat{r} \frac{\partial}{\partial r} \tag{A1.5}$$

where

$$\mathbf{E}_t = E_\theta \hat{\theta} + H_z \hat{z}$$

$$\mathbf{H}_t = H_\theta \hat{\theta} + H_z \hat{z}$$

$$\nabla_t = \hat{\theta} \frac{1}{r} \frac{\partial}{\partial \theta} + \hat{z} \frac{\partial}{\partial z} \tag{A1.6}$$

Substituting Eq.(A1.4) and Eq.(A1.5) into Eq.(A1.2), we get

$$(\nabla_t + \hat{r}\frac{\partial}{\partial r}) \times (\mathbf{H}_t + H_r\hat{r}) = \nabla_t \times \mathbf{H}_t + \hat{r}\frac{\partial}{\partial r} \times \mathbf{H}_t + \nabla_t \times (H_r\hat{r}) \tag{A1.7}$$

but

$$\nabla_t \times \mathbf{H}_t = \hat{r}\,(\frac{1}{r}\frac{\partial H_\theta}{\partial \theta} - \frac{\partial H_z}{\partial z}) + \frac{H_\theta}{r}\hat{z} \tag{A1.8}$$

$$\hat{r}\frac{\partial}{\partial r} \times \mathbf{H}_t = \hat{z}\frac{\partial H_\theta}{\partial r} - \hat{\theta}\frac{\partial H_z}{\partial r} \tag{A1.9}$$

$$\nabla_t \times (H_r\hat{r}) = -\hat{z}\frac{1}{r}\frac{\partial H_r}{\partial \theta} + \hat{\theta}\frac{\partial E_r}{\partial z} \tag{A1.10}$$

Substituting Eqs.(A1.7)-(A1.10) into Eq.(A1.2), and comparing the two sides, yields

$$\mathbf{E}_r = \hat{r}\,(\frac{1}{j\omega\varepsilon_0\varepsilon})\,(\frac{1}{r}\frac{\partial H_\theta}{\partial \theta} - \frac{\partial H_z}{\partial z}) = (\frac{1}{j\omega\varepsilon_0\varepsilon})\,[\nabla_t \times \mathbf{H}_t - \frac{H_\theta}{r}\hat{z}] \tag{A1.11}$$

Appendix II

Orthonormal Relations Between Cylindrical Waves

A. Coupled-Power Theorem

We start with the complex Maxwell's equations for a lossless, scalar medium. Consider two different solutions labeled 1 and 2 that satisfy the vector wave equations

$$\nabla \times \mathbf{E}_{1,2} = -j\,\omega\,\mu_0 \mathbf{H}_{1,2}$$

$$\nabla \times \mathbf{H}_{1,2} = j\,\omega\,\varepsilon_0 \varepsilon\, \mathbf{E}_{1,2} \qquad \text{(A2.1)}$$

From Eq.(A2.1), we can prove that

$$\nabla . (\mathbf{E}_1 \times \mathbf{H}_2^* + \mathbf{E}_2^* \times \mathbf{H}_1) = 0 \qquad \text{(A2.2)}$$

Integrating on both sides over a cylindrical surface of radius r gives

$$\int_0^{2\pi} r\, d\theta \int_{-\infty}^{\infty} dz\ \nabla . (\mathbf{E}_1 \times \mathbf{H}_2^* + \mathbf{E}_2^* \times \mathbf{H}_1) = 0 \qquad \text{(A2.3)}$$

Using the following notation

$$\mathbf{A} = \mathbf{E}_1 \times \mathbf{H}_2^* + \mathbf{E}_2^* \times \mathbf{H}_1$$

$$\mathbf{A}_t = (\mathbf{E}_1 \times \mathbf{H}_2^* + \mathbf{E}_2^* \times \mathbf{H}_1)_t$$

$$\mathbf{A}_t = A_\theta \hat{\theta} + A_z \hat{z} \qquad \text{(A2.4)}$$

where the subscript " t " means the transverse (θ, z) components, we have

$$\int_0^{2\pi} r\,d\theta \int_{-\infty}^{\infty} dz\ \nabla . \mathbf{A} = \int_0^{2\pi} r\,d\theta \int_{-\infty}^{\infty} dz\ (\nabla_t + \hat{r}\frac{\partial}{\partial r}) . (A_r \hat{r} + \mathbf{A}_t)$$

$$= \int_0^{2\pi} r\,d\theta \int_{-\infty}^{\infty} dz\ (\nabla_t . \mathbf{A}_t) + \int_0^{2\pi} r\,d\theta \int_{-\infty}^{\infty} dz\ (\frac{A_r}{r} + \frac{\partial A_r}{\partial r})$$

$$= \oint \mathbf{A}_t . \mathbf{dl} + \int_0^{2\pi} r\,d\theta \int_{-\infty}^{\infty} dz\ (\frac{1}{r}\frac{\partial (rA_r)}{\partial r}) \qquad \text{(A2.5)}$$

Note that the line integral in Eq.(A2.5) is

$$\oint \mathbf{A}_t . \mathbf{dl} = \oint (\mathbf{E}_1 \times \mathbf{H}_2^* + \mathbf{E}_2^* \times \mathbf{H}_1)_t . \mathbf{dl} \qquad \text{(A2.6)}$$

which vanishes if at least one of the two waves is a guided wave with fields exponentially decaying toward infinity along the z-direction. The line integral also goes to zero when both waves are radiation waves, due to the oscillatory nature of the radiation fields [75]. Hence, from Eq.(A2.3) and Eq.(A2.5), we get

$$\int_0^{2\pi} r\,d\theta \int_{-\infty}^{\infty} dz\ \nabla . (\mathbf{E}_1 \times \mathbf{H}_2^* + \mathbf{E}_2^* \times \mathbf{H}_1)$$

$$= \int_0^{2\pi} \int_{-\infty}^{\infty} d\theta\, dz\ \frac{\partial}{\partial r} [r\,(\mathbf{E}_{1t} \times \mathbf{H}_{2t}^* + \mathbf{E}_{2t}^* \times \mathbf{H}_{1t}) . \hat{r}\,]$$

$$= \frac{\partial}{\partial r} \int_0^{2\pi} \int_{-\infty}^{\infty} d\theta\, dz\ [r\,(\mathbf{E}_{1t} \times \mathbf{H}_{2t}^* + \mathbf{E}_{2t}^* \times \mathbf{H}_{1t}) . \hat{r}\,] = 0$$

thus,

$$\int_0^{2\pi} \int_{-\infty}^{\infty} r\,d\theta\, dz\ [(\mathbf{E}_{1t} \times \mathbf{H}_{2t}^* + \mathbf{E}_{2t}^* \times \mathbf{H}_{1t}) . \hat{r}\,] = C \qquad \text{(A2.7)}$$

where C is a constant.

Let field 1 be the m-th order cylindrical wave that belongs to the ν-th slab mode of polarization τ, and field 2 be the n-th order cylindrical wave that is associated with the μ–th slab mode of polarization σ. The direction of propagation for field 1 is denoted by q and that for field 2 by p. Then, from Eq.(A2.7), we have

$$\int_0^{2\pi}\int_{-\infty}^{\infty} r\,d\theta\,dz\,[(\mathbf{E}_{\nu m\,t}^{(q)\tau}\times\mathbf{H}_{\mu n\,t}^{(p)\sigma\,*}+\mathbf{E}_{\mu n\,t}^{(p)\sigma\,*}\times\mathbf{H}_{\nu m\,t}^{(q)\tau})\,.\,\hat{r}\,]=C \tag{A2.8}$$

Eq.(A2.8) is called the coupled-power theorem in [72]. As we shall see in the following, for two different waves, the integration on the left-hand side of Eq.(A2.8) is zero, which implies the waves travel independently; if the two waves are the same, the left-hand side is nonzero and equals to the power that flows across a cylindrical surface, then Eq.(A2.8) simply states the conservation of power.

B. Orthonormal Relations

Orthonormal relations between cylindrical waves can be derived from the coupled-power theorem stated by Eq.(A2.8). The orthornormal relations between cylindrical waves can be shown to be

$$\int_0^{2\pi}\int_{-\infty}^{\infty} rd\theta dz\,\hat{r}.[\mathbf{E}_{\nu m\,t}^{(q)\tau}\times\mathbf{H}_{\mu n\,t}^{(p)\sigma\,*}+\mathbf{E}_{\mu n\,t}^{(p)\sigma\,*}\times\mathbf{H}_{\nu m\,t}^{(q)\tau}\,]=p\,\delta_{\nu\mu}\delta_{nm}\delta_{pq}\delta_{\sigma\tau} \tag{A2.9}$$

where σ, τ = TE, or TM, denotes the polarization of the waves; p, q= ± 1, represents outward or inward propagating waves; μ and ν denotes the mode number of the slab TE or TM modes; n and m denotes the order of the cylindrical waves.

In the following, Eq.(A2.9) is proved for each of the three cases: TE-TM(TM-TE), TE-TE and TM-TM orthonormalities.

B.1 TE-TM(TM-TE) Orthonormality

Substituting the fields for TE-waves (Eq.(1.12)) and those for TM-waves(Eq.(1.13)) into the left hand-side of Eq.(A2.8), we obtain

$$\int_0^{2\pi}\int_{-\infty}^{\infty} r d\theta dz\, \hat{r}.[E_{\nu m\, t}^{(q)TM} \times H_{\mu n\, t}^{(p)TE\,*} + E_{\mu n\, t}^{(p)TE\,*} \times H_{\nu m\, t}^{(q)TM}]$$

$$= \int_0^{2\pi}\int_{-\infty}^{\infty} (E_{\nu m\, \theta}^{(q)TM} H_{\mu n\, z}^{(p)TE\,*} - E_{\nu m\, z}^{(q)TM} H_{\mu n\, \theta}^{(p)TE\,*})\, r\, d\theta dz$$

$$= j A_{\mu n}^{(p)TE\,*} A_{\nu m}^{(q)TM} R_m^{(q)}(\beta_\nu^{TM} r) R_n^{(p)*}(\beta_\mu^{TE} r) \int_0^{2\pi} e^{j(m-n)\theta} d\theta$$

$$\cdot \int_{-\infty}^{\infty} dz \left[\frac{m}{(\beta_\nu^{TM})^2} \frac{d(Z_\nu^{TM})}{dz} (Z_\mu^{TE})^* + \frac{n}{(\beta_\mu^{TE})^2} \frac{d(Z_\mu^{TE})^*}{dz} (Z_\nu^{TM})\right]$$

$$= j A_{\mu n}^{(p)TE\,*} A_{\nu m}^{(q)TM} R_m^{(q)}(\beta_\nu^{TM} r)\, R_n^{(p)*}(\beta_\mu^{TE} r)\, 2\pi\, \delta_{nm}$$

$$\cdot \int_{-\infty}^{\infty} dz \left[\frac{n}{(\beta_\nu^{TM})^2} \frac{d(Z_\nu^{TM})}{dz} (Z_\mu^{TE})^* + \frac{n}{(\beta_\mu^{TE})^2} \frac{d(Z_\mu^{TE})^*}{dz} (Z_\nu^{TM})\right]$$

$$= C \qquad \text{(A2.10)}$$

where δ_{nm} denotes the Kronecker's delta. The constant C is zero because for (βr) approaching infinity

$$R_m^{(q)}(\beta_\nu^{TM} r) R_n^{(p)*}(\beta_\mu^{TE} r) \to O(\frac{1}{r}) \to 0 \qquad \text{(A2.11)}$$

Therefore, we can write

$$\int_0^{2\pi}\int_{-\infty}^{\infty} r d\theta dz\, \hat{r}.[E_{\nu m\, t}^{(q)TM} \times H_{\mu n\, t}^{(p)TE\,*} + E_{\mu n\, t}^{(p)TE\,*} \times H_{\nu m\, t}^{(q)TM}] = 0 \qquad \text{(A2.12)}$$

This is the orthonormal relation between TE and TM cylindrical waves.

B.2 TE-TE Orthonormality

Consider the n-th order TE cylindrical wave associated with the μ-th slab TE-mode and the m-th order TE cylindrical waves of the ν-th slab TE-mode. Putting Eq.(1.12) into Eq.(A2.8), we obtain

$$\int_0^{2\pi}\int_{-\infty}^{\infty} \hat{r}\cdot\,(\mathbf{E}_{\nu m\,t}^{(q)TE}\times\mathbf{H}_{\mu n\,t}^{(p)TE\,*}+\mathbf{E}_{\mu n\,t}^{(p)TE\,*}\times\mathbf{H}_{\nu m\,t}^{(q)TE})\,r\,d\theta dz$$

$$=\int_0^{2\pi}\int_{-\infty}^{\infty} (E_{\nu m\,\theta}^{(q)TE}H_{\mu n\,z}^{(p)TE\,*}+E_{\mu n\,\theta}^{(p)TE\,*}\times H_{\nu m\,z}^{(q)TE})\,r\,d\theta dz$$

$$=j\,\omega\mu_0 r\,A_m^{(q)TE}A_n^{(p)TE\,*}\,[\,\frac{1}{(\beta_\nu^{TE})^2}\frac{dR_m^{(q)}(\beta_\nu^{TE}r)}{dr}R_n^{(p)*}(\beta_\mu^{TE}r)-\frac{1}{(\beta_\mu^{TE})^2}\frac{dR_n^{(p)*}(\beta_\mu^{TE}r)}{dr}R_m^{(q)}(\beta_\nu^{TE}r)\,]$$

$$\cdot\int_0^{2\pi}\int_{-\infty}^{\infty} Z_\nu^{TE}(z)Z_\mu^{TE\,*}(z)\,e^{j(m-n)\theta}\,d\theta dz$$

$$=j\,2\pi\,\delta_{nm}A_{\mu n}^{TE\,*}A_{\nu m}^{TE}\omega\mu_0 r\,[\int_{-\infty}^{\infty} Z_\nu^{TE}(z)Z_\mu^{TE\,*}(z)\,dz\,]$$

$$\cdot\,[\,\frac{1}{(\beta_\nu^{TE})^2}\frac{dR_m^{(q)}(\beta_\nu^{TE}r)}{dr}R_n^{(p)*}(\beta_\mu^{TE}r)-\frac{1}{(\beta_\mu^{TE})^2}\frac{dR_n^{(p)*}(\beta_\mu^{TE}r)}{dr}R_m^{(q)}(\beta_\nu^{TE}r)\,]$$

$$=C \qquad \text{(A2.13)}$$

Unless μ=ν, n=m and p=q, the constant C is zero. This can be easily proved. If $n \neq m$, $\delta_{nm}=0$, evidently C=0. If n=m, but $\mu \neq \nu$, the orthogonality relations between slab TE modes [67] yields

$$\int_{-\infty}^{\infty} Z_\nu^{TE}(z)Z_\mu^{TE\,*}(z)\,dz=0 \qquad \text{(A2.14)}$$

thus C=0 for $\mu \neq \nu$.If $\mu=\nu$, n=m, but $p \neq q$, for example, p=+, q= -. Then,

$$\left[\frac{1}{(\beta_\mu)^2}\frac{dR_n^{(q)}(\beta_\mu r)}{dr}R_n^{(p)*}(\beta_\mu r) - \frac{1}{(\beta_\mu)^2}\frac{dR_n^{(p)*}(\beta_\mu r)}{dr}R_n^{(q)}(\beta_\mu r)\right]$$

$$= \left[\frac{1}{(\beta_\mu)^2}\frac{dR_n^{(-)}(\beta_\mu r)}{dr}R_m^{(+)*}(\beta_\mu r) - \frac{1}{(\beta_\mu)^2}\frac{dR_m^{(+)*}(\beta_\mu r)}{dr}R_n^{(-)}(\beta_\mu r)\right]$$

$$= \left[\frac{1}{(\beta_\mu)^2}\frac{dH_n^{(1)}(\beta_\mu r)}{dr}H_n^{(2)*}(\beta_\mu r) - \frac{1}{(\beta_\mu)^2}\frac{dH_n^{(2)*}(\beta_\mu r)}{dr}H_n^{(1)}(\beta_\mu r)\right]$$

$$= \left[\frac{1}{(\beta_\mu)^2}\frac{dH_n^{(1)}(\beta_\mu r)}{dr}H_n^{(1)}(\beta_\mu r) - \frac{1}{(\beta_\mu)^2}\frac{dH_n^{(1)}(\beta_\mu r)}{dr}H_n^{(1)}(\beta_\mu r)\right]$$

$$= 0 \qquad \text{(A2.15a)}$$

Similarly, for p= -, q= +, we obtain

$$\left[\frac{1}{(\beta_\mu)^2}\frac{dR_n^{(+)}(\beta_\mu r)}{dr}R_n^{(-)*}(\beta_\mu r) - \frac{1}{(\beta_\mu)^2}\frac{dR_n^{(-)*}(\beta_\mu r)}{dr}R_n^{(+)}(\beta_\mu r)\right]$$

$$= \left[\frac{1}{(\beta_\mu)^2}\frac{dH_n^{(2)}(\beta_\mu r)}{dr}H_n^{(2)}(\beta_\mu r) - \frac{1}{(\beta_\mu)^2}\frac{dH_n^{(2)}(\beta_\mu r)}{dr}H_n^{(2)}(\beta_\mu r)\right]$$

$$= 0 \qquad \text{(A2.15b)}$$

Again, C = 0.

For $\mu=\nu$, n=m and p=q, because

$$R_n^{(+)}(\beta r) = R_n^{(-)*}(\beta r) = H_n^{(2)}(\beta r)$$

$$R_n^{(-)}(\beta r) = R_n^{(+)*}(\beta r) = H_n^{(1)}(\beta r)$$

we have

$$\left[\frac{1}{(\beta)^2}\frac{dR_n^{(\pm)}(\beta r)}{dr}R_n^{(\pm)*}(\beta r) - \frac{1}{(\beta)^2}\frac{dR_n^{(\pm)*}(\beta r)}{dr}R_n^{(\pm)}(\beta r)\right]$$

$$= \pm\frac{1}{(\beta)^2}\left[\frac{dH_n^{(2)}(\beta r)}{dr}H_n^{(2)*}(\beta r) - \frac{dH_n^{(2)*}(\beta r)}{dr}H_n^{(2)}(\beta r)\right]$$

$$= \pm\frac{1}{(\beta)^2}\left[\frac{dH_n^{(2)}(\beta r)}{dr}H_n^{(1)}(\beta r) - \frac{dH_n^{(1)}(\beta r)}{dr}H_n^{(2)}(\beta r)\right]$$

$$= \pm\frac{1}{\beta}\frac{4(-j)}{\pi\beta r} \qquad \text{(A2.16)}$$

where we have utilized the Wronskian for Hankel functions [82]

$$\left[\frac{dH_n^{(2)}(x)}{dx}H_n^{(1)}(x) - \frac{dH_n^{(1)}(x)}{dx}H_n^{(2)}(x)\right] = -\frac{4j}{\pi x} \qquad \text{(A2.17)}$$

Substituting (A2.16) into Eq.(A2.13), we get

$$C = (\pm)\frac{8\omega_0\mu_0}{(\beta_\mu^{TE})^2}\left|A_{\mu n}^{TE}\right|^2\int_{-\infty}^{\infty}\left|Z_\mu^{TE}\right|^2 dz \qquad \text{(A2.18)}$$

for $\mu=\nu$, $n=m$ and $p=q$.

Let C in Eq.(A2.18) be equal to 1 for the upper sign, and to -1 for the lower sign. Then the field can be normalized by

$$\left|A_{\mu n}^{TE}\right|^2 = \frac{(\beta_\mu)^{TE\ 2}}{8\omega_0\mu_0\int_{-\infty}^{\infty}\left|Z_\mu^{TE}\right|^2 dz} \tag{A2.19}$$

Combining all the cases above, we can thus write the orthonormal relation between TE cylindrical waves as

$$\int_0^{2\pi}\int_{-\infty}^{\infty}\hat{r}\cdot\left(E_{\nu m\,t}^{(q)TE}\times H_{\mu n\,t}^{(p)TE\,*}+E_{\mu n\,t}^{(p)TE\,*}\times H_{\nu m\,t}^{(q)TE}\right) r\,d\theta dz = p\,\delta_{\mu\nu}\delta_{nm}\delta_{pq} \tag{A2.20}$$

where p= +1 for outward-propagating waves, and p= -1 for inward-propagating wave.

B.3 TM-TM Orthonormality

The derivation of the orthonormal relation for TM cylindrical waves is similar to that of TE waves. We again start from the coupled power theorem. Using the field distribution for TM-waves in Eq.(1.13), we can derive

$$\int_0^{2\pi}\int_{-\infty}^{\infty} r d\theta dz\,\hat{r}.[E_{\nu m\,t}^{(q)TM}\times H_{\mu n\,t}^{(p)TM\,*}+E_{\mu n\,t}^{(p)TM\,*}\times H_{\nu m\,t}^{(q)TM}]$$

$$=\int_0^{2\pi}\int_{-\infty}^{\infty} r d\theta dz\,[-E_{\nu m\,z}^{(q)TM}H_{\mu n\,\theta}^{(p)TM\,*}-E_{\mu n\,z}^{(p)TM\,*}H_{\nu m\,\theta}^{(q)TM}]$$

$$=j\,\omega_0\varepsilon_0\,A_{\mu n}^{(p)TM\,*}A_{\nu m}^{(q)TM}\cdot\int_0^{2\pi}\int_{-\infty}^{\infty} r d\theta dz\,\varepsilon\,e^{j(m-n)\theta}\,Z_\mu^{TM\,*}Z_\nu^{TM}$$

$$\cdot\left[\frac{1}{(\beta_\nu^{TM})^2} R_n^{(p)*}(\beta_\mu^{TM} r)\frac{dR_m^{(q)}(\beta_\nu^{TM} r)}{dr} - \frac{1}{(\beta_\mu^{TM})^2} R_m^{(q)}(\beta_\nu^{TM} r)\frac{dR_n^{(p)*}(\beta_\mu^{TM} r)}{dr}\right]$$

$$= j\omega_0\varepsilon_0 A_{\mu n}^{(p)TM*} A_{\nu m}^{(q)TM} 2\pi r\delta_{nm}\int_{-\infty}^{\infty} dz\, \varepsilon Z_\mu^{TM*} Z_\nu^{TM}$$

$$\cdot\left[\frac{1}{(\beta_\nu^{TM})^2} R_n^{(p)*}(\beta_\mu^{TM} r)\frac{dR_n^{(q)}(\beta_\nu^{TM} r)}{dr} - \frac{1}{(\beta_\mu^{TM})^2} R_n^{(q)}(\beta_\nu^{TM} r)\frac{dR_n^{(p)*}(\beta_\mu^{TM} r)}{dr}\right]$$

$$= C \qquad \text{(A2.21)}$$

If $n\neq m$, $\delta_{nm}=0$, then $C=0$. If $\mu\neq\nu$, from the orthogonality relations between TM slab modes[67], the Z-functions satisfy

$$\int_{-\infty}^{\infty} r d\theta dz\, \varepsilon Z_\mu^{TM} Z_\nu^{TM\,*} = 0 \qquad \text{(A2.22)}$$

which gives $C=0$. If $n=m$, $\mu=\nu$, but $p\neq q$, terms in the square bracket cancel each other (see Eq.(A2.15a)-(A2.15b)), thus we also have $C=0$.

For the case of $\mu=\nu$, $m=n$, $p=q$, we have

$$\frac{1}{(\beta^2)}\left[R_n^{(\pm)*}(\beta r)\frac{dR_n^{(\pm)}(\beta r)}{dr} - R_n^{(\pm)}(\beta r)\frac{dR_n^{(\pm)*}(\beta r)}{dr}\right]$$

$$= -\frac{\pm}{(\beta^2)}\left[H_n^{(2)}(\beta r)\frac{dH_n^{(2)*}(\beta r)}{dr} - H_n^{(2)*}(\beta r)\frac{dH_n^{(2)}(\beta r)}{dr}\right]$$

$$= -\frac{\pm}{\beta}\left[H_n^{(2)}(\beta r)\frac{dH_n^{(1)}(\beta r)}{d(\beta r)} - H_n^{(1)}(\beta r)\frac{dH_n^{(2)}(\beta r)}{d(\beta r)}\right]$$

$$= \frac{\pm 1}{\beta} \frac{4(-j)}{\pi \beta r} \qquad \text{(A2.23)}$$

Thus, putting Eq.(A2.23) into Eq.(A2.21), we obtain

$$C = \pm \frac{8\,\omega\varepsilon_0}{\beta_\mu^2} \left| A_{\mu n}^{(p)TM} \right|^2 \int_{-\infty}^{\infty} dz\ \varepsilon Z_\mu^{TM} Z_\mu^{TM*} \qquad \text{(A2.24)}$$

Let C=1, for p=+, and C=-1 for p=-. Normalizing the field by

$$\left| A_{\mu n}^{(p)TM} \right|^2 = \frac{(\beta_\mu^{TM})^2}{8\,\omega\varepsilon_0 \int_{-\infty}^{\infty} dz\ \varepsilon Z_\mu^{TM} Z_\mu^{TM*}} \qquad \text{(A2.25)}$$

We, then, can write the orthonormal relation for TM cylindrical waves as

$$\int_0^{2\pi} \int_{-\infty}^{\infty} r d\theta dz\, \hat{r}.[E_{\nu m\, t}^{(q)TM} \times H_{\mu n\, t}^{(p)TM*} + E_{\mu n\, t}^{(p)TM*} \times H_{\nu m\, t}^{(q)TM}] = p\, \delta_{\nu\mu} \delta_{nm} \delta_{pq} \qquad \text{(A2.26)}$$

where p=+1 for outward waves and p=-1 for inward waves.

Summarizing Eqs.(A2.12), (A2.20) and (A2.26), we conclude that the orthonormal relations between cylindrical waves are simply expressed by Eq.(A2.9).

Appendix III

Proof of Self-Consistency

For a general field distribution ($\mathbf{E}_1, \mathbf{H}_1$) given by Eq.(1.24), the time averaged Poynting vector in the r-direction is

$$S_r = (\mathbf{E}_{1t} \times \mathbf{H}^*_{1t} + \mathbf{E}^*_{1t} \times \mathbf{H}_{1t}) \cdot \hat{r} \tag{A3.1}$$

The total power transported in the radial direction is calculated from

$$P_{total} = \int_0^{2\pi} \int_{-\infty}^{\infty} r \, d\theta dz \, S_r$$

$$= \int_0^{2\pi} \int_{-\infty}^{\infty} r \, d\theta dz \, \hat{r} \cdot [(\sum_{p,\sigma,\mu,n} a_{\mu n}^{(p)\sigma} \mathbf{E}_{\mu n\, t}^{(p)\sigma}) \times (\sum_{q,\tau,\nu,m} a_{\nu m}^{(q)\tau *} \mathbf{H}_{\nu m\, t}^{(q)\tau *})$$

$$+ (\sum_{q,\tau,\nu,m} a_{\nu m}^{(q)\tau *} \mathbf{E}_{\nu m\, t}^{(q)\tau *}) \times (\sum_{p,\sigma,\mu,n} a_{\mu n}^{(p)\sigma} \mathbf{H}_{\mu n\, t}^{(p)\sigma})]$$

$$= \sum_{p,\sigma,\mu,n} \sum_{q,\tau,\nu,m} a_{\mu n}^{(p)\sigma} a_{\nu m}^{(q)\tau *} \int_0^{2\pi} \int_{-\infty}^{\infty} r \, d\theta dz \, \hat{r} \cdot [\mathbf{E}_{\mu n\, t}^{(p)\sigma} \times \mathbf{H}_{\nu m\, t}^{(q)\tau *} + \mathbf{E}_{\nu m\, t}^{(q)\tau *} \times \mathbf{H}_{\mu n\, t}^{(p)\sigma}]$$

$$= \sum_{p,\sigma,\mu,n} \sum_{q,\tau,\nu,m} a_{\mu n}^{(p)\sigma} a_{\nu m}^{(q)\tau *} \, p \, \delta_{\mu\nu} \delta_{nm} \delta_{pq} \delta_{\sigma\tau}$$

$$= \sum_{p,\sigma,\mu,n} \left| a_{\mu n}^{(p)\sigma} \right|^2 p$$

$$= \sum_{\sigma,\mu,n} \left[\left| a_{\mu n}^{(+)\sigma} \right|^2 - \left| a_{\mu n}^{(-)\sigma} \right|^2 \right] \qquad \text{(A3.2)}$$

Now if we substitute Eq.(1.35) into Eq.(A3.2) and make use of Eq.(1.33), we have

$$\frac{dP_{total}}{dr} = \sum_{\sigma,\mu,n} \left[\frac{da_{\mu n}^{(+)\sigma}}{dr} a_{\mu n}^{(+)\sigma *} + a_{\mu n}^{(+)\sigma} \frac{da_{\mu n}^{(+)\sigma *}}{dr} - \frac{da_{\mu n}^{(-)\sigma}}{dr} a_{\mu n}^{(-)\sigma *} - a_{\mu n}^{(-)\sigma} \frac{da_{\mu n}^{(-)\sigma *}}{dr} \right]$$

$$= \sum_{\sigma,\mu,n} \{ -j \sum_{\tau,\nu,m} \left[K_{\mu n,\nu m}^{(+)\sigma,(+)\tau} a_{\nu m}^{(+)\tau} + K_{\mu n,\nu m}^{(+)\sigma,(-)\tau} a_{\nu m}^{(-)\tau} \right] a_{\mu n}^{(+)\sigma *}$$

$$+ a_{\mu n}^{(+)\sigma} \left[j \sum_{\tau,\nu,m} \left(K_{\mu n,\nu m}^{(+)\sigma,(+)\tau} \right)^* \left(a_{\nu m}^{(+)\tau} \right)^* + \left(K_{\mu n,\nu m}^{(+)\sigma,(-)\tau} \right)^* \left(a_{\nu m}^{(-)\tau} \right)^* \right]$$

$$- j \sum_{\tau,\nu,m} \left[K_{\mu n,\nu m}^{(-)\sigma,(+)\tau} a_{\nu m}^{(+)\tau} + K_{\mu n,\nu m}^{(-)\sigma,(-)\tau} a_{\nu m}^{(-)\tau} \right] a_{\mu n}^{(-)\sigma *}$$

$$+ a_{\mu n}^{(-)\sigma} \left[j \sum_{\tau,\nu,m} \left(K_{\mu n,\nu m}^{(-)\sigma,(+)\tau} \right)^* \left(a_{\nu m}^{(+)\tau} \right)^* + \left(K_{\mu n,\nu m}^{(-)\sigma,(-)\tau} \right)^* \left(a_{\nu m}^{(-)\tau} \right)^* \right] \}$$

$$= j \left[\sum_{\tau,\nu,m} \left(\sum_{\sigma,\mu,n} K_{\nu m,\,\mu n}^{(+)\tau,(+)\sigma} a_{\mu n}^{(+)\sigma} \right) \left(a_{\nu m}^{(+)\tau} \right)^* - \sum_{\sigma,\mu,n} \left(\sum_{\tau,\nu,m} K_{\mu n,\nu m}^{(+)\sigma,(+)\tau} a_{\nu m}^{(+)\tau} \right) \left(a_{\mu n}^{(+)\sigma} \right)^* \right]$$

$$+ j \left[\sum_{\tau,\nu,m} \left(\sum_{\sigma,\mu,n} K_{\nu m,\,\mu n}^{(+)\tau,(-)\sigma} a_{\mu n}^{(-)\sigma} \right) \left(a_{\nu m}^{(+)\tau} \right)^* - \sum_{\sigma,\mu,n} \left(\sum_{\tau,\nu,m} K_{\mu n,\nu m}^{(+)\sigma,(-)\tau} a_{\nu m}^{(-)\tau} \right) \left(a_{\mu n}^{(+)\sigma} \right)^* \right]$$

$$+j\Big[\sum_{\tau,\nu,m}\Big(\sum_{\sigma,\mu,n} K^{(-)\tau,(+)\sigma}_{\nu m,\,\mu n}\, a^{(+)\sigma}_{\mu n}\Big)\big(a^{(-)\tau}_{\nu m}\big)^{*} - \sum_{\sigma,\mu,n}\Big(\sum_{\tau,\nu,m} K^{(-)\sigma,(+)\tau}_{\mu n,\nu m}\, a^{(+)\tau}_{\nu m}\Big)\big(a^{(-)\sigma}_{\mu n}\big)^{*}\Big]$$

$$+j\Big[\sum_{\tau,\nu,m}\Big(\sum_{\sigma,\mu,n} K^{(-)\tau,(-)\sigma}_{\nu m,\,\mu n}\, a^{(-)\sigma}_{\mu n}\Big)\big(a^{(-)\tau}_{\nu m}\big)^{*} - \sum_{\sigma,\mu,n}\Big(\sum_{\tau,\nu,m} K^{(-)\sigma,(-)\tau}_{\mu n,\nu m}\, a^{(-)\tau}_{\nu m}\Big)\big(a^{(-)\sigma}_{\mu n}\big)^{*}\Big]$$

$$= 0 \qquad \text{(A3.3)}$$

The terms in each square bracket cancel out. Therefore, we conclude that the coupled-wave theory presented here conserves the total power and is consequently self-consistent.

Appendix IV

Expressions for Coupling Coefficients

A. Coupling Coefficients Between TE Cylindrical Waves

According to Eq.(1.37) in Chapter 1, the coupling coefficients for TE-cylindrical waves are defined by

$$K_{\mu n,\nu n}^{(p,q)TETE} = 2\pi r\, A_{\nu n}^{(q)TE} A_{\mu n}^{(p)TE*} \frac{(\omega^2\varepsilon_0\mu_0)^2}{(\beta_\nu^{TE}\beta_\mu^{TE})(\omega\varepsilon_0)} \int_{-\infty}^{\infty} dz\, \Delta\varepsilon(r,z)\, Z_\nu^{TE} Z_\mu^{TE*}$$

$$\cdot \left\{ \frac{dR_n^{(q)}(\beta_\nu^{TE} r)}{d(\beta_\nu^{TE} r)} \frac{dR_n^{(p)*}(\beta_\mu^{TE} r)}{d(\beta_\mu^{TE} r)} + \frac{\varepsilon}{\varepsilon+\Delta\varepsilon} \left(\frac{n}{\beta_\nu^{TE} r}\right)\left(\frac{n}{\beta_\mu^{TE} r}\right) R_n^{(q)}(\beta_\nu^{TE} r) R_n^{(p)*}(\beta_\mu^{TE} r) \right\} \tag{A4.1}$$

The R's describe the radial dependence of the cylindrical waves with

$$R_n^{(+)}(\beta r) = H_n^{(2)}(\beta r)$$

$$R_n^{(-)}(\beta r) = H_n^{(1)}(\beta r) \tag{A4.2}$$

where $H_n^{(1)}(\beta r)$ and $H_n^{(2)}(\beta r)$ are the Hankel functions of the first kind and the second kind, respectively. The A's are normalization constants defined by

$$\left|A_{\mu n}^{(p)TE}\right|^2 = \frac{(\beta_\mu^{TE})^2}{8\omega\mu_0 \int_{-\infty}^{\infty} \left|Z_\mu^{TE}\right|^2 dz} \tag{A4.3}$$

To simplify the expression, we set $A_{\nu n}^{TE(+)} = A_{\nu n}^{TE(-)}$ and $A_{\mu n}^{TE(+)} = A_{\mu n}^{TE(-)}$ and substitute Eq.(A4.3) into Eq.(A4.1) to obtain

$$K_{\mu n,\nu n}^{(p,q)TETE} = \frac{\pi r}{4} \frac{k_0^2 \int_{-\infty}^{\infty} \Delta\varepsilon(r,z)\, Z_\nu^{TE} Z_\mu^{TE*}\, dz}{\sqrt{\int_{-\infty}^{\infty} \left|Z_\nu^{TE}\right|^2 dz \int_{-\infty}^{\infty} \left|Z_\mu^{TE}\right|^2 dz}}$$

$$\cdot \{ \frac{dR_n^{(q)}(\beta_\nu r)}{d(\beta_\nu r)}^{TE} \frac{dR_n^{(p)*}(\beta_\mu r)}{d(\beta_\mu r)}^{TE} + \frac{\varepsilon}{\varepsilon+\Delta\varepsilon} (\frac{n}{\beta_\nu r}^{TE})(\frac{n}{\beta_\mu r}^{TE}) R_n^{(q)}(\beta_\nu r)^{TE} R_n^{(p)*}(\beta_\mu r)^{TE} \}$$

$$\approx \frac{\pi r}{4} \frac{k_0^2 \int_{-\infty}^{\infty} \Delta\varepsilon(r,z)\, Z_\nu^{TE} Z_\mu^{TE*}\, dz}{\sqrt{\int_{-\infty}^{\infty} |Z_\nu^{TE}|^2 dz \int_{-\infty}^{\infty} |Z_\mu^{TE}|^2 dz}}$$

$$\cdot \{ \frac{dR_n^{(q)}(\beta_\nu r)}{d(\beta_\nu r)}^{TE} \frac{dR_n^{(p)*}(\beta_\mu r)}{d(\beta_\mu r)}^{TE} + (\frac{n}{\beta_\nu r}^{TE})(\frac{n}{\beta_\mu r}^{TE}) R_n^{(q)}(\beta_\nu r)^{TE} R_n^{(p)*}(\beta_\mu r)^{TE} \} \qquad \text{(A4.4)}$$

where we have used the approximation that $\Delta\varepsilon/(\varepsilon+\Delta\varepsilon) << 1$.

Define

$$K_{\mu\nu}^{TE\,TE}(r) = \frac{1}{2} \frac{k_0^2}{\sqrt{(\beta_\mu^{TE}\beta_\nu^{TE})}} \frac{\int_{-\infty}^{\infty} \Delta\varepsilon(r,z)\, Z_\mu^{TE*} Z_\nu^{TE}\, dz}{\sqrt{\int_{-\infty}^{\infty} \left|Z_\mu^{TE}\right|^2 dz \int_{-\infty}^{\infty} \left|Z_\nu^{TE}\right|^2 dz}} \qquad \text{(A4.5a)}$$

$$F_{\mu n,\nu n}^{(p,q)TE\,TE}(r) = \frac{\pi r}{2}\sqrt{\beta_\nu^{TE}\,\beta_\mu^{TE}}\,\{\frac{dR_n^{(q)}(\beta_\nu^{TE} r)}{d(\beta_\nu^{TE} r)}\,\frac{dR_n^{(p)*}(\beta_\mu^{TE} r)}{d(\beta_\mu^{TE} r)} + (\frac{n}{\beta_\nu^{TE} r})(\frac{n}{\beta_\mu^{TE} r})\,R_n^{(q)}(\beta_\nu^{TE} r)R_n^{(p)*}(\beta_\mu^{TE} r)\}$$

(A4.5b)

Then, Eq.(A4.4) becomes

$$K_{\mu n,\nu n}^{(p,q)TE\,TE} = F_{\mu n,\nu n}^{(p,q)TE\,TE}(r)\,K_{\mu\nu}^{TE\,TE}(r) \qquad (A4.6)$$

From the recurrence formulae of Hankel functions [90], we have

$$\frac{n}{x}R_n^{(p)}(x) = \frac{1}{2}[\,R_{n-1}^{(p)}(x) + R_{n+1}^{(p)}(x)]$$

$$R_n^{(p)\prime}(x) = \frac{1}{2}[\,R_{n-1}^{(p)}(x) - R_{n+1}^{(\pi)}(x)\,] \qquad (A4.7)$$

and

$$\{\frac{dR_n^{(q)}(\beta_\nu^{TE} r)}{d(\beta_\nu^{TE} r)}\,\frac{dR_n^{(p)*}(\beta_\mu^{TE} r)}{d(\beta_\mu^{TE} r)} + (\frac{n}{\beta_\nu^{TE} r})(\frac{n}{\beta_\mu^{TE} r})\,R_n^{(q)}(\beta_\nu^{TE} r)R_n^{(p)*}(\beta_\mu^{TE} r)\}$$

$$= \frac{1}{2}[\,R_{n-1}^{(q)}(\beta_\nu^{TE} r)\,R_{n-1}^{(p)*}(\beta_\mu^{TE} r) + R_{n+1}^{(q)}(\beta_\nu^{TE} r)\,R_{n+1}^{(p)*}(\beta_\mu^{TE} r)\,] \qquad (A4.8)$$

Substitution of Eq.(A4.8) into the right-hand side of Eq.(5.b) yields

$$F_{\mu n,\nu n}^{(p,q)TE\,TE}(r) = \frac{\pi r}{4}\sqrt{\beta_\nu^{TE}\,\beta_\mu^{TE}}\,[\,R_{n-1}^{(q)}(\beta_\nu^{TE} r)\,R_{n-1}^{(p)*}(\beta_\mu^{TE} r) + R_{n+1}^{(q)}(\beta_\nu^{TE} r)\,R_{n+1}^{(p)*}(\beta_\mu^{TE} r)\,] \qquad (A4.9)$$

B. Coupling Coefficients For TM-Cylindrical Waves

The coupling coefficients for TM-TM coupling are given by Eq.(1.39) in Chapter 1, i.e.

$$K^{(p,q)TMTM}_{\mu n,\nu n} = 2\pi r\, A^{(q)TM}_{\nu n} A^{(p)TM*}_{\mu n}\, \omega\varepsilon_0 \int_{-\infty}^{\infty} dz\, \Delta\varepsilon(r,z)$$

$$\cdot\Big[\frac{n^2}{(\beta^{TM}_{\nu}\beta^{TM}_{\mu})^2}\frac{1}{r^2}\frac{dZ^{TM}_{\nu}}{dz}\frac{dZ^{TM*}_{\mu}}{dz} R^{(q)}_n(\beta^{TM}_{\nu} r) R^{(p)*}_n(\beta^{TM}_{\mu} r) + R^{(q)}_n(\beta^{TM}_{\nu} r)\, R^{(p)*}_n(\beta^{TM}_{\mu} r)\, Z^{TM}_{\nu} Z^{TM*}_{\mu}$$

$$+\frac{\varepsilon}{\varepsilon+\Delta\varepsilon}\frac{1}{(\beta^{TM}_{\nu}\beta^{TM}_{\mu})^2}\frac{dR^{(q)}_n(\beta^{TM}_{\nu} r)}{dr}\frac{dR^{(p)*}_n(\beta^{TM}_{\mu} r)}{dr}\frac{dZ^{TM}_{\nu}}{dz}\frac{dZ^{TM*}_{\mu}}{dz}\Big] \qquad \text{(A4.10)}$$

where the A's are normalization constants defined by

$$\left|A^{(p)TM}_{\mu n}\right|^2 = \frac{(\beta^{TM}_{\mu})^2}{8\,\omega\varepsilon_0 \int_{-\infty}^{\infty} dz\, \varepsilon Z^{TM}_{\mu} Z^{TM*}_{\mu}} \qquad \text{(A4.11)}$$

As in the case for TE cylindrical waves, we set $A^{TM(+)}_{\nu n} = A^{TM(-)}_{\nu n}$ and $A^{TM(+)}_{\mu n} = A^{TM(-)}_{\mu n}$. Substituting Eq.(A4.11) into Eq.(A4.10) and using the notation $x=\beta^{TM}_{\nu} r$, $y=\beta^{TM}_{\mu} r$, we obtain

$$K_{\mu n,\nu n}^{(p,q)\text{™}\text{™}} = \frac{\pi r}{4} \frac{\beta_\nu^{\text{™}}\,\beta_\mu^{\text{™}}}{\sqrt{\int_{-\infty}^{\infty} dz\ \varepsilon |Z_\nu^{\text{™}}|^2 \int_{-\infty}^{\infty} dz\ \varepsilon |Z_\mu^{\text{™}}|^2}}$$

$$\cdot \int_{-\infty}^{\infty} dz\, \Delta\varepsilon(r,z) \{ R_n^{(q)}(x)\, R_n^{(p)*}(y)\, Z_\nu^{\text{™}} Z_\mu^{\text{™}*}$$

$$+ \frac{1}{\beta_\nu^{\text{™}}\,\beta_\mu^{\text{™}}} \frac{dZ_\nu^{\text{™}}}{dz} \frac{dZ_\mu^{\text{™}*}}{dz} [(\frac{n}{x}) R_n^{(q)}(x) (\frac{n}{y}) R_n^{(p)*}(y) + \frac{\varepsilon}{\varepsilon+\Delta\varepsilon} \frac{dR_n^{(q)}(x)}{dx} \frac{dR_n^{(p)*}(y)}{dy}] \}$$

$$\approx \frac{\pi r}{4} \frac{\beta_\nu^{\text{™}}\,\beta_\mu^{\text{™}}}{\sqrt{\int_{-\infty}^{\infty} dz\ \varepsilon |Z_\nu^{\text{™}}|^2 \int_{-\infty}^{\infty} dz\ \varepsilon |Z_\mu^{\text{™}}|^2}} \cdot \int_{-\infty}^{\infty} dz\, \Delta\varepsilon(r,z) \{ R_n^{(q)}(x)\, R_n^{(p)*}(y)\, Z_\nu^{\text{™}} Z_\mu^{\text{™}*}$$

$$+ \frac{1}{\beta_\nu^{\text{™}}\beta_\mu^{\text{™}}} \frac{dZ_\nu^{\text{™}}}{dz} \frac{dZ_\mu^{\text{™}*}}{dz} [(\frac{n}{x}) R_n^{(q)}(x) (\frac{n}{y}) R_n^{(p)*}(y) + \frac{dR_n^{(q)}(x)}{dx} \frac{dR_n^{(p)*}(y)}{dy}] \}$$

$$\approx \frac{\pi r}{4} \frac{\beta_\nu^{\text{™}}\,\beta_\mu^{\text{™}}}{\sqrt{\int_{-\infty}^{\infty} dz\ \varepsilon \left|Z_\nu^{\text{™}}\right|^2 \int_{-\infty}^{\infty} dz\ \varepsilon \left|Z_\mu^{\text{™}}\right|^2}}$$

$$\cdot \int_{-\infty}^{\infty} dz\, \Delta\varepsilon(r,z) \{ R_n^{(q)}(x)\, R_n^{(p)*}(y)\, Z_\nu^{\text{™}} Z_\mu^{\text{™}*}$$

$$+ \frac{1}{2(\beta_\nu^{\text{™}}\,\beta_\mu^{\text{™}})} \frac{dZ_\nu^{\text{™}}}{dz} \frac{dZ_\mu^{\text{™}*}}{dz} [R_{n-1}^{(q)}(x)\, R_{n-1}^{(p)*}(y) + R_{n+1}^{(q)}(x)\, R_{n+1}^{(p)*}(y)] \} \qquad \text{(A4.12)}$$

In the last step, we have used Eq.(A4.8).

Defining

$$\tilde{F}^{(p,q)\text{™}\text{™}}_{\mu n,\nu n}(r) = \frac{\pi}{2}\sqrt{xy}\, R^{(q)}_n(x)\, R^{(p)*}_n(y) \qquad \text{(A4.13a)}$$

$$F^{(p,q)\text{™}\text{™}}_{\mu n,\nu n}(r) = \frac{\pi}{4}\sqrt{xy}\,[\, R^{(q)}_{n-1}(x)\, R^{(p)*}_{n-1}(y) + R^{(q)}_{n+1}(x)\, R^{(p)*}_{n+1}(y)] \qquad \text{(A4.13b)}$$

$$\tilde{K}^{\text{™}\text{™}}_{\mu\nu}(r) = \frac{\sqrt{\beta^{\text{™}}_\nu\, \beta^{\text{™}}_\mu}}{2} \frac{\int_{-\infty}^{\infty} \Delta\varepsilon(r,z)\, Z^{\text{™}}_\nu Z^{\text{™}*}_\mu dz}{\sqrt{\int_{-\infty}^{\infty} \varepsilon \left|Z^{\text{™}}_\nu\right|^2 dz \int_{-\infty}^{\infty} \varepsilon \left|Z^{\text{™}}_\mu\right|^2 dz}} \qquad \text{(A4.13c)}$$

$$K^{\text{™}\text{™}}_{\mu\nu}(r) = \frac{1}{2\sqrt{\beta^{\text{™}}_\nu\, \beta^{\text{™}}_\mu}} \frac{\int_{-\infty}^{\infty} \Delta\varepsilon(r,z) \left(\frac{dZ^{\text{™}}_\nu}{dz}\right)\left(\frac{dZ^{\text{™}*}_\mu}{dz}\right) dz}{\sqrt{\int_{-\infty}^{\infty} \varepsilon \left|Z^{\text{™}}_\nu\right|^2 dz \int_{-\infty}^{\infty} \varepsilon \left|Z^{\text{™}}_\mu\right|^2 dz}} \qquad \text{(A4.13d)}$$

$$(\; x = \beta^{\text{™}}_\nu r \quad \text{and} \quad y = \beta^{\text{™}}_\mu r \;)$$

Eq.(A4.12) can be simplified as

$$K^{(p,q)\text{™}\text{™}}_{\mu n,\nu n}(r) = \tilde{F}^{(p,q)}_{\mu n,\nu n}(r)\, \tilde{K}_{\mu\nu}(r) + F^{(p,q)}_{\mu n,\nu n}(r)\, K_{\mu\nu}(r) \qquad \text{(A4.14)}$$

C. Coupling Coefficients For TE-TM Coupling

The coupling coefficients for this case are (see Eq.(1.41) in Chapter 1)

$$K_{\mu n,\nu n}^{(p,q)TE TM} = 2\pi n\, A_{\nu n}^{(q)TM} A_{\mu n}^{(p)TE*} \frac{(\omega^2 \varepsilon_0 \mu_0)}{(\beta_\nu^{TM} \beta_\mu^{TE})^2} \int_{-\infty}^{\infty} dz\, \Delta\varepsilon(r,z) \frac{dZ_\nu^{TM}}{dz} Z_\mu^{TE*}$$

$$\cdot \left[R_n^{(q)}(\beta_\nu^{TM} r) \frac{dR_n^{(p)*}(\beta_\mu^{TE} r)}{dr} + \frac{\varepsilon}{\varepsilon+\Delta\varepsilon} \frac{dR_n^{(q)}(\beta_\nu^{TM} r)}{dr} R_n^{(p)*}(\beta_\mu^{TE} r) \right] \qquad \text{(A4.15)}$$

and

$$K_{\mu n,\nu n}^{(p,q)TM TE} = 2\pi n\, A_{\nu n}^{(q)TE} A_{\mu n}^{(p)TM*} \frac{(\omega^2 \varepsilon_0 \mu_0)}{(\beta_\nu^{TE} \beta_\mu^{TM})^2} \int_{-\infty}^{\infty} dz\, \Delta\varepsilon(r,z) \frac{dZ_\mu^{TM*}}{dz} Z_\nu^{TE}$$

$$\cdot \left[R_n^{(p)*}(\beta_\mu^{TM} r) \frac{dR_m^{(q)}(\beta_\nu^{TE} r)}{dr} + \frac{\varepsilon}{\varepsilon+\Delta\varepsilon} \frac{dR_n^{(p)*}(\beta_\mu^{TM} r)}{dr} R_m^{(q)}(\beta_\nu^{TE} r) \right] \qquad \text{(A4.16)}$$

Let $x=\beta_\nu^{TM} r$, $y=\beta_\mu^{TE} r$ and substitute the normalization constants from Eq.(A4.3) and Eq.(A4.11) into Eq.(A4.15), we obtain

$$K_{\mu n,\nu n}^{(p,q)TE TM} = \frac{\pi r}{4} \frac{k_0 \int_{-\infty}^{\infty} \Delta\varepsilon \left(\frac{dZ_\nu^{TM}}{dz}\right) Z_\mu^{TE*} dz}{\sqrt{\int_{-\infty}^{\infty} \varepsilon \left|Z_\nu^{TM}\right|^2 dz \int_{-\infty}^{\infty} \left|Z_\mu^{TE}\right|^2 dz}}$$

$$\cdot \left[\left(\frac{n}{x}\right) R_n^{(q)}(x) \frac{dR_n^{(p)*}(y)}{dy} + \frac{dR_n^{(q)}(x)}{dx} \left(\frac{n}{y}\right) R_n^{(p)*}(y) \right] \qquad \text{(A4.17)}$$

for $\Delta\varepsilon/(\varepsilon+\Delta\varepsilon) \ll 1$.

Using the following notation,

$$F_{\mu n,\nu n}^{(p,q)TETM}(r) = \frac{\pi}{2}\sqrt{xy}\,\left[\left(\frac{n}{x}\right) R_n^{(q)}(x)\,\frac{dR_n^{(p)*}(y)}{dy} + \frac{dR_n^{(q)}(x)}{dx}\left(\frac{n}{y}\right) R_n^{(p)*}(y)\right]$$

$$\left(x=\beta_\nu^{TM} r \text{ and } y=\beta_\mu^{TE} r \right) \qquad \text{(A4.18a)}$$

$$K_{\mu,\nu}^{TETM}(r) = \frac{1}{2}\,\frac{k_0}{\sqrt{\beta_\nu^{TM}\beta_\mu^{TE}}}\,\frac{\int_{-\infty}^{\infty}\Delta\varepsilon\left(\frac{dZ_\nu^{TM}}{dz}\right) Z_\mu^{TE*}\,dz}{\sqrt{\int_{-\infty}^{\infty}\varepsilon\left|Z_\nu^{TM}\right|^2 dz\int_{-\infty}^{\infty}\left|Z_\mu^{TE}\right|^2 dz}} \qquad \text{(A4.18b)}$$

we get

$$K_{\mu n,\nu n}^{(p,q)TETM} = F_{\mu n,\nu n}^{(p,q)TETM}(r)\,K_{\mu,\nu}^{TETM}(r) \qquad \text{(A4.19)}$$

Eq.(A4.7) allows us to obtain

$$F_{\mu n,\nu n}^{(p,q)TETM}(r) = \left(\frac{\pi}{2}\right)\sqrt{xy}\,\left[\left(\frac{n}{x}\right) R_n^{(q)}(x)\,\frac{dR_n^{(p)*}(y)}{dy} + \frac{dR_n^{(q)}(x)}{dx}\left(\frac{n}{y}\right) R_n^{(p)*}(y)\right]$$

$$= \frac{\pi}{4}\sqrt{xy}\,\left[\,R_{n-1}^{(q)}(x)\,R_{n-1}^{(p)*}(y) - R_{n+1}^{(q)}(x)\,R_{n+1}^{(p)*}(y)\,\right] \qquad \text{(A4.20)}$$

Similarly, Eq.(A4.16) can be expressed as

$$K_{\mu n,\nu n}^{(p,q)TMTE} = F_{\mu n,\nu n}^{(p,q)TMTE}(r)\,K_{\mu,\nu}^{TMTE}(r) \qquad \text{(A4.21)}$$

with

$$F_{\mu n,\nu n}^{(p,q)TM\,TE}(r) = \frac{\pi}{4}\sqrt{xy}\,[\,R_{n-1}^{(p)*}(x)\,R_{n-1}^{(q)}(y) - R_{n+1}^{(p)*}(x)\,R_{n+1}^{(q)}(y)\,] \qquad \text{(A4.22a)}$$

$$\left(x=\beta_\mu^{TM} r \;,\; y=\beta_\nu^{TE} r \right)$$

and

$$K_{\mu,\nu}^{TM\,TE}(r) = \frac{1}{2}\frac{k_0}{\sqrt{\beta_\nu^{TE}\,\beta_\mu^{TM}}}\frac{\int_{-\infty}^{\infty}\Delta\varepsilon\,\frac{dZ_\mu^{TM*}}{dz}\,Z_\nu^{TE}\,dz}{\sqrt{\int_{-\infty}^{\infty}\varepsilon\left|Z_\mu^{TM}\right|^2 dz\int_{-\infty}^{\infty}\left|Z_\nu^{TE}\right|^2 dz}} \qquad \text{(A4.22b)}$$

Eq.(A4.6), Eq.(A4.14), Eq.(A4.19) and Eq.(A4.21) can be expressed in a unified form as :

$$K_{\mu n,\nu n}^{(p,q)\sigma\tau} = F_{\mu n,\nu n}^{(p,q)\sigma\tau}(r)\,K_{\mu,\nu}^{\sigma\tau}(r) \quad (\,\sigma=\tau=\text{TE or } \sigma\neq\tau, \text{ with } \sigma \text{ and } \tau=\text{TE, TM}) \qquad \text{(A4.23a)}$$

$$= \tilde{F}_{\mu n,\nu n}^{(p,q)\sigma\tau}(r)\,\tilde{K}_{\mu,\nu}^{\sigma\tau}(r) + F_{\mu n,\nu n}^{(p,q)\sigma\tau}(r)\,K_{\mu,\nu}^{\sigma\tau}(r) \quad (\,\sigma=\tau=TM\,) \qquad \text{(A4.23b)}$$

Appendix V

Derivation of Large Radius Conditions

Here, we derive the condition for the large radius approximation to be valid. Using the notations of [82], we have

$$H_n^{(1)}(\beta r) = -j\, C_n(\beta r)\, e^{\,j\delta_n(\beta r)} \tag{A5.1a}$$

$$H_n^{(2)}(\beta r) = j\, C_n(\beta r)\, e^{\,-j\delta_n(\beta r)} \tag{A5.1b}$$

where $C_n(\beta r)$ is the amplitude and $\delta_n(\beta r)$ is the phase angle of the Hankel functions. Substitute Eqs.(A5.1) into Eqs.(2.27), we obtain

$$F_{n,n}^{(+,+)\sigma\sigma}(r) = F_{n,n}^{(-,-)\sigma\sigma^*}(r) = \frac{\pi\beta^{\sigma} r}{4}\{\,[\,C_{n-1}(\beta^{\sigma} r)\,]^2 + [C_{n+1}(\beta^{\sigma} r)\,]^2\,\}$$

(σ=TE or TM) (A5.2a)

$$F_{n,n}^{(+,-)\sigma\sigma}(r) = F_{n,n}^{(-,+)\sigma\sigma^*}(r) = -\frac{\pi\beta^{\sigma} r}{4}\{\,[\,C_{n-1}(\beta^{\sigma} r)\,]^2\, e^{j2\delta_{n-1}(\beta^{\sigma} r)} + [C_{n+1}(\beta^{\sigma} r)\,]^2\, e^{j2\delta_{n+1}(\beta^{\sigma} r)}\}$$

(σ=TE or TM) (A5.2b)

$$\widetilde{F}_{n,n}^{(+,+)\sigma\sigma}(r) = \widetilde{F}_{n,n}^{(-,-)\sigma\sigma^*}(r) = \frac{\pi\beta^{\sigma} r}{2}[\,C_n(\beta^{\sigma} r)\,]^2$$

(σ=TM) (A5.2c)

$$\widetilde{F}_{n,n}^{(+,-)\sigma\sigma}(r) = \widetilde{F}_{n,n}^{(-,+)\sigma\sigma^*}(r) = -\frac{\pi\beta^{\sigma} r}{2}[\,C_n(\beta^{\sigma} r)\,]^2\, e^{j2\delta_n(\beta^{\sigma} r)}$$

(σ=TM) (A5.2d)

$$F_{n,n}^{(+,+)\sigma\tau}(r) = F_{n,n}^{(-,-)\sigma\tau^*}(r) = \frac{\pi r}{4}\sqrt{\beta^{\sigma}\beta^{\tau}}\ \{\ C_{n-1}(\beta^{\sigma} r)\, C_{n-1}(\beta^{\tau} r)\, e^{j2[\,\delta_{n-1}(\beta^{\sigma} r)-\delta_{n-1}(\beta^{\tau} r)\,]}$$

$$- C_{n+1}(\beta^{\sigma} r)\, C_{n+1}(\beta^{\tau} r)\, e^{j2[\,\delta_{n+1}(\beta^{\sigma} r)-\delta_{n+1}(\beta^{\tau} r)\,]}\ \}$$

$$(\sigma \neq \tau) \qquad \text{(A5.2e)}$$

$$F_{n,n}^{(+,-)\sigma\tau}(r) = F_{n,n}^{(-,+)\sigma\tau^*}(r) = -\frac{\pi r}{4}\sqrt{\beta^{\sigma}\beta^{\tau}}\ \{\ C_{n-1}(\beta^{\sigma} r)\, C_{n-1}(\beta^{\tau} r)\, e^{j2[\,\delta_{n-1}(\beta^{\sigma} r)+\delta_{n-1}(\beta^{\tau} r)\,]}$$

$$- C_{n+1}(\beta^{\sigma} r)\, C_{n+1}(\beta^{\tau} r)\, e^{j2[\,\delta_{n+1}(\beta^{\sigma} r)+\delta_{n+1}(\beta^{\tau} r)\,]}\ \}$$

$$(\sigma \neq \tau) \qquad \text{(A5.2f)}$$

For $\beta r > n \geq 1$ and $q_n = \sqrt{(\beta r/n)^2 - 1} >> 0.6/\sqrt{n}$, we have [90]

$$C_n \approx \sqrt{\frac{2}{\pi\, n\, q_n}} \qquad \text{(A5.3a)}$$

$$\delta_n \approx n\,[\,q_n - \tan^{-1}(q_n)\,] + \frac{\pi}{4} \qquad \text{(A5.3b)}$$

Putting Eqs. (A5.3) into Eqs. (A5.2) and after some calculations, we can obtain

$$\left|F_{n,n}^{(+,+)\sigma\sigma}\right| = \left|F_{n,n}^{(-,-)\sigma\sigma^*}\right| \approx 1 + \frac{1}{2}\frac{(n^2+1)}{(\beta r)^2} \qquad (\sigma = \text{TE or TM}) \qquad \text{(A5.4a)}$$

$$\left|F_{n,n}^{(+,-)\sigma\sigma}\right| = \left|F_{n,n}^{(-,+)\sigma\sigma^*}\right| \approx 1 - \frac{1}{2}\frac{(3n^2-1)}{(\beta r)^2} \qquad (\sigma = \text{TE or TM}) \qquad \text{(A5.4b)}$$

$$\left|\widetilde{F}_{n,n}^{(+,+)\sigma\sigma}\right| = \left|\widetilde{F}_{n,n}^{(-,-)\sigma\sigma^*}\right| \approx 1 + \frac{1}{2}\left(\frac{n}{\beta r}\right)^2 \qquad (\sigma = \text{TM}) \qquad \text{(A5.4c)}$$

$$\left|\tilde{F}_{n,n}^{(+,-)\sigma\sigma}\right| = \left|\tilde{F}_{n,n}^{(-,+)\sigma\sigma^*}\right| \approx 1 + \frac{1}{2}\left(\frac{n}{\beta r}\right)^2 \qquad (\sigma=\text{TM}) \qquad \text{(A5.4d)}$$

$$\left|F_{n,n}^{(+,+)\sigma\tau}\right| = \left|F_{n,n}^{(-,-)\sigma\tau}\right| \approx \frac{n}{(\beta r)^2} \qquad (\sigma=\text{TE}, \tau=\text{TM and vice versa}) \qquad \text{(A5.4e)}$$

$$\left|F_{n,n}^{(+,-)\sigma\tau}\right| = \left|F_{n,n}^{(-,+)\sigma\tau}\right| \approx \frac{2n}{\beta r} \qquad (\sigma=\text{TE}, \tau=\text{TM and vice versa}) \qquad \text{(A5.4f)}$$

In deriving Eqs.(A5.4e)-(A5.4f), we have assumed that the birefringence between TE and TM modes are small with $\beta^{TE} \approx \beta^{TM} = \beta,$. For simplicity, we have omitted the superscripts " σ " and " τ " for the propagation constants. No confusion should ensue. Note that Eq.(A5.4f) approaches zero as ($1/\beta r$) for large βr, which is much slower than Eq.(A5.4e).

As a reasonable approximation, we set that the residual terms on the right-hand side of Eqs.(A5.4a)-(A5.4f) be less than 10%. Take Eq.(A5.4a) as an example, we require that

$$\frac{1}{2}\frac{(n^2+1)}{(\beta r)^2} \le 0.1 \quad , \quad \text{or} \quad \beta r \ge \sqrt{5(n^2+1)} \qquad \text{(A5.5a)}$$

Correspondingly, we obtain

$$\beta r \ge \sqrt{5(3n^2-1)} \qquad \text{for Eq.(A5.4b)} \qquad \text{(A5.5b)}$$

$$\beta r \ge \sqrt{5n^2} \qquad \text{for Eqs.(A5.4d)-(A5.4d)} \qquad \text{(A5.5c)}$$

$$\beta r \ge 4\,n \qquad \text{for Eq.(A5.4e)} \qquad \text{(A5.5d)}$$

$$\beta r \ge 20\,n \qquad \text{for Eq.(A5.4f)} \qquad \text{(A5.5e)}$$

For the coupling between cylindrical waves of the same polarization (TE-TE coupling or TM-TM coupling), Eqs.(A5.5a)-(A5.5b) can be combined together to give the following criterion for the large radius approximation:

$$r \geq r_0 = \frac{\sqrt{5(3n^2+1)}}{\beta} \qquad \text{(A5.6)}$$

which is valid for $n \geq 0$. When r is larger than r_0, the large radius approximation is very good as shown in Tables 2.1-2.2.

For the coupling between cylindrical waves of different polarizations (TE-TM coupling), the following condition should be used in judging the validity of the large radius approximation :

$$r \geq r_0 = \frac{20\,n}{\beta} \qquad \text{(A5.7)}$$

This condition is detailed in Table 2.3. For comparison, we also used Eq.(A5.6) to estimate the amplitudes of the cylindrical-wave factors for TE-TM couplings at βr_0. The results are listed in Table 2.4.

Appendix VI

Biography

Chunmeng Wu est né le 26 octobre 1962 dans la province de Guangxi, en Chine. Il a reçu le baccalauréat en physique à l'Institut de Génie des Télécommunications de Chengdu, province de Sichuan, Chine, en 1982. Il est venu au Canada en 1984. De mai 1984 à juin 1987, il a étudié au département de génie électrique de l'Université McGill, où il a obtenu le diplôme de maîtrise en 1987. De juillet 1987 jusqu'à présent, il a poursuivi des études de doctorat au département de génie physique de l'Ecole Polytechnique de Montréal, sous la supervision des professeurs Romain Maciejko et S. Iraj Najafi. Durant les deux dernières années, il a effectué ses recherches au "Advanced Technology Laboratory" de Bell-Northern Research (BNR) à Ottawa. Ses intérêts de recherche incluent les lasers à semiconducteur, les modulateurs à ondes guidées, les dispositifs à guide d'onde sur substrat de verre et la communication par fibre optique. M. Wu est membre étudiant de "Optical Society of America".

Chunmeng Wu, was born on October 26, 1962, in Guangxi Province, China. He received the Bachelor's degree in physics from the Chengdu Institute of Radio Engineering, Sichuan Province, China, in 1982. He came to Canada in 1984. From May 1984 to June 1987, he studied in the Department of Electrical Engineering of McGill University, where he obtained the Master's degree in 1987. From July 1987 to present, he has been a Ph.D student in the Department of Engineering Physics, Ecole Polytechnique of Montreal, under the supervision of Professors Romain Maciejko and S. Iraj Najafi. For the past two years, he has been working at the Advanced Technology Laboratory of Bell-Northern Research (BNR), Ottawa. His research interests include semiconductor lasers, guided-wave modulators, glass-waveguide devices and fiber-optics. Mr. Wu is a student member of the Optical Society of America.

Appendix VII

List of Publications and Conferences

Publications on Circular Grating Lasers :

1. WU, C., MAKINO, T., GLINSKI, J., MACIEJKO, R. and NAJAFI, S.I., " Self-consistent coupled-wave theory for circular gratings on planar dielectric waveguides ", *Journal of Lightwave Technology*, vol.9, no.10, 1991, pp.1264-1277.

2. WU, C., SVILANS, M., FALLAHI, M., MAKINO, T., GLINSKI, J., MARITAN, C. and BLAAUW, C., " Optically pumped surface-emitting 1.3 μm DFB laser with circular grating ", Electronics Letters, vol.27, no.20, 1991, pp. 1891-1820.

3. WU, C., SVILANS, M., FALLAHI, M., TEMPLETON, I., MAKINO, T., MACIEJKO, R., NAJAFI, S.I., BLAAUW, C., MARITAN, C. and KNIGHT, D.G., " Room temperature operation of electrically pumped surface-emitting circular grating DBR laser, " *Electron. Lett.*, vol.28, no. 11, May, 1992, pp. 1037-1039.

4. WU, C., MAKINO, T., MACIEJKO, R., NAJAFI, S.I. and SVILANS, M., " Simplified coupled-wave equations for cylindrical waves in circular grating planar waveguides, " accepted for publication in *J. Lightwave Technol.*

5. MAKINO, T. and WU, C., " Circular grating DFB and DBR semiconductor lasers: threshold current analysis, " accepted for publication in *Optics Communications.*

6. WU, C., SVILANS, M., FALLAHI, M., TEMPLETON, I., MAKINO, T., MACIEJKO, R., NAJAFI, S.I., BLAAUW, C., MARITAN, C. and KNIGHT, D.G., " Electrically-pumped circular grating DBR laser, " accepted for publication in *Photon. Technol. Lett.*

7. WU, C., MAKINO, T., NAJAFI, S.I., MACIEJKO, R., SVILANS, M., GLINSKI, J. and FALLAHI, M., "Threshold gain and threshold current analysis of circular grating DFB and DBR lasers, " submitted to *IEEE J. Quantum Electron.*

Conferences on Circular Grating Lasers :

1. WU, C., MAKINO, T., GLINSKI, J., MACIEJKO, R. and NAJAFI, S.I., " Circular grating resonators: a coupled-wave analysis, " presented at the *1st IEEE International Workshop on Photonic Networks, Components and Applications*, Monte-bello, Quebec, Canada, Oct.11-13, 1990.

2. FALLAHI, M., WU, C., MARITAN, C., FOX, K. and BLAAUW, C., " Fabrication of circular gratings on InP by E-beam and reactive-ion etch " *LEOS 1991 Summer Topical Meetings: Microfabrication for Photonics and Optoelectronics*, Newport Beach, California, 31st July-2nd August, 1991.

3. WU, C., SVILANS, M., FALLAHI, M., MAKINO, T., GLINSKI, J., MARITAN, C. and BLAAUW, C., " Optically pumped circular grating DFB 1.3 μm lasers for surface emission," post dealine paper, *ECOC'91*, Paris, France, 9-12 September 1991.

4. WU, C., SVILANS, M., MAKINO, T., FALLAHI, M., TEMPLETON, I., NAJAFI, S.I., MACIEJKO, R., BLAAUW, C., MARITAN, C. and KNIGHT, D.G., "Electrically pumped circular grating DBR lasers ", presented at the *2nd IEEE International Workshop on Photonic Networks, Components and Applications*, Monte-bello, Quebec, Canada, March 9-11, 1992.

5. WU, C., SVILANS, M., MAKINO, T., FALLAHI, M., TEMPELTON, I., MACIEJKO, R., NAJAFI, S.I., BLAAUW, C., MARITAN, C. and KNIGHT, D.G., " Circular grating surface-emitting laser, " post deadline paper (PD3), *Integrated Photonics Research Topica Meeting*, New Orleans, LA., April 13-14, 1992.

6. KNIGHT, D.G., WU, C., SVILANS, M., FOX, K., ZORZI, J., BLAAUW, C. and MARITAN, C., " MOCVD regrowth of semi-insulating GaInAsP for circular grating DBR lasers, " presented at *the 6th International Conference on MOVPE* , Cambridge, MA, USA, June 8-11, 1992.

7. WU, C., SVILANS, M., MAKINO, T., BLAAUW, C., MARITAN, C., KNIGHT, D.G., FALLAHI, M., TEMPELTON, I., MACIEJKO, R., and NAJAFI, S.I., "Room Temperature Operation of Circular Grating DBR Surface-Emitting Laser, " accepted for presentation at *the 13th IEEE International Semiconductor Laser Conference*, Takamatsu, Japan, Sep.21-25, 1992.

Other Publications:

1. WU, C., TOUAM, T., NAJAFI, S.I., " Analysis of Zn-diffused semiconductor slab waveguide : exact solution and WKB approximation, " *Intl. J. Optoelectron.*, vol.6, no.4, 1991, pp. 365-384.

2. WU, C., NAJAFI, S.I. and MACIEJKO, R., " Substrate leaky TE-modes in four-layer dielectric waveguides, " *Intl.J.Optoelectronics*, vol.5, no.3, 1990, pp.217-226.

3. WU, C., NAJAFI, S.I., MACIEJKO, R. and CURRIE, J.F., " Propagation losses in GaAs/AlGaAs four-layer waveguides, " *Intl. J. Optoelectronics*, vol.4, no.1, 1989, pp.81-86.

4. TOUAM, T., WU, C., GIGASE, Y., BELANGER, M., CURRIE, J.F. and NAJAFI, S.I., " Fabrication, characterization and analysis of Zn-diffused GaAs waveguides, " *IEEE J. Quantum Electron.*, vol.25, no.5, May, 1989, pp.850-853.

5. NAJAFI, S.I. and WU, C., " Potassium ion-exchanged glass waveguide directional couplers at 0.6328 and 1.3µm, " *Appl. Opt.*, vol. 28, 1989, pp.2459-2460.

6. NAJAFI, S.I., TOUAM, T., WU, C. and CURRIE, J.F., " Modal study of GaAs waveguides with Zn-diffused boundaries, " *App. Opt.*, vol.28, 1989, pp.987-989.

7. YANG, R., WU, C. and YIP, G. L., " Approximate formulas for the microbending loss in single-mode fibers, " *Opt. Lett.*, vol.12, no.6, June, 1987, pp.428-430.

8. WU, C. and YIP, G.L., " Coupled-mode analysis of a bent birefringent fiber ", *Opt. Lett.*, vol.12, no.7, July, 1987, pp. 522-524.

9. WU, C., Analysis of High Birefringence Optical Fibers under Elastic Deformations, *Master's thesis*, Dept. of Electrical Eng., McGill University, Montreal, Canada, July, 1987.

Other Conferences:

1. NAJAFI, S. I. and WU, C., " Single-mode polarization-insensitive wavelength-independent ion-exchanged glass directional couplers, " *Integrated Optics and Optical Fiber COmmunications (IOOC'89)*, Japan, July 1989.

2. NAJAFI, S.I. and WU, C., " Fabrication and characterization of single-mode glass waveguide power dividers, " *Optical Fiber Communications (OFC'89)*, Houston, Texas , U.S.A, Feb.1989.

Globe & Mail

Bell-Northern tests new chip 20/6/92

Device holds promise for phone fibre optics in the home

BY LAWRENCE SURTEES
Telecommunications Reporter

Scientists at **Bell-Northern Research Laboratories Ltd.** say they have successfully tested a new light-emitting laser microchip that will make it affordable to bring fibre optics to telephone subscribers' homes.

Fibre optics to the home would allow phone companies to compete with cable-television companies and deliver a greater number of video signals on demand via a phone line.

The new laser chip has the potential to slash the costs of current fibre-optic electronic systems, Peter Scovell, vice-president of advanced systems and technology at BNR, said in an interview.

The Ottawa-based research and development arm of **Northern Telecom Ltd.** released details of the new chip yesterday during a visit to the labs by Russian President Boris Yeltsin.

Northern Telecom, which is based in Mississauga, is a unit of BCE Inc., a Montreal-based conglomerate.

The new laser chip, called a circular grating surface emitting laser, is smaller than a grain of salt.

Unlike conventional laser-emitting chips, which emit a beam of light from the side, the circular grating etched on to the surface of the microchip emits a more powerful beam from the top of the chip.

"We believe the new technique will make it easier, and cheaper, to make the electronic couplers required to connect fibre-optic cables to the electronic devices that power them," Mr. Scovell said.

Fibre optics are hair-thin strands of glass that use laser-generated pulses of light to transmit information.

However, more than 70 per cent of the current cost of fibre-optic telephone systems is for the packaging systems that precisely join a fibre-optic cable to the modules containing laser-emitting chips.

Those modules are needed to convert electrical signals into light pulses so that information can be transmitted along the fibre.

"Conventional laser-emitting chips generate a divergent beam of light."

"It is not only essential, but very difficult, to precisely align the two surfaces," Mr. Scovell said.

The new BNR technique using the gratings, however, makes it much easier to align the fibre and the laser chip.

The circular grating, which is a fraction of a millimetre in diameter, resembles the tracks of a compact disc with hundreds of concentric grooves.

It reflects a two-dimensional beam of light upwards into a three-dimensional beam, with a surface area more than 10,000 times greater than conventional lasers, Mr. Scovell said.

"We have quite a lot of work to do to move to production-scale volumes, but we believe the new chip will greatly reduce the cost of fibre-optic systems for phone companies," he said.

Although fibre-optic systems are now used by phone companies and large businesses for high-volume and high-speed networks, the high cost has prevented phone companies from bringing fibre optics the last few dozen metres to each subscriber's phone.

Using conventional electronics, it costs a phone company about $1,500 for the fibre-optic cable and electronic modules for each phone, compared with about $150 for comparable systems based on copper wire.

Mr. Scovell said it is too early to say how much the new chip may trim from those costs.

"Obviously, we have to achieve more than a 10-fold reduction in those costs, and we think this new chip will take us a good part of the way toward that goal."